UiO : University of Oslo

Vetle Wegner Ingeberg

The Oslo Method in Inverse Kinematics

Thesis submitted for the degree of Philosophiae Doctor

Department of Physics
Faculty of Mathematics and Science

2022

Series of dissertations submitted to the
Faculty of Mathematics and Science, University of Oslo
No. 2508

ISSN 1501-7710

Cover: Hanne Baadsgaard Utigard.
Print production: Reprosentralen, University of Oslo.

To my dog, Georg

Acknowledgements

First, and most importantly, I would like to thank my supervisors, Sinniva Siem and Mathis Wiedeking. I would not have been able to finish this thesis without your invaluable guidance. I'm the type of person who cannot stand black boxes and stubbornly wants to solve everything myself. Under your supervision, I've enjoyed the freedom to explore those boxes, a freedom not everyone gets to experience. Still, I've always been greeted with open doors whenever I was stuck or had anything I needed to discuss.

I would like to thank all my colleagues and friends that I've made along the way. Especially the NEP group where the default is to collaborate and support each other. Twice I've been able to stay at iThemba LABS for an extended period, where I met and befriended many amazing people. I'm very grateful for the opportunity and the experiences I made during the many trips I've had to South Africa.

Til slutt så vil jeg takke min familie og venner. Jeg kan alltid stole på dere når jeg trenger det som mest. Dere er der for meg på de verste, og de beste dagene. Uten den tryggheten hadde jeg aldri klart dette.

Vetle Wegner Ingeberg
Oslo, February 2022

List of Papers

This thesis is based on the following four papers:

Paper I

Ingeberg, V. W., Siem, S., Wiedeking, M., Sieja, K., Bleuel, D. L., Brits, C. P., Bucher, T. D., Dinoko, T. S., Easton, J. L., Görgen, A., Guttormsen, M., Jones, P., Kheswa, B. V., Khumalo, N. A., Larsen, A. C., Lawrie, E. A., Lawrie, J. J., Majola, S. N. T., Malatji, K. L., Makhathini, L., Maqabuka, B., Negi, D., Noncolela, S. P., Papka, P., Sahin, E., Schwengner, R., Tveten, G. M., Zeiser, F., and Zikhali, B. R. "First application of the Oslo method in inverse kinematics". In: *Eur. Phys. J. A.* **56**:68 (2020), DOI: 10.1140/epja/s10050-020-00070-7.

Paper II

Ingeberg, V. W., Jones, P., Msebi, L., Siem, S., Wiedeking, M., Avaa, A. A., Bucher, T.D., Brits, C. P., Chisapi, M. V., Lawrie, E. A., Malatji, K. L., Maqabuka, B., Makhathini, L., Noncolela, S. P., Ndayishmye, J., Netshiya, A., Shinda, O., and Zikhali, B. R. "Nuclear Level Density and γ-ray Strength Function of ^{63}Ni" *Manuscript in preparation.*

Paper III

Ingeberg, V. W., Siem, S., Wiedeking, M., Abrahams, K. J., Arnswald, K., Bello Garrote, F., Berry, T., Bleuel, D. L., Cederkäll, J., Christoffersen, T. L., Cox, D. M., Crespo Campo, L., De Witte, H., Gaffney, L. P., Görgen, A., Henrich, C., Illana Sison, A., Jones, P., Kheswa, B.V., Kröll, T., Majola, S .N. T., Malatji, K. L., Nogwanya, T., Ojala. J., Pakarinen, J., Rainovski, G., Reiter, P., Rosiak, D., von Schmid, M., Seidlitz, M., Siebeck, B., Snäll, J., Sowazi, K., Tveten, G.M., Warr, N. and Zeiser, F. "The Oslo Method With Radioactive Beam - Nuclear Level Density and γ-ray Strength Function of ^{67}Ni" *Manuscript in preparation.*

Paper IV

Msebi, L., Ingeberg, V. W., Jones, P. Sharpey-Schafer, J. F., Avaa, A. A., Bucher, T. D., Brits, C. P., Chisapi, M. V., Kenfack, E. A., Lawrie, E. A., Malatji, K. L., Noncolela, S. P., Ndayishimye, J., Netshiya, A., Shrinda, O., Wiedeking, M., and Zikhali, B. R. "A fast timing array 2" x 2" LaBr3:Ce for lifetime measurements

of excited nuclear states" In: *Nuclear Inst. and Methods in Physics Research, A.* **1026**:166195 (2022), DOI: 10.1016/j.nima.2021.166195.

All papers are reprinted at the end of the thesis. Paper I is published under a Creative Commons Attribution 4.0 International License. For Paper IV, permission has been obtained from Elsevier B.V.

Contents

List of Figures

Chapter 1

Introduction

The nucleus is a quantum mechanical system and can only be in certain discrete energy levels and the ground state is the level with the lowest energy. At what energies the excited levels occur relative to the ground state varies from nucleus to nucleus and the occurrence of these levels increases exponentially as the energy increases. The average number of levels at a particular excitation energy, per unit energy, is the nuclear level density. Excited levels quickly decay to other levels with lower energy by emitting γ-rays until the nucleus reaches the ground state. On average, the distribution of emitted γ-ray energies and the lifetime of the level is governed by the γ-ray strength function and the level density at the final excitation energy. The main focus of this work is the nuclear level density and the γ-ray strength function, which are statistical properties of the nucleus and contain vital information about the nuclear structure and decay.

The outcome of nuclear reactions are strongly linked to the statistical properties of the final residual nucleus and are predicted within the statistical framework of Hauser-Feshbach theory [1]. Accurate knowledge about the neutron-capture rates are of utmost importance within the field of nuclear astrophysics as they significantly impact the model predictions of the slow (s-process), intermediate (i-process) and rapid (r-process) neutron-capture processes responsible for the nucleosynthesis of elements heavier than iron [2–6]. Typical theoretical estimates of capture rates on unstable neutron-rich nuclei can vary as much as three or four orders of magnitude. Therefore, these rates represent a large source of uncertainty for model predictions on the abundance distribution of elements.

Experimental measurements of the γ-ray strength function and nuclear level density are complicated. Most methods are only able to measure either the level density or the γ-ray strength function. The analytical framework called the Oslo method is the only method able to simultaneously measure both [7]. With the Oslo method, a large enhancement at low γ-ray energy in the γ-ray strength function of ^{56,57}Fe was reported in 2004 [8]. This was the first observation of such an enhancement and has since been found in nuclei ranging from as light as ^{43}Sc [9] and as heavy as ^{152}Sm [10]. Assuming the presence of the enhancement in neutron-rich nuclei, it has been shown that the enhancement could cause an increase in capture rate of as much as two orders of magnitude [11].

The Oslo method is applied to experimental data where γ-ray spectra and the initial excitation are measured. Typically, experiments use beams of light ions (protons, deuterons, ^{3}He ions or α particles) impinging on a isotopically enriched target material. Induced nuclear reactions produce a particular residual nucleus. Scattered fragment particles are measured in coincidence with the γ-rays de-exciting the residual nucleus. The reaction channels are chosen by

selecting the desired scattered particle type (i.e. proton, deuteron, triton, α, ...), while the initial excitation energy of the residual nucleus is found from kinematic reconstruction. An excitation versus γ-ray energy matrix is constructed from the coincidences, and the γ-ray strength function and nuclear level density are uncovered by applying the Oslo method. For most nuclei close to the valley of stability, the γ-ray strength functions and nuclear level densities are easily probed with light ion beams. However, to reach neutron-rich nuclei further away than one or two neutrons from stability, other types of experiments have to be employed. One alternative approach is using inverse kinematics, where a heavy ion beam impinges on a target of light particles, e.g. deuterated plastic targets. Another method is the β-Oslo method where γ-rays following β-decay are measured in total γ-absorption spectroscopy [12]. The main topic of this thesis is the application of the Oslo method on inverse kinematics experiments. The thesis work also included the development and implementation of $LaBr_3$:Ce detectors and digital data acquisition systems for OSCAR.

This thesis is structured in two main parts. The first chapters introduce concepts and provide context to the second part which contains four papers. Central theoretical models of the nuclear level density and γ-ray strength function are presented in Chapter 2, as well as a short description of the Hauser-Feshbach theory of nuclear reactions. Chapter 3 provides an overview of the latest detector developments and the equipment enabling the experiments while Chapter 4 introduces the Oslo method. Challenges and experiences unique to inverse kinematics experiments are discussed in Chapter 5. Lastly, Chapter 6 will summarize the thesis and present some ideas for future experiments.

The papers cover a diverse set of topics. In Paper I the γ-ray strength function and nuclear level density of ^{87}Kr are extracted from an inverse kinematics experiment at iThemba LABS. This was the proof-of-principle experiment showing that the Oslo method could be applied on data from inverse kinematics. Paper III applies the Oslo method on data from an inverse kinematics experiment with a radioactive ^{66}Ni beam at ISOLDE CERN, to probe the level density and γ-ray strength function of ^{67}Ni.

Paper II presents the level density and γ-ray strength function of ^{63}Ni. The data was collected during the commissioning experiment of a new fast-timing array at iThemba LABS. Characterization of this array is presented in Paper IV.

Chapter 2

Theory

Nuclear level density

The nuclear level density (NLD) is the number of levels in the nucleus per energy unit,

$$\rho(E_x, J, \pi) = \frac{N(E_x, J, \pi)}{\Delta E}, \tag{2.1}$$

where $N(E_x, J, \pi)$ is the number of levels with spin J and parity π, within an excitation bin with energy E_x and width ΔE. Summing over spin and parity gives the total level density

$$\rho(E_x) = \sum_{J,\pi} \rho(E_x, J, \pi) = \sum_{J,\pi} \rho(E_x) g(E_x, J) \tau(E_x, \pi), \tag{2.2}$$

where $g(E_x, J)$ is the spin distribution and $\tau(E_x, \pi)$ is the parity distribution. For the vast majority of nuclei, the parity distribution will be roughly the same for both odd and even parity. There are examples where this is not true such as ^{60}Ni, where the first odd-parity level occurs at around 4 MeV [13]. For the nuclei studied in this thesis, the parity distribution is assumed to be equal. The spin distribution is usually modeled with the Ericson distribution [14]

$$\begin{aligned} g(E_x, J) &= \exp\left(-\frac{J^2}{2\sigma^2(E_x)}\right) - \exp\left(-\frac{(J+1)^2}{2\sigma^2(E_x)}\right) \\ &\approx \frac{2J+1}{2\sigma^2(E_x)} \exp\left(-\frac{(J+1/2)^2}{2\sigma^2(E_x)}\right), \end{aligned} \tag{2.3}$$

where $\sigma(E_x)$ is the spin cut-off parameter.

If the nuclear level density and the spin distribution are known, the density of states can be found using

$$\Xi(E_x) = \sum_J (2J+1)\rho(E_x, J). \tag{2.4}$$

Observant readers might have made the connection that the state density essentially is a partition function. The connection to statistical mechanics is the main inspiration for the common phenomenological models of the nuclear level density.

Arguably, the first and most well known model for the nuclear level density is the Back-shifted Fermi gas model (BSFG). It was first derived by Bethe [15] in 1936, approximating the nucleons as non-interacting fermions in a common

potential. The modern formulation of the model was presented in 1965 by Gilbert and Cameron [16]:

$$\rho_{\mathrm{BSFG}}(E_x) = \frac{\sqrt{\pi}}{12\sigma(E_x)} \frac{\exp(2\sqrt{a(E_x-\delta)})}{a^{1/4}(E_x-\delta)^{5/4}}, \tag{2.5}$$

where a is the level density parameter, δ is the energy shift and $\sigma(E_x)$ is the spin cut off parameter. Another well known model is the Constant temperature (CT) model first proposed by Ericson in 1959 [17]:

$$\rho_{\mathrm{CT}}(E_x) = \frac{1}{T} \exp\left(\frac{E_x - E_0}{T}\right), \tag{2.6}$$

where T is the nuclear temperature and E_0 is an empirical shift parameter. The constant temperature model arises from the assumption that added energy to the nucleus will be used to break nucleon pairs, analogous to a phase change. Once enough nucleon pairs have melted, the nucleus will transit into a state that can be described as a Fermi gas.

There are several proposed models for the spin cut off parameter. Most notable are the rigid moment of inertia (RMI) formula proposed by von Egidy and Bucurescu in 2005 [18], the formula of Gilbert and Cameron [16] and the formula by von Egidy and Bucurescu proposed in 2009 [19]. The RMI is parameterized as

$$\sigma^2(E_x) = 0.0146A^{2/3} \frac{1+\sqrt{4a(E_x-\delta)}}{2a}, \tag{2.7}$$

where a and δ are the density and shift parameter, respectively, from the BSFG model and A is the mass number of the nucleus. Gilbert and Cameron's formula for the spin cut-off parameter is

$$\sigma^2(E_x) = 0.0888A^{2/3}a\sqrt{\frac{E_x-\delta}{a}}. \tag{2.8}$$

The formula of von Egidy and Bucurescu proposed in 2009 is

$$\sigma^2(E_x) = 0.391A^{0.675}(E-0.5P'_a)^{0.312}, \tag{2.9}$$

with the P'_a parameter being related to the deuteron pairing energy by $P'_a = (-1)^{Z+1}P_d$ and Z being the atomic number. Another frequently used spin cut off model was proposed by Guttormsen *et al.* in 2017 [20], assuming $\sigma^2(E_x)$ as linearly increasing with excitation energy:

$$\sigma^2(E_x) = \sigma_d^2 + \frac{E_x - E_d}{S_n - E_d}(\sigma^2(S_n) - \sigma_d^2). \tag{2.10}$$

The spin cut off parameterm σ_d, is estimated by fitting the spin distribution to the known discrete levels at excitation energy $E_x = E_d$. The spin cut off

parameter at the neutron separation energy, $\sigma(S_n)$, is not explicitly defined and is often taken from other spin cut off models such as Eq. (2.7), (2.8) or (2.9).

The spin distribution is notoriously difficult to measure as there are few direct observables, though some results inferred from neutron evaporation spectra exist [21]. Within the Oslo method, the reliance on model predictions for spin distributions often yield the largest source of systematical uncertainty. Model dependence enters the Oslo method as part of the normalization explained in Chapter 4. The uncertainties and impact of having to rely on model predictions for the spin distribution are subject in both Paper I and Paper II.

γ-ray strength function

The time it takes an excited energy level to decay is its lifetime, τ. The inverse of the lifetime, $\lambda = 1/\tau$, is the decay rate. Excited levels are not stationary states, thus their energy will be subject to the Heisenberg uncertainty principle, $\Delta E \Delta t \geq \hbar$. The uncertainty of the energy level, its width, is related to the lifetime by $\Delta E = \Gamma = \hbar/\tau = \hbar\lambda$. When the excited level decays, the total width of the level, Γ, will be the sum of all partial widths as $\Gamma = \sum_i \Gamma_i$. The branching ratio to a particular level is the ratio of partial to total width, Γ_i/Γ.

The γ-ray strength function is defined as [22]

$$f_{XL}(E_\gamma, E_i, J_i, \pi_i) = \frac{\langle \Gamma_\gamma^{XL} \rangle (E_\gamma, J_i, \pi_i)}{E_\gamma^{2L+1}} \rho(E_i, J_i, \pi_i), \tag{2.11}$$

for each multipolarity $X = E$ or M and $L = 1, 2, 3$, etc. $\langle \Gamma_\gamma^{XL} \rangle (E_\gamma, J_i, \pi_i)$ is the average partial width for decay with γ-ray energy E_γ from the initial levels in excitation bin, E_i, with spin and parity J_i^π. $\rho(E_i, J_i, \pi_i)$ is the density of initial levels. At the excitation energies subject to this thesis, the γ-ray strength function is strongly dominated by dipole transitions ($L = 1$). From here on, only dipole strength is considered.

As originally defined, the γ-ray strength function depends on the γ-ray energy, initial excitation energy, spin and parity. In addition, there is a distinction between upward strength describing excitation due to photo-absorption and downward strength describing decay. In 1955, David Brink hypothesised in his doctoral thesis that the cross-section for photo-absorption should have the same shape regardless of whether the nucleus is in its ground state or an excited state [23]. The hypothesis was further expanded upon by Peter Axel in 1962 [24] in what is commonly known as the generalized Brink-Axel hypothesis. The hypothesis essentially states that the γ-ray strength function is independent of initial excitation energy, spin, parity and direction (upwards or downwards), meaning that

$$f(E_\gamma, E_i, J_i, \pi_i) = f(E_\gamma). \tag{2.12}$$

Within the Oslo method, the γ-ray strength function is extracted from a wide range of initial excitation energies, implicitly assuming the general Brink-Axel hypothesis. The validity of the hypothesis has been the subject of great debate,

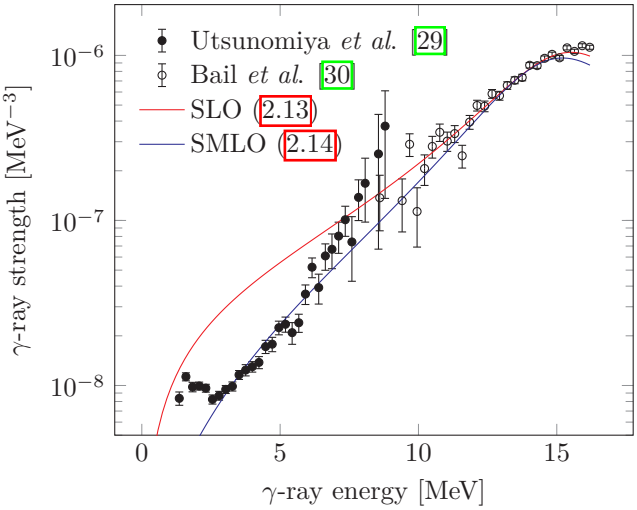

Figure 2.1: γ-ray strength function in ^{98}Mo measured with the Oslo method (closed circles) [29] and by photo-excitation (open circles) [30]. The red line shows the SLO model with parameters taken from RIPL-3 [13] while the blue line shows the SMLO model [31, 32].

with some experimental results favouring the hypothesis [25–27] and some results claiming the opposite [28].

The dipole γ-ray strength function of most nuclei is dominated by a few resonance-like features. The electric dipole strength function is dominated by a large resonance known as the electric giant dipole resonance (GDR), typically centered around 15 to 20 MeV depending on the mass of the nucleus. At the macroscopic scale, the GDR is understood as the result of collective motions of neutrons and protons oscillating against each other. There are many models seeking to describe the shape of the GDR, the simplest being the standard Lorentzian (SLO) [22, 23]:

$$f_{\mathrm{SLO}}(E_\gamma) = \frac{\sigma_r}{3\pi^2\hbar^2c^2}\frac{E_\gamma\Gamma_r^2}{(E_\gamma^2 - E_r^2)^2 + E_\gamma\Gamma_r^2}, \tag{2.13}$$

where E_r is the centroid energy, Γ_r the width and σ_r the peak cross section. Although effective at describing the γ-ray strength close to the GDR peak, the SLO often breaks down at lower γ-ray energies. Often the strength gets over-estimated as illustrated in Figure 2.1. Better reproduction can be obtained with the simple modified Lorentzian (SMLO) [31, 32]

$$f(E_\gamma) = \frac{1}{3\pi^2\hbar^2c^2}\frac{\sigma_r\Gamma_r}{1-\exp\left(-E_\gamma/T\right)}\frac{E_\gamma\Gamma(E_\gamma,T)}{(E_\gamma^2 - E_r^2)^2 + \Gamma^2(E_\gamma,T)E_\gamma^2}, \tag{2.14}$$

where the width of the resonance,

$$\Gamma(E_\gamma, T) = \frac{\Gamma_r}{E_r}\left(E_\gamma + \frac{4\pi^2}{E_r}T^2\right), \tag{2.15}$$

depends on both the γ-ray energy and the nuclear temperature at the final level. The temperature dependence of the SMLO means that it does not strictly comply with the assumptions of the Brink-Axel hypothesis. Nevertheless, the formula is effective at describing the shape of the GDR as seen in Figure 2.1, and has been shown to systematically reproduce experimental data [32, 33].

In addition to the GDR, the electric dipole strength sometimes features a smaller, more narrow resonance known as the Pygmy dipole resonance (PDR), typically centered around $6 - 10$ MeV. The PDR is usually associated with more neutron-rich nuclei and has been suggested to be induced by neutron skin oscillation [34].

The magnetic dipole strength of nuclei is typically much lower than its electric counterpart. The largest contributor to the magnetic dipole strength is the giant magnetic dipole resonance (GMDR). It is caused by particle-hole excitations between $j = l \pm 1/2$ orbitals and typically occurs at about $6 - 8$ MeV [35]. Deformed nuclei feature the Scissors resonance [36] at γ-ray energies around $2-4$ MeV and is understood to originate from the protons and neutrons oscillating against each other in a scissor-like motion. Systematic behaviour of the Scissors resonance has been studied extensively with the Oslo method [37–40].

In 2004, Voinov *et al.* [8] observed a large increase in the γ-ray strength function as the γ-ray energy decreased in the results from an Oslo method experiment on ^{56,57}Fe. At the time, this observation was contrary to the general belief that the γ-ray strength function should continue to decrease [8]. The structure is usually referred to as the low energy enhancement (LEE) or the upbend. In the years since the initial discovery, similar enhancements have been observed in several nuclei from Sc to Mo and Sm [9, 10, 33, 41]. Initially, the observation was met with scepticism, but the debate was resolved with the observation of a similar enhancement in ^{95}Mo by Wiedeking *et al.* in 2012 using an independent method [42], confirming the results of Ref. [41]. Examination of the angular distribution of γ-rays revealed that the enhancement is due to dipole transitions [43]. There have been attempts to experimentally determine if the enhancement is electric or magnetic in nature, though results so far have been inconclusive [44]. There are also theoretical attempts at describing the enhancement, with one model suggesting both an electric character [45] while shell model calculations suggest magnetic character [46].

Microscopic descriptions of the nuclear level density and gamma-ray strength function

Thus far, the focus has been on semi-empirical macroscopic models and explanations for the shapes and features found in the NLD and γSF. Approaching the subject from the perspectives of shell model and many-body quantum

mechanics should provide a more physically informed description of the features seen in the NLD and γSF. The following section briefly introduces the most central concepts of many-body quantum mechanics and the nuclear shell model. A more comprehensive introduction to the subject can be found in the book *From Nucleons to Nucleus* by Jouni Suhonen [47].

Most microscopic models of the nucleus usually start out with the mean-field approximation, in which it is assumed that the potential that a single nucleon experiences can be reduced to a central potential V_{MF}. This potential arises from its mean interactions with the $A-1$ other nucleons within the nucleus. Using a Woods-Saxon potential and a spin-orbit interaction results in the typical orbitals found in the shell model. The Schrödinger equation for the nucleus is reduced to a system of A non-interacting fermions in a common potential and its wave function simply being the product of A single-particle wave functions. With the mean field approximation alone, many observed phenomena are well described, such as the magic numbers, spins and parities of most even-even and even-odd nuclei.

A model of the nucleus with no interactions between the nucleons is unfortunately too simplistic and will not be able to reproduce most of the excited levels. However, adding a residual interaction, V_{res}, to the nuclear potential, corresponding to the interaction of nucleons with neighbouring nucleons gives a much more realistic results. The starting point for evaluating such a model is the Hartree-Fock method. Slater determinants, which are the antisymmetrized product of the mean field single particle wave functions,

$$\Phi_n(\boldsymbol{r}_1,\ldots,\boldsymbol{r}_A) = \mathcal{A}\left[\prod_{i=1}^{A}\phi_{\alpha_i}(\boldsymbol{r}_i)\right], \tag{2.16}$$

are used as the basis for the many-body wave function of the nucleus. $\mathcal{A}$ is an antisymmetrization operator responsible for ensuring the wave functions complies with the Pauli principle and ϕ_{α_i} is the single particle wave function. Eigenstates and wave functions of the nucleus are found by diagonalizing the Hamiltonian in this basis. Once the wave functions of the nucleus are found, the level density can be deduced by counting the number of levels. The γ-ray strength function is found by applying the appropriate electromagnetic operator to get the transition strength between levels.

As the number of nucleons in the nucleus increases, so do the dimensions of the Slater determinants. After only a dozen or so nucleons, the dimentionality of the problem becomes so immense that it is practically impossible to solve and approximations have to be made. Still, wave functions and eigenvalues can be obtained by strategically freezing out degrees of freedom. The simplest approach is to assume an inert core, usually a doubly-magic nucleus, and only allow interactions between the valence nucleons in orbitals outside of the core. The number of orbitals outside the core has to be limited such that the dimensions of the problem are manageable. Typically, this means only orbitals within the same major shell will be included. $E1$ transitions require a change in parity and since most shell model calculations are truncated to a single major shell,

these calculations often only provide strength for $M1$ and $E2$ transitions. In Paper I, such large shell model calculations within a limited model space were performed with a ^{78}Ni core and effective interaction described in Refs. [48, 49] and references within, to investigate if the low energy enhancement of ^{87}Kr could be replicated. Results from similar calculations [50] were compared with the experimental γ-ray strength function of ^{63}Ni and ^{67}Ni in Paper II and Paper III, respectively.

Imposing further restrictions on the types of excitation available (e.g. only single particle-hole excitation, two particles-two holes, etc.), and other approximations has lead to a myriad of methods and formalisms. Some of these are the Hartree-Fock-Bogoliubov (HFB) [51], random-phase approximation (RPA) [52], quasiparticle random-phase approximation (QRPA) [53], etc. The specifics of these methods are beyond the scope of this thesis. In general, they will not be as accurate as direct diagonalization of the Hamiltonian, though they may operate with more orbitals allowing for predictions of $E1$ strength.

Nuclear reactions

Nuclear reactions are complicated. The probabilities for different outcomes are determined by numerous factors such as the structures of the target and residual nuclei and the energy of the projectile. Reactions typically fall under one of three categories: direct, pre-equilibrium or compound. The major distinction between these types of reactions is the number of nucleons involved and the timescale. In the case of direct reactions, only a small number of nucleons will be involved and the time scale will be comparable with the time it takes the projectile to traverse the diameter of the target nucleus. On the contrary, compound reactions will involve most, if not all, nucleons as the energy of the projectile will be distributed and a compound nucleus in thermal equilibrium is formed. As the projectile energy is distributed amongst the other nucleons, the compound nucleus forgetshow it was formed. The decay of the compound nucleus is independent of how it was made, depending only on energy, spin and parity conservation laws. Thus, the cross section for creating a compound nucleus is independent of how it decays, and the cross section for a particular reaction with incoming channel a and outgoing channel b can be separated as

$$\sigma(a,b) = \sigma_a^{\mathrm{CN}} P_b \tag{2.17}$$

where σ_a^{CN} is the cross section for the formation of the compound nucleus and P_b is the probability of its decay with outcome b. Conversely, direct reactions will have strong correlations between the incoming projectile and final outcome of the reaction. The last category, pre-equilibrium reactions, are reactions where the projectile and target nuclei will not reach thermal equilibrium before decaying, thus retaining features of both direct and compound reactions.

The rest of this section will concern mainly neutron capture reactions at neutron energies relevant for neutron capture processes responsible for the nucleosynthesis of heavy elements [3]. Typical energies for such reactions range

from a few eV up to a few keV. At these energies, compound reactions will be the dominant reaction mechanism.

Hauser and Feshbach presented in 1952 a framework that enables calculations of the compound reaction cross section from level densities and γ-ray strength functions [1]. Within the Hauser-Feshbach framework, the cross section for a compound nucleus being formed when a neutron hits the target nucleus is calculated within the optical model. Once formed, the excited compound nucleus could have many decay channels open, but for neutron energies below an MeV or so, there are usually only two possible decay paths. Re-emitting a neutron or emitting γ rays, trapping the neutron inside the compound nucleus. Simplified, the capture cross section given by the Hauser-Feshbach theory will be

$$\sigma(n,\gamma) = \sigma_n^{\mathrm{CN}} \frac{T_\gamma}{\sum_f T_f}, \tag{2.18}$$

where

$$T_\gamma = \sum_{XL} \int_0^{S_n+E_n} 2\pi E_\gamma^{2L+1} f_{XL}(E_\gamma) \sum_{J,\pi} \rho(S_n + E_n - E_\gamma, J, \pi) dE_\gamma \tag{2.19}$$

is the total transmission coefficient for γ-ray decay and $\sum_f T_f$ is sum over all possible final outcomes.

In Paper I and Paper III, the neutron capture rates of ^{86}Kr and ^{66}Ni were calculated with the TALYS reaction code [54], respectively. Providing experimental NLDs and γSFs allowed for considerable containment of the capture rates and cross-sections.

Chapter 3

Detectors and data acquisition

In 2001, a new type of inorganic scintillator detector was discovered - the cerium-doped $LaBr_3$ crystal [55]. It soon become apparent that this material has exceptional properties as a γ-ray detector. $LaBr_3$:Ce has an extremely high light yield of more than 6.1×10^4 photons per MeV and exceptional timing properties of the order of only a few hundred picoseconds. The relatively high density and high proton number of the material gives it a high efficiency for high-energy γ-ray detection.

The high scintillation light yield of the $LaBr_3$:Ce material results in most photo multiplier tubes (PMTs) quickly saturating. Therefore, specific low gain PMTs have to be used. High stability, high-voltage power supplies capable of providing high currents are required to ensure the PMT remains linear for all γ-ray energies [56, 57].

The OSCAR array

The nuclear physics group at the University of Oslo was awarded a 25M NOK grant to develop and implement a new γ-detector array in 2016. A part of this thesis work was to commission the new detectors and its accompanying electronics.

The Oslo SCintilator ARray (OSCAR) consists of 30 large-volume $LaBr_3$:Ce detectors (3.5×8-inch) and replaced the old NaI-detector based CACTUS array. Each of the 30 $LaBr_3$:Ce crystals, PMTs and voltage dividers were characterized to determine the optimal operational voltages, resolution performance etc. Together with the new detectors, a new versatile support frame for the detectors was built. The project saw the creation of a new reaction chamber to house the targets and the Silicon Ring (SiRi) [58] particle telescope. A picture of the OSCAR array is shown in Figure 3.1. Figure 3.2 presents a picture of the new target chamber with the SiRi telescope mounted at backwards angles.

Accompanying the new detector array, a new data acquisition system was also commissioned. This system consisted of seven new Pixie−16 digital pulse processing modules from XIA, with two modules featuring 500 MHz analog-to-digital converters (ADCs) and the rest of the modules having 250 MHz ADCs. A picture of the electronics rack is shown in Figure 3.3. The power provided to the electronics is isolated by a transformer to avoid any unwanted coupling. Detector signals are continuously sampled and all processing such as triggering, energy and time filtering is done digitally in real time. To read out the modules, new programs `XIAengine` and `XIAonline` were developed. `XIAengine` is responsible for communicating with the XIA modules, storing list-mode data to disk. It also provides a simple graphical user interface for modifying settings such as shaping

Figure 3.1: The OSCAR γ-detector array consisting of 30 large-volume $LaBr_3$:Ce detectors.

time, trigger thresholds, etc. The `XIAonline` program monitors the data read out in real time and performs an online analysis for diagnosis and monitoring of the experiment. The entire DAQ software suite is open source and available online [59].

The OSCAR array coupled with the SiRi detectors represents the ideal experimental setup for Oslo-method-type experiments. A light ion beam of e.g. protons or α particles is provided by the MC-35 Scanditronix cyclotron impinges on a target producing a highly excited compound nucleus. Fragment particles from the reaction (e.g. protons, deuterons, etc.) are emitted and hits the SiRi particle telescope. SiRi consists of a thin (130 μm) ΔE detector and a thick (1550 μm) E detector. From the energy deposited in the two detectors, the particle species are identified and the reaction channels can be selected. From simple two-body scattering kinematics, the excitation energy of the residual excited nucleus is determined from the measured energy and scattered angle of the fragment particle [60]. Coincident γ-rays are selected by gating on the prompt time peak. A matrix of excitation energy versus γ-ray energy is constructed from these coincidences. Such matrices are the raw input data for the Oslo method presented in Chapter 4.

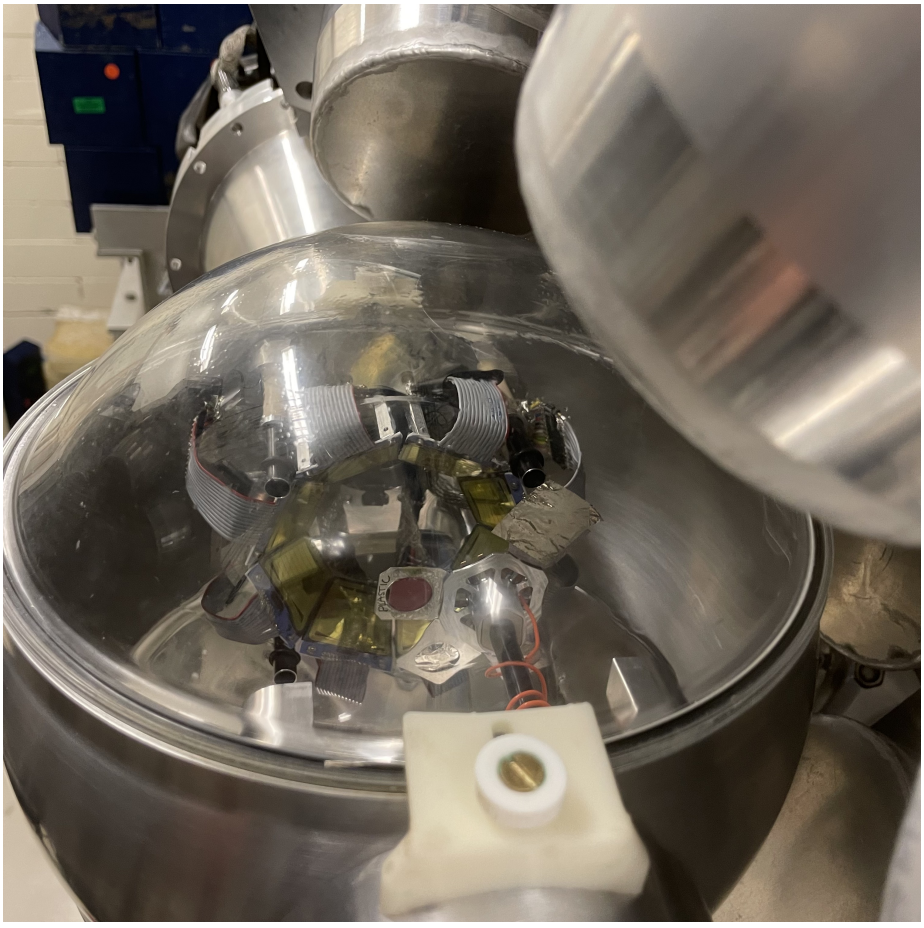

Figure 3.2: New target chamber made for the OSCAR array. A variety of targets are mounted on the target wheel in front of the SiRi particle telescope.

The Fast Timing Array

With the exceptional timing properties and the high resolution of $LaBr_3$:Ce, it has become feasible to directly measure lifetimes of excited states at the picosecond scale. A new detector array consisting of eight 2×2-inch $LaBr_3$:Ce detectors was commissioned in 2017 at iThemba LABS. During the commissioning, several measurements with radioactive sources such as ^{60}Co, ^{152}Eu, ^{22}Na and ^{133}Ba were performed to characterize the energy resolution and the coincident resolving time (CRT) of the detectors. Signals from the detectors were processed by a 500 MHz, 14-bit Pixie−16 DGF module from XIA. Results of these measurements are presented in Paper IV. In addition to the source measurements, an in-beam commissioning experiment with a 27 MeV proton beam was carried out at the

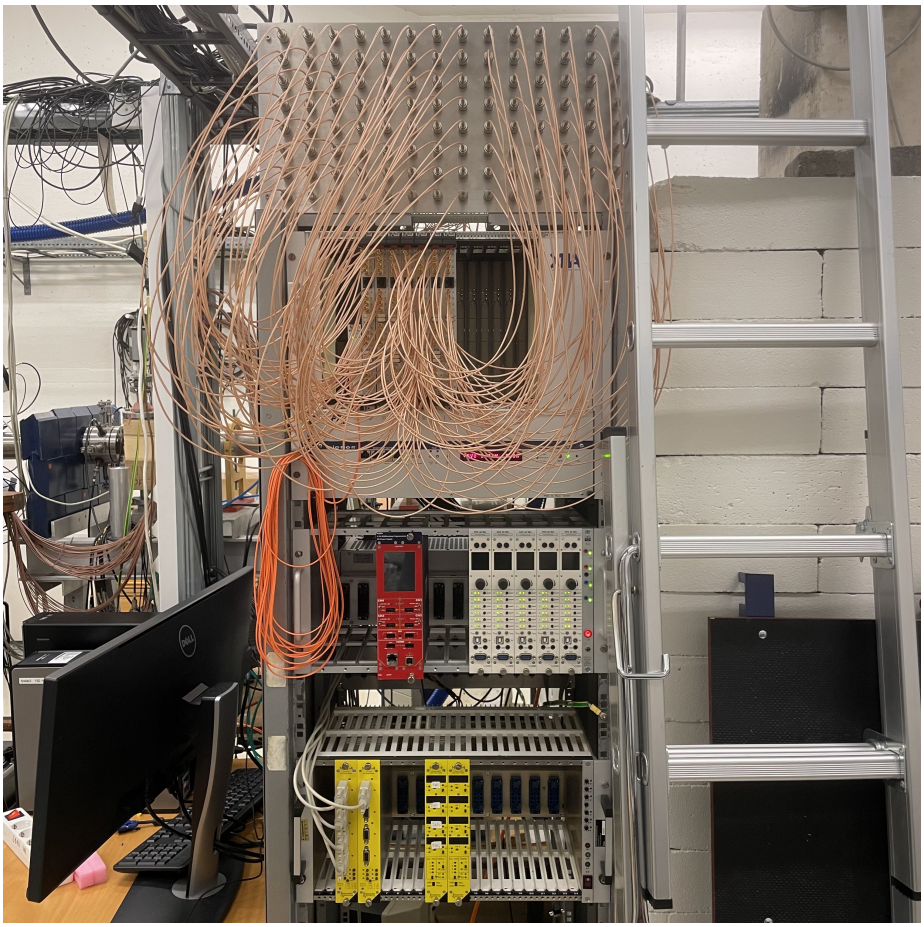

Figure 3.3: Rack with all the electronics powering the OSCAR and SiRi array. On the top, a patch panel provides easy access to the detector signals that are connected to the XIA modules mounted in the crate directly below. In the NIM crate below, the power supplies for the OSCAR detectors are mounted and the bottom NIM crate has the power supply for the SiRi detectors and pre-amplifiers. The desktop computer to the left is responsible for the readout of the XIA modules over a fiber optic interface, ensuring electric separation.

AFRODITE array [61] at iThemba LABS. The experiment had six of the 2×2-inch $LaBr_3$:Ce detectors mounted in the AFRODITE frame together with eight Compton-suppressed High-Purity Germanium (HPGe) CLOVER detectors. An additional two large volume $LaBr_3$:Ce detectors on loan from the University of Oslo were also used. Deuteron-γ coincidences were measured following (p, d) reactions on a ^{45}Sc and a ^{64}Ni target. The deuterons were measured by two annular silicon detectors of the S2 type mounted at forward angles. The results from the ^{64}Ni$(p, d)^{63}$Ni reactions were analyzed with the Oslo method and are the subject of Paper II. During work on this thesis, the FTA detectors were characterized and the lifetime of the first-excited state in ^{152}Sm was measured and is presented in Paper IV. In-beam measurements with the ^{45}Sc target were analyzed to obtain the in-beam characteristics of the detectors. This work was done as part of the PhD project of Lumkile Msebi [62].

Chapter 4

The Oslo method

The starting point for the Oslo method are the excitation energy versus γ-energy matrices measured in experiments, as described in Chapter 3. An example of such a matrix is shown in Figure 4.1. The unfolding method [63] is applied to raw excitation-γ matrices to account for the detector response, producing the unfolded matrix. Applying the first generation method [64] to the unfolded matrix produces the first-generation matrix which the NLD and γSF are extracted from. In this chapter, the steps of the Oslo method will be presented, starting with the unfolding method.

The unfolding method

The γ-ray spectra found in the raw excitation energy versus γ-ray energy matrices is the detector's response to the true spectrum of incident γ-rays. The raw spectrum is often referred to as the *folded* spectrum, f, and the spectrum of incident γ-rays as the *unfolded* spectrum, u. The folded spectrum will be related to the unfolded by

$$f = \boldsymbol{R}u, \tag{4.1}$$

where $\boldsymbol{R}$ is the response of the detector. If the folded (f) and unfolded (u) spectrum are represented as vectors, the process of recovering the unfolded spectrum becomes a matrix inversion problem. However, directly inverting the response matrix will lead to unphysically large fluctuations and introduce unwanted artificial structures. Using an iterative method to invert the spectrum reduces the amount of artificial structures significantly. The algorithm starts out with an initial unfolded test spectrum equal to the experimental raw spectrum: $u^{(0)} = f$. Each iteration of the method will do the following steps:

1. Fold the n^{th} test spectrum $u^{(n)}$ by the detector response, $f^{(n)} = Ru^{(n)}$
2. Calculate the new test spectrum $u^{(n+1)} = u^{(n)} + (f - f^{(n)})$
3. Continue until $f^{(k)} \sim f$

The resulting unfolded spectrum from this iterative process, $u^{(k)}$, features strong artificial fluctuations relative to the expected $\sqrt{N}$ Poisson fluctuations. To reduce the fluctuations to a more realistic level, the unfolded spectrum $u^{(k)}$ is used to determine the Compton-scattering contribution to the raw spectrum. The resulting Compton spectrum is smoothed and, together with contributions from single/double-escape and annihilation processes, is subtracted from the raw spectrum. This leaves only counts due to full-energy deposition. The unfolded spectrum is found by dividing by the probability of full-energy deposition and

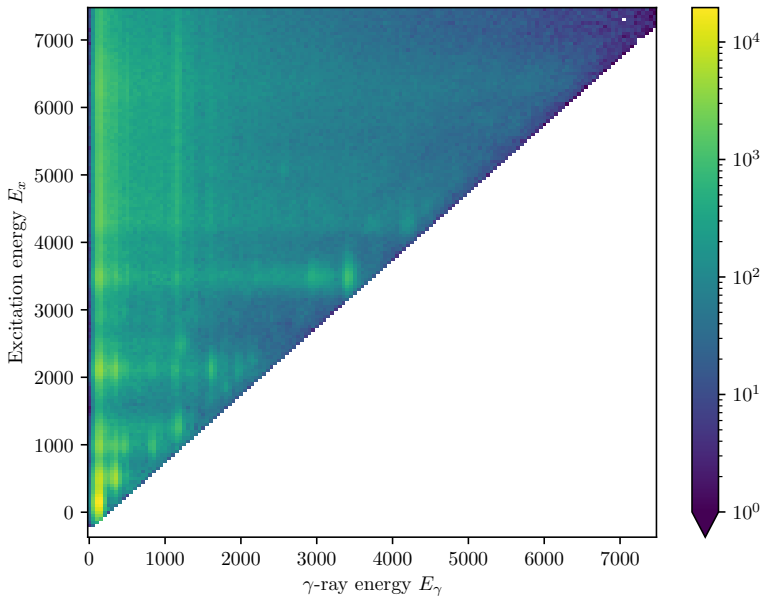

Figure 4.1: Background-subtracted excitation versus γ-ray energy matrix for ^{63}Ni. The matrix has been cut along the diagonal of $E_\gamma = E_x + \Delta E$ ($\Delta E = 240$ keV) to emphasis features. Figure is taken from Paper II.

the absolute efficiency of the detector. Applying the unfolding method on the matrix shown in Figure 4.1 results in the unfolded matrix shown in Figure 4.2.

The ideal response matrix is measured by producing mono-energetic γ rays in the experimental setup at all relevant energies. In practice, few mono-energetic γ-ray energies can be produced, and between these energies, the response spectrum has to be interpolated. The measured responses are typically supplemented by simulating the experimental setup using packages such as `Geant4` [65]. In Paper I, Paper II and Paper III there were no response matrices measured for the setups. Models of the experimental setups were implemented in `Geant4` to produce the response matrices required for the analysis. The source code of these simulations is available on GitHub [66, 67].

The first generation method

Each excitation bin contains the γ-ray spectrum of all γ-rays emitted during cascades depopulating a level within the excitation-energy bin. However, information about the nuclear level density and γ-ray strength function is only contained within the distribution of the first γ-ray of the cascades. To

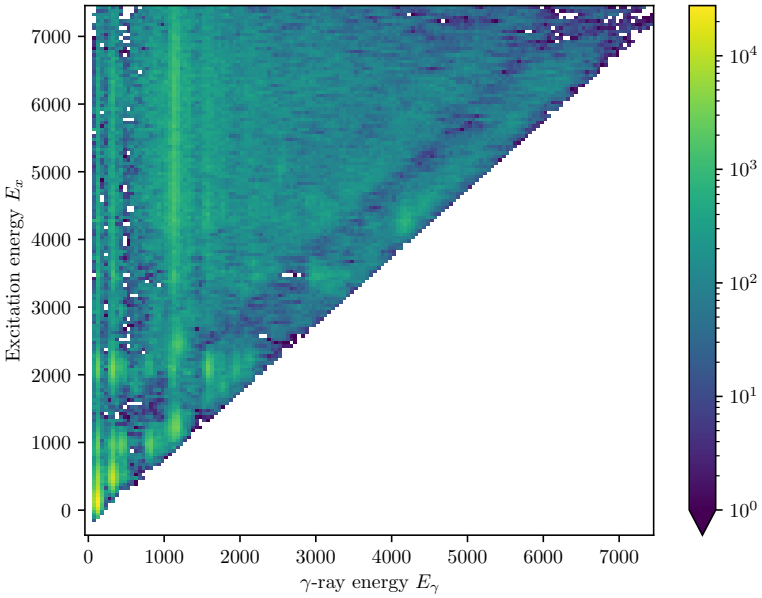

Figure 4.2: Unfolded excitation versus γ-ray matrix for ^{63}Ni. Figure taken from Paper II.

recover the first generation matrix the first generation method [64] is applied to the unfolded matrix. The main assumption of the first generation method is that the γ-ray distribution of decays from levels within a particular excitation-energy bin are independent of how the bin was populated, i.e. the same distribution of first generation γ rays regardless of whether the bin was populated directly in a reaction or it was populated as part of a γ cascade. Based on this assumption, each excitation-energy bin will contain the first generation γ rays plus γ rays depopulating all excitation-energy bins with less excitation energy. Thus, the distribution of first generation γ rays emitted from each excitation-energy bin may be recovered by subtracting the spectra from excitation-energy bins with less excitation energy. The subtraction need to be weighted by the relative population of the underlying bins from the initial excitation-energy bin. Applying the first generation method on the unfolded matrix from ^{63}Ni results in the first generation matrix seen in Figure 4.3.

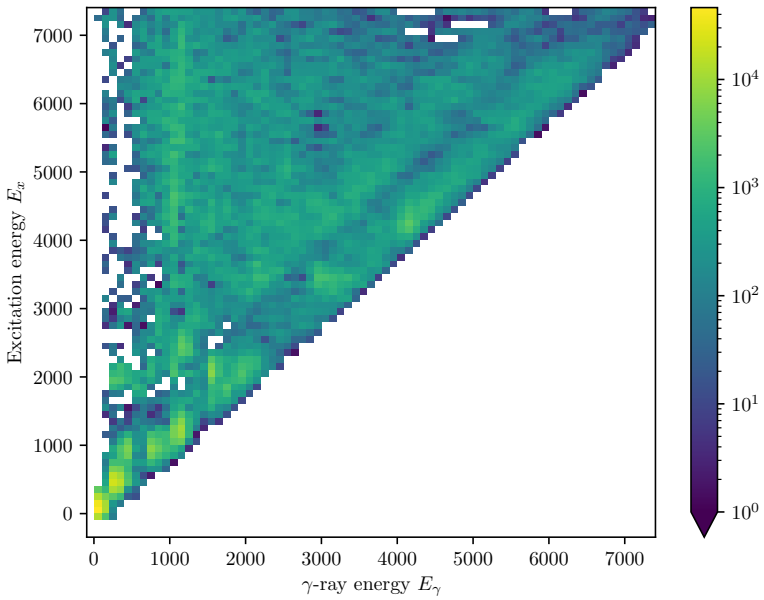

Figure 4.3: First generation matrix for ^{63}Ni. Figure taken from Paper II.

Extraction of nuclear level density and γ-ray strength function

The first generation matrix is proportional to the γ-ray transmission coefficient and the nuclear level density at the final excitation energy [7]

$$P(E_x, E_\gamma) \propto \mathcal{T}(E_\gamma)\rho(E_x - E_\gamma), \tag{4.2}$$

where P is the first generation matrix, $\mathcal{T}(E_\gamma)$ is the γ-ray transmission coefficient and $\rho(E_x - E_\gamma)$ is the nuclear level density at the final excitation energy.

Based on this relation, a theoretical normalized first generation matrix is given by:

$$P_{\text{teo}}(E_x, E_\gamma) = \frac{\mathcal{T}(E_\gamma)\rho(E_x - E_\gamma)}{\sum_{E_\gamma = E_\gamma^{\min}}^{E_x} \mathcal{T}(E_\gamma)\rho(E_x - E_\gamma)}, \tag{4.3}$$

where the transmission coefficient $\mathcal{T}(E_\gamma)$ and $\rho(E_x - E_\gamma)$ are free parameters for each γ-ray energy bin and final excitation energy $E_f = E_x - E_\gamma$ bin, respectively. The nuclear level density and γ-ray transmission coefficients are determined by

minimizing

$$\chi^2 = \sum_{E_x, E_\gamma} \left(\frac{P(E_x, E_\gamma) - P_{\text{teo}}(E_x, E_\gamma)}{\sigma_P(E_x, E_\gamma)} \right)^2 . \tag{4.4}$$

The limits of excitation energy and γ-ray energy are chosen to ensure that only statistical decay is included.

A side effect of the proportionality is that the γ ray spectrum for each excitation-energy bin in the first generation matrix needs to be normalized. The normalization results in the theoretical first generation matrix becomes invariant under transformation [7]:

$$\begin{aligned} \rho(E_x) &= A\widetilde{\rho}(E_x)e^{\alpha E_x} \\ \mathcal{T}(E_\gamma) &= B\widetilde{\mathcal{T}}(E_\gamma)e^{\alpha E_\gamma} \end{aligned} \tag{4.5}$$

where A, B and α are transformation parameters. This symmetry means that there are an infinite number of solutions that minimize Eq. (4.4) and the challenge becomes finding the actual physical solution.

Normalization

Since the first generation matrix only provides the functional shape of the NLD and γSF, comparison with auxiliary data is necessary to obtain the physical solution. Typical external data used for comparison are the level density found by counting the known resolved levels, and the level density at the neutron separation energy. The NLD at the neutron separation energy is found by inverting the neutron s-wave resonance spacing D_0: [7]

$$\rho(S_n, J_t + 1/2, \pi_t) + \rho(S_n, J_t - 1/2, \pi_t) = \frac{1}{D_0}, \tag{4.6}$$

where J_t and π_t are the ground state spin and parity of the $A-1$ nucleus, respectively. The total level density at the neutron separation energy is recovered by dividing by the spin and parity distributions

$$\rho(S_n) = \frac{2}{g(S_n, J_t + 1/2) + g(S_n, J_t - 1/2)} \frac{1}{D_0}. \tag{4.7}$$

This is where the first systematic errors due to model assumptions are introduced. As discussed in Chapter 2, the spin distribution is, in most cases, unknown, necessitating model predictions to determine the total level density at the neutron separation energy. In Paper I and Paper II the spin distribution was given by the Ericson distribution, Eq. (2.3), and the spin cut-off parameter at the neutron separation energy was an average of the theoretical models given by Eqs. (2.7), (2.8) and (2.9).

The first generation matrix probes the level density at the final excitation energy, meaning that the level densities extracted only extend up to $E_f = E_x^{\max} - E_\gamma^{\min}$, where $E_x^{\max}$ is the maximum excitation-energy bin included in the

extraction and $E_\gamma^{\min}$ is the lowest γ-ray bin included. Comparing the extracted level density from the first generation matrix to the one found at the neutron separation energy requires an interpolation connecting the two regions. In most cases, this is done using the constant temperature formula, Eq. (2.6).

The average total radiative width of s-wave neutron resonances are related to the nuclear level density and γ-ray strength function by

$$\langle \Gamma_\gamma \rangle = \frac{D_0}{2} \int_0^{S_n} E_\gamma^3 f(E_\gamma) \rho(S_n - E_\gamma) \sum_{l=-1}^{l=1} g(S_n - E_\gamma, J_t + l) dE_\gamma, \tag{4.8}$$

where J_t is the spin of the ground state of the $A-1$ nucleus. The normalization parameter B, determining the absolute value of the extracted γ-ray strength function, is constrained by comparing the calculated average radiative width, Eq. (4.8), with the experimental values found in neutron resonance experiments. The γSF is only extracted between γ-ray energies $E_\gamma^{\min}$ and $E_x^{\max}$. Between 0 and $E_\gamma^{\min}$ the strength is extrapolated using $f(E_\gamma) = C_0 e^{-\eta_0 E_\gamma}$. The function $f(E_\gamma) = C_1 e^{-\eta_1 E_\gamma}/E_\gamma^3$ is used between $E_x^{\max}$ and the neutron separation energy. Errors due to poor extrapolation are expected to not exceed 15% [68].

In Paper I and Paper II, neutron s-wave parameters are experimentally known and the level densities and γ-ray strength functions are normalized as explained above. In the case of ^{67}Ni presented in Paper III, there is no experimental resonance data available. The situation is further complicated by the lack of a reliable level scheme to produce discrete level densities. The solution was to rely on the NLD from large-scale shell model calculations for the low energy normalization point. Model predictions for the level density at the neutron separation energy were used instead of s-wave resonance spacing. The absolute value of the γ-ray strength was determined by extrapolating from the experimental γ-ray strength of ^{68}Ni using both the SMLO model [32] and the Gogny-HFB+QRPA model [53].

A major drawback of the Oslo method is the dependence on external data to normalize the level density and γ-ray strength function. A new, novel approach combining the Shape method [69] with the Oslo method has shown that the slope (α parameter in Eq. (4.5)) of the level density and γ-ray strength function can be constrained without the need of any auxiliary data [70].

Chapter 5

Inverse kinematics

The standard way of performing Oslo method experiments is by employing light ion beams that impinge on thin target foils, causing scattering or nucleon transfer reactions. The light fragment particles from the reaction are measured with silicon detectors configured such that there is a thin ΔE detector in front of a thicker E detector. The particle species can then be identified from the energy deposited in the two detectors. The excitation energy of the residual excited nucleus is determined from the fragment energy and scattering angle using simple two-body kinematics (e.g. Chapter 11 in [71]) and coincident γ rays are measured with γ-ray detectors.

As briefly touched upon in the introduction, this approach has limitations as to what nuclei can be studied. Since these experiments rely on stationary targets, the material used to produce the targets has to be both chemically and radioactively stable and of a high isotopic purity. An experimental setup where light beams are employed cannot be used on elements such as noble gases or reactive elements such as alkali or halogens. An alternative approach is to accelerate heavy ion beams to impinge on a deuterated plastic target, essentially interchanging the target and the beam used in the standard Oslo method type experiments. This type of experiment is often referred to as *inverse kinematics*.

In normal kinematics (meaning light ion beam and heavy target), the center-of-mass (momentum) (CM) frame is approximately the laboratory frame, but with inverse kinematics, the CM frame will have a significant velocity. Relativistic effects such as Lorentz boosts and Doppler shifts become significant. A consequence of the Lorentz boost is that the residual excitation energy becomes strongly correlated with the laboratory scattering angle of the fragment. This is illustrated in Figure 5.1, where the colour shows the excitation energy of ^{67}Ni as a function of the proton laboratory angle and energy after a d(^{66}Ni, p)^{67}Ni reaction. This is in contrast to Figure 5.2, which shows the excitation energy of ^{67}Ni, but with normal kinematics. The large angular dependence in forward angles requires careful planning in terms of particle detector array placement and beam energy. Particular focus has to be given to ensure that all excitation energies between the first-excited state and the neutron separation energy are measured.

The highly excited residual nucleus will have considerable velocity after the reaction and the emitted γ rays will be Doppler shifted. Fortunately, due to the large mass difference between the projectile (e.g. ^{66}Ni) and the target (e.g. deuterons) the momentum transfer will be small. Depending on energy and mass, the scattered angle will be of the order on a few degrees. The change in velocity will be dominated by the slowing down of the beam particles. Disregarding the slowing down in the target, Figure 5.3 shows the laboratory velocity and

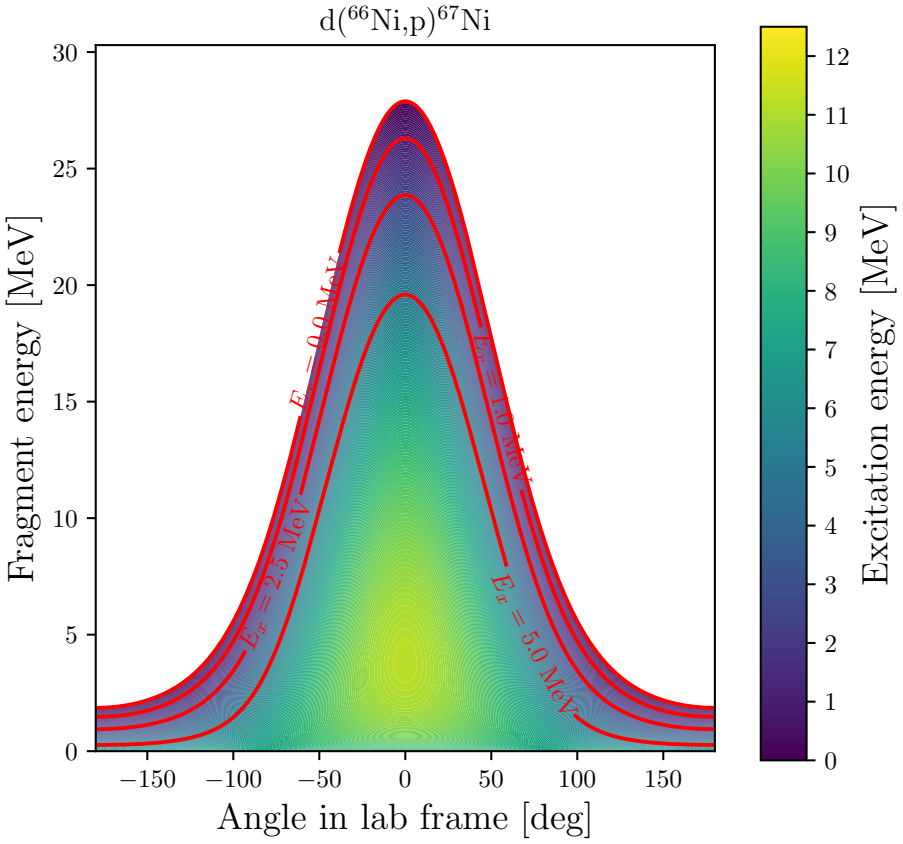

Figure 5.1: Excitation energy of ^{67}Ni as a function of proton energy and scattering angle in laboratory frame following a d(^{66}Ni, p)^{67}Ni reaction with 295 MeV ^{66}Ni beam.

scattered angle of ^{67}Ni after a d(^{66}Ni, p)^{67}Ni reaction.

With a small change of the residual velocity and scattered angle, the corrections necessary to account for Doppler shift can greatly be simplified. Assuming no scattering and constant velocity for all events reduces the Doppler corrections to a constant factor that only depends on the angle of the γ-ray detector relative to the beam axis.

When ions impinge on a target, part of their kinetic energy will be deposited as heat in the target material. For most metallic targets, this heating will be quickly dissipated to the surroundings. However, Plastic targets suffer from poor thermal conductivity, thus the beam will melt the target if sufficiently intense. Polyethylene target are therefore not well suited for high beam intensities. During

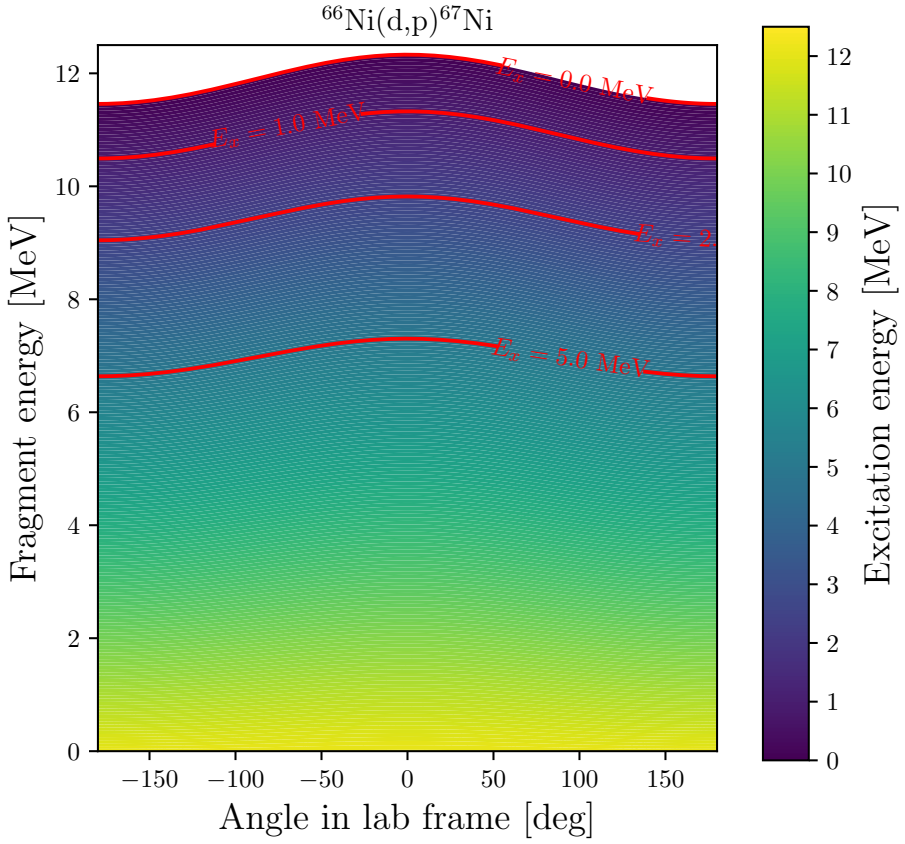

Figure 5.2: Excitation energy of ^{67}Ni as a function of proton energy and scattering angle in laboratory frame following a ^{66}Ni(d, p)^{67}Ni reaction with 9 MeV deuteron beam. The red contour lines shows 0, 1, 2.5 and 5 MeV excitation energy.

the Kr experiment presented in Paper I, the targets usually lasted a few hours before they had to be switched out. Intuitively thinner targets should last longer since less energy will be deposited. However, during the experiment the thicker targets tended to last longer before count rates got critically low. In the ^{66}Ni beam experiment presented in Paper III, this was not an issue and the same target could be used throughout the entire experiment.

With polyethylene targets, 1/3 of all particles in the target is carbon. Fusion between the beam and carbon could occur in inverse kinematics experiments which would result in hard-to-remove background. In the krypton experiment performed at iThemba LABS and the nickel experiment at CERN ISOLDE there was no clear evidence of any strong background due to fusion evaporation.

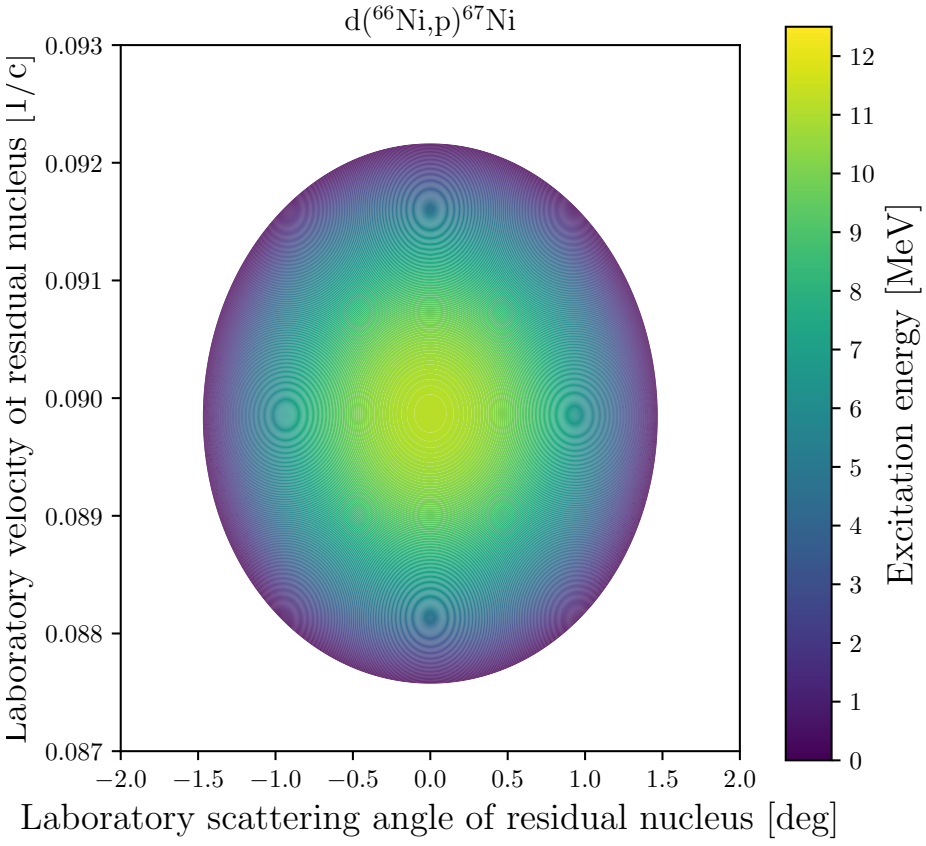

Figure 5.3: Laboratory scattering angle and velocity of residual ^{67}Ni from a d(^{66}Ni, p)^{67}Ni reaction with 295 MeV ^{66}Ni beam.

Although not seen in these experiments, fusion evaporation could still have a significant impact for other beams and needs to be taken into consideration during the planning stages of an experiment.

Chapter 6

Summary and outlook

The Oslo method has received much attention in recent years as the method has matured and proven itself as an effective tool for measuring nuclear level densities and γ-ray strength functions. The method is unique as it is the only technique able to simultaneously determine both quantities from the same dataset. Standard Oslo method experiments use light-ion beams. To reach neutron-rich nuclei, alternative experimental methods have to be employed. One such alternative method is inverse kinematics and in Paper I, the Oslo method was, for the first time, applied to an inverse kinematics experiment performed at iThemba LABS. In Paper III, the method is applied, for the first time, to an inverse kinematics experiment with a radioactive beam performed at Isolde CERN. These papers demonstrate the versatility of the Oslo method and show that level densities and γ-ray strength functions can be reliably extracted from inverse kinematics experiments. Based on the measured NLDs and γSFs of ^{87}Kr and ^{67}Ni, the theoretical estimates for the neutron capture rates and cross sections of ^{86}Kr and ^{66}Ni can be considerably constrained. As discussed in Paper III, the ^{66}Ni(n,γ) cross section can have a significant impact on astrophysical models [6]. The Oslo method with inverse kinematics and the β-Oslo method [12] are valuable tools for constraining neutron capture rates in neutron rich nuclei.

With the new OSCAR array, the Oslo Cyclotron Laboratory now has unique experimental capabilities. The unrivaled resolution, timing capabilities and efficiency of $LaBr_3$:Ce detectors allow for high-precision measurements that open new avenues of research. Complementary techniques such as the Shape method [69, 70], which requires well resolved diagonals, can be applied to data from OSCAR to constrain systematic errors [72].

The new fast-timing array at iThemba LABS, consisting of $LaBr_3$:Ce detectors, provides great energy resolution and timing capabilities. In Paper IV, the detectors are characterized and their energy and timing resolution are presented. With this array, direct measurements of lifetimes as low as 100 picoseconds are possible [62].

Understanding the systematic behaviour of NLDs and γSFs is important when models of these properties are evaluated. Recently, a new IAEA database was created to gather all experimental γSF results [33]. In Paper II, the NLD and γSF of ^{63}Ni is measured and compared with those of other nickel isotopes to look for systematic behaviours. This study shows a clear trend of decreasing γ-strength at energies below 4.5 MeV with increasing mass.

Outlook

To end the thesis, I would like to list a few experiments and future developments that I think would be important.

Results from the commissioning and characterization of the OSCAR array has yet to be published. A paper on these results and its capabilities should be written.

As briefly mentioned in Chapter 2 and Chapter 4, the spin distributions of nuclei are one of the major sources of systematic errors. Within the Oslo method framework, the spin distribution could conceivably be probed. One approach is to look at particle-$\gamma - \gamma$ coincidences gating on Yrast transitions to select different initial spins. Such experiments can be done in Oslo with the OSCAR array.

Another idea to probe the spin distribution would be to use specialized experimental setups such as the K600 spectrometer at iThemba LABS. Measuring γ rays in coincidence with inelastic scattered protons at 0° for an even-even target would ensure the reaction is highly selective, populating mainly 0^+. Assuming the Brink-Axel hypothesis is valid, then the first generation matrix from such an experiment would be proportional to the density of $J = 1$ states, not the total level density.

The Hauser-Feshbach model assumes the Brink-Axel hypothesis. In a recent study by Isaak *et al.* [28] the γ-ray strength function of ^{128}Te is examined using quasi-monochromatic polarized γ rays from the HIγS which populated 1^+ states. The photoabsorption cross section was measured and the strength function from decay was found with the Shape method applied to γ-γ coincidences. The results of this study showed the upwards and downwards strength function differed with as much as a factor 2. Signs of excitation energy dependence for the decay strength was also observed. The Oslo method framework allows for similar studies [25, 26, 72] and Oslo-method-type measurements of the γ-ray strength function should be performed for ^{128}Te.

Both the issue of targets melting and potential background from fusion evaporation can be avoided by using gas-filled targets, albeit with added complexity. Such an experiment has been approved to run at TRIUMF in Canada [73]. In this experiment, a ^{142}Cs beam will impinge on a deuteron gas target coupled to an advanced silicon tracking array to probe the γSF and NLD of ^{143}Cs. Another novel approach is the (p, 2p) knock-out reaction. Such an experiment with a high energy ($\geq$ 200 MeV/A) neutron-rich Indium beam impinging on a liquid hydrogen target has been proposed at RIKEN in Japan [74].

Papers

Paper I

First application of the Oslo method in inverse kinematics

Nuclear level densities and gamma-ray strength functions of 87Kr

V. W. Ingeberg, S. Siem, M. Wiedeking, K. Sieja, D. L. Bleuel, C. P. Brits, T. D. Bucher, T. S. Dinoko, J. L. Easton, A. Görgen, M. Guttormsen, P. Jones, B. V. Kheswa, N. A. Khumalo, A. C. Larsen, E. A. Lawrie, J. J. Lawrie, S. N. T. Majola, K. L. Malatji, L. Makhathini, B. Maqabuka, D. Negi, S. P. Noncolela, P. Papka, E. Sahin, R. Schwengner, G. M. Tveten, F. Zeiser, B. R. Zikhali

Published in *Eur. Phys. J. A*, **56**:68 (2020), DOI: 10.1140/epja/s10050-020-00070-7

Eur. Phys. J. A (2020) 56:68
https://doi.org/10.1140/epja/s10050-020-00070-7

THE EUROPEAN PHYSICAL JOURNAL A

Regular Article - Experimental Physics

First application of the Oslo method in inverse kinematics

Nuclear level densities and γ-ray strength functions of ^{87}Kr

V. W. Ingeberg[1,a], S. Siem[1], M. Wiedeking[2], K. Sieja[3,4], D. L. Bleuel[5], C. P. Brits[2,6], T. D. Bucher[2], T. S. Dinoko[2], J. L. Easton[2,7], A. Görgen[1], M. Guttormsen[1], P. Jones[2], B. V. Kheswa[2,8], N. A. Khumalo[2], A. C. Larsen[1], E. A. Lawrie[2], J. J. Lawrie[2], S. N. T. Majola[2,8,9], K. L. Malatji[2,6], L. Makhathini[2,6], B. Maqabuka[2,7], D. Negi[2], S. P. Noncolela[2,7], P. Papka[2,6], E. Sahin[1], R. Schwengner[10], G. M. Tveten[1], F. Zeiser[1], B. R. Zikhali[2,9]

[1] Department of Physics, University of Oslo, 0316 Oslo, Norway
[2] iThemba LABS, P.O. Box 722, Somerset West 7129, South Africa
[3] Université de Strasbourg, IPHC, 23 rue du Loess, 67037 Strasbourg, France
[4] CNRS, UMR7178, 67037 Strasbourg, France
[5] Lawrence Livermore National Laboratory, 7000 East Avenue, Livermore, CA 94550-9234, USA
[6] Department of Physics, Stellenbosch University, Private Bag X1, Matieland 7602, South Africa
[7] Department of Physics, University of the Western Cape, P/B X17, Bellville 7535, South Africa
[8] Department of Physics, University of Johannesburg, P.O. Box 524, Auckland Park 2006, South Africa
[9] Department of Physics, University of Zululand, Private Bag X1001, KwaDlangezwa 3886, South Africa
[10] Institut für Strahlenphysik, Helmholtz-Zentrum Dresden-Rossendorf, 01328 Dresden, Germany

Received: 12 July 2019 / Accepted: 14 January 2020 / Published online: 20 February 2020

Communicated by Ari Jokinen

Abstract The γ-ray strength function (γSF) and nuclear level density (NLD) have been extracted for the first time from inverse kinematic reactions with the Oslo method. This novel technique allows measurements of these properties across a wide range of previously inaccessible nuclei. Proton–γ coincidence events from the d(^{86}Kr, pγ)^{87}Kr reaction were measured at iThemba LABS and the γSF and NLD in ^{87}Kr was obtained. The low-energy region of the γSF is compared to shell-model calculations, which suggest this region to be dominated by M1 strength. The γSF and NLD are used as input parameters to Hauser–Feshbach calculations to constrain (n, γ) cross sections of nuclei using the TALYS reaction code. These results are compared to ^{86}Kr(n, γ) data from direct measurements.

1 Introduction

The nuclear level density (NLD) and the γ-ray strength function (γSF) are fundamental properties of the nucleus. The NLD was introduced by Bethe soon after the composition of nuclei was firmly established [1]. When excitation energy in a nucleus increases towards the particle separation energy, the NLD increases rapidly, creating a region referred to as the quasi-continuum. The ability of atomic nuclei to emit and absorb photons in the quasi-continuum is determined by the γSF [2]. It is a measure of the average reduced γ-ray decay probability and reveals essential information about the electromagnetic response and therefore the nuclear structure of the nucleus.

With their significant applicability to astrophysical element formation via capture processes [3–6], NLDs and γSFs have received increased experimental and theoretical attention [7]. They are also relevant to the design of existing and future nuclear power reactors, where reactor simulations depend on many evaluated nuclear reactions [8,9]. The importance of NLDs and γSFs is increasingly being recognized and a reference database for γSFs has been established [10]. Nonetheless, challenges remain and nuclear physics properties, such as the NLD and γSF, remain a main source of uncertainty in cross-section calculations. This is either due to the complete lack of experimental data or the associated large experimental uncertainties.

The situation can be improved through accurate experimental neutron capture cross sections, or indirectly by measuring NLD and γSF data. One experimental approach, the Oslo method [11], has been extensively used to measure the NLD and γSF from particle–γ coincident data. NLDs and γSFs obtained with the Oslo method have been shown to provide reliable neutron capture cross sections [12,13] and proton capture cross sections [14]. In recent years, the Oslo

[a] e-mail: vetlewi@fys.uio.no (corresponding author)

method has been extended to extract the γSF and NLD following β decay [15]. Using γSFs and NLDs to determine capture cross sections has several advantages since these properties can be obtained for any nucleus that can be populated in a reaction from which the excitation energy can be experimentally determined. Although the Oslo and β-Oslo methods provide access to a vast range of stable and radioactive nuclei some species remain inaccessible. Many more nuclei become accessible by using inverse kinematic reactions, from radioactive species to several stable isotopes for which the manufacture of targets is problematic due to their chemical or physical properties.

In this Letter we report on the first application to measure the NLD and γSF with the Oslo method following an inverse kinematic reaction. This work lays the foundation of new opportunities to study statistical properties of nuclei, which were previously inaccessible, at stable and radioactive ion beam facilities. The results from the d(^{86}Kr, p)^{87}Kr reaction exhibit a low-energy enhancement of the γSF in ^{87}Kr, which is discussed in the context of shell-model calculations. The ^{86}Kr(n, γ) cross section is obtained from the TALYS reaction code [16] and compared to previous direct measurements to test the robustness of the experimental method.

2 Experiment

The experiment was performed with a 300 MeV ^{86}Kr beam from the Separated Sector Cyclotron facility at iThemba LABS. Polyethylene targets with 99% deuteron enrichment were bombarded with a beam intensity of $\approx$ 0.1 pnA for 80 hrs. Several deuterated polyethylene targets, ranging in thicknesses from 110 to 550 μg/cm^2, were used. Accounting for the target thicknesses the center-of-mass (CM) energy was 6.44(40) MeV. The reactions were identified through the detection of light charged particles in two silicon ΔE–E telescopes covering scattering angles between 24° and 67° relative to the beam direction (corresponding to CM-angles 38°–121°). The E detectors were 1 mm thick while the ΔE detectors were 0.3 and 0.5 mm thick. The dimensions of the W1-type double-sided silicon strip detectors [17] were 4.8 × 4.8 cm and they consisted of 16 parallel and perpendicular strips 3 mm wide with an opening angle of $\approx$ 1.5° for each pixel. Suppression of δ electrons was achieved by an aluminum foil of 4.1 mg/cm^2 areal density which was placed in front of the ΔE detectors. The γ-rays were measured with the AFRODITE array [18], which at the time of the experiment consisted of eight collimated and Compton suppressed high-purity germanium CLOVER-type detectors. Two non-collimated LaBr$_3$:Ce detectors (3.5″ × 8″) were coupled to the AFRODITE array and mounted 24 cm from the target at 45°. The detectors were calibrated using standard ^{152}Eu and ^{56}Co sources. The detector signals were processed by XIA digital electronics in time-stamped list mode with each channel self-triggered.

From the time-stamped list mode data, entries were selected based on their time-stamps being within a window of ±1850 ns in an E-detector entry. The ratio of energy deposited in the ΔE- to the E-detector is used to determine the outgoing reaction channels. The selection of proton–γ events was made with an 80 ns wide time-gate on the prompt time peak. Contributions from uncorrelated events were subtracted from the data by placing off-prompt time gates of equal length. This leads to approximately 100 k proton–γ events in both LaBr$_3$:Ce and CLOVER matrices. In this letter only the data from the LaBr$_3$:Ce detectors are included, although data from the CLOVER detectors yield similar results. Kinematic corrections due to the reaction Q value, recoil energy of ^{87}Kr, and the energy losses of the protons in the target and aluminum foils were applied to determine the excitation energy of the populated states, with the a resulting FWHM for excitation energy of $\approx$ 1 MeV. The γ-rays in coincidence with protons were Doppler corrected by assuming the residual ^{87}Kr nucleus not being deflected from the beam axis and has a constant velocity of 8.5% of c. Due to these assumptions the error in deflection angle is less than 1.3° while the error in velocity is less than 0.4% of c. These errors are negligible as the major contributor to errors in the Doppler correction is the 17° opening angle of the LaBr3:Ce detectors. Background from ^{86}Kr + ^{12}C fusion evaporation events has been simulated with PACE4 [19] and was found to have a very low proton yield ($<$ 4%) with proton energies outside the energy range considered in the analysis. This matrix is unfolded [20] with response functions of the detectors extracted from a Geant4 [21] simulation of the LaBr$_3$:Ce detectors. An iterative subtraction method, known as the first-generation method [22], is applied to the unfolded γ-ray spectra, revealing the distribution of primary γ-rays in each excitation bin (256 keV bin width for both the E_x and E_γ axes).

The NLD $\rho(E_x)$ at excitation energy E_x and γ-ray transmission coefficient, $\mathcal{T}(E_\gamma)$, are related to the primary γ-ray spectrum by [11]

$$P(E_x, E_\gamma) \propto \rho(E_x - E_\gamma)\mathcal{T}(E_\gamma), \tag{1}$$

and are extracted with a χ^2-method [11] giving the unique solution of the functional shape of the NLD and $\mathcal{T}(E_\gamma)$. These are normalized to known experimental data to retrieve the correct slope and absolute value. The extraction has been performed within the limits $3.2 < E_x < 5.2$ MeV and $E_\gamma > 1.7$ MeV of the primary γ-ray matrix where the level density is sufficiently high for statistical decay to be dominant.

3 Normalization

From the primary γ-ray spectrum the NLD $\widetilde{\rho}(E_x)$ and γ-transmission coefficient $\widetilde{\mathcal{T}}(E_\gamma)$ are extracted. These are related to the physical solution by the following transformation [11]:

$$\rho(E_x) = A\widetilde{\rho}(E_x)e^{\alpha E_x} \tag{2}$$

$$\mathcal{T}(E_\gamma) = B\widetilde{\mathcal{T}}(E_\gamma)e^{\alpha E_\gamma}, \tag{3}$$

where A and B are the absolute values for the level density and the transmission coefficient, respectively, and α is the common slope parameter.

For the level density, the slope and absolute value are determined by a fit to the level density found from the known discrete levels [23] at low-excitation energy and the level density at the neutron separation energy ($S_n = 5.5$ MeV). The level density of $J = 1/2$ levels at S_n is determined from the average resonance spacing of s-wave resonances (D_0) and p-wave resonances ($D_1(J = 1/2)$) by

$$\rho(Sn, J = 1/2) = \frac{1}{D_0} + \frac{1}{D_1(J = 1/2)}, \tag{4}$$

with the spacing parameters are taken from [24]. The full level density at S_n is determined by

$$\rho(S_n) = \rho(S_n, J = 1/2)/g(Sn, J = 1/2), \tag{5}$$

where g is the spin distribution [25]

$$g(E, J) = \frac{2J+1}{2\sigma^2(E)} e^{-(J+1/2)^2/2\sigma^2(E)}. \tag{6}$$

The spin cutoff parameter $\sigma(E)$ is modeled with the following energy dependence [12]:

$$\sigma^2(E) = \sigma_d^2 + \frac{E - E_d}{S_n - E_d}(\sigma^2(S_n) - \sigma_d^2), \tag{7}$$

where E_d is the excitation energy below which the spin cutoff parameter $\sigma = \sigma_d$ is a constant. The spin cutoff parameter σ_d at $E_d \leq 2.4$ MeV is estimated to be 1.75(26), based on the spin assignment of the known levels, while the cutoff parameter at the neutron separation energy $\sigma(S_n)$ is estimated to be 3.95(60), based on the predictions of the spin cutoff models of Refs. [26–28]. The shape of the spin distribution predicted by the Hartree–Fock–Bogoliubov plus combinatorial model [29] has also been considered and found to be in agreement. Based on the estimated uncertainties of $\sigma(E)$ and the experimental uncertainties of the resonance spacing, the total NLD at S_n is found to be 1472(427) MeV^{-1}.

The level density extracted with the Oslo method extracted extends up to 3.7 MeV and an interpolation between the Oslo method data and the neutron separation energy has to be done. This interpolation uses the constant temperature (CT) shape [30]

$$\rho_{\mathrm{CT}}(E) = \frac{1}{T} e^{\frac{E-E_0}{T}}, \tag{8}$$

with shift parameter $E_0 = S_n - T\ln(T\rho(S_n))$ to ensure that the interpolation matches the experimental known $\rho(S_n)$. The optimum temperature parameter T in the interpolation, as well as the normalization parameters A and α, are determined through a least-squares fit between the level density extracted in the Oslo method and the discrete levels for energies below $E_x = 2.4$ MeV and the CT interpolation above.

Since the reaction is sub-Coulomb barrier the primary reaction channel will be neutron capture following inelastic deuteron breakup in the Coulomb field of the ^{86}Kr projectile and 1/2 states are assumed to be strongly favored in the initial population, and has to be accounted for. Since the resulting normalized level density found with the Oslo method will correspond to the level density of 1/2 and 3/2 levels, the total level density is recovered by dividing by $g(E_x, 1/2) + g(E_x, 3/2)$.

The same normalization procedure has been repeated, but with an interpolation with a shape matching that of the Back-Shifted Fermi-gas model [27,31] with the difference in the resulting normalization included in the error bars. All errors due to systematical and statistical effects of the Oslo method [32], together with those related to the normalization process have been propagated to give the level density with error bars shown in Fig. 1.

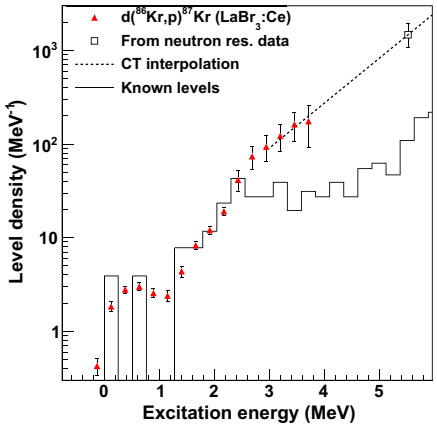

Fig. 1 Normalized ^{87}Kr nuclear level densities for $LaBr_3$:Ce (red circles) detectors. The black line shows the known levels while the open square is the level density at the neutron separation energy. The dashed line is the constant temperature interpolation. The error bars represent the upper and lower uncertainty limit due to all known statistical and systematic effects

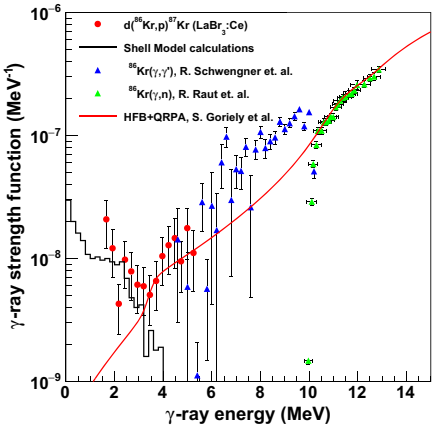

Fig. 2 γ-ray strength function of ^{87}Kr (red circles) compared with the γ-ray strength function of ^{86}Kr extracted from ^{86}Kr(γ, γ') (blue triangles) [35] and ^{86}Kr(γ, n) (green squares) [36]. The solid black line are results from Shell Model calculations with a ^{78}Ni core (see Sect. 5 for details), while the red line is the microscopic HFB+QRPA prediction [37] for the E1 strength. The error bars include all known statistical and systematic errors

Table 1 Experimental values and parameters used in the normalization. The spin cutoff at S_n $\sigma(Sn)$ is an average of the models presented in [26–29] while σ_d is estimated from discrete states with known spin. The level density of 1/2 levels at S_n are found using Eq. (4) and the total level density at S_n with Eq. (5). The temperature T is determined from a least-squares fit to data points in the range $2.4 < E_x < 3.7$ MeV

D_0	26.2(21) keV [24]
D_1 (J = 1/2)	18.8(14) keV [24]
$\sigma(S_n)$	3.95(60)
σ_d	1.75(26)
$\rho(S_n, 1/2)$	91(5) MeV^{-1}
$\rho(S_n)$	1472(427) MeV^{-1}
$\langle\Gamma_{\gamma 0}\rangle$	0.25(10) eV [33]
T	0.9(1) MeV

The absolute value of the transmission coefficients are normalized to the average radiative width of s-wave resonances $\langle\Gamma_{\gamma 0}\rangle$ in a process detailed in [34], and converted to γSF by $f(E_\gamma) = \mathcal{T}(E_\gamma)/(2\pi E_\gamma^3)$. The value of $\langle\Gamma_{\gamma 0}\rangle$ is estimated to be 0.25(10) eV based on the measured Γ_γ of s-wave resonances of [33]. The resulting γSF with all errors propagated are shown in Fig. 2. All experimental values and parameters used in the normalization process are listed in Table 1.

4 Nuclear level densities and γ-ray strength functions

The normalized NLD is shown in Fig. 1 and is in excellent agreement with the constant temperature level density and matches well with the known discrete states at lower excitation energies. The normalized γSF is shown in Fig. 2 and is consistent with γSFs from ^{86}Kr(γ, γ') [35] and ^{86}Kr(γ, n) [36], with the enhancement seen in the (γ, γ') data between 6 and 8 MeV caused by a Pygmy resonance [35]. A drop in the γSFs at $\sim$ 2.1 MeV is caused by the 2123-keV state in ^{87}Kr, which is strongly populated in the reaction, but less through feeding from the quasi-continuum. This causes the first-generation method to over-subtract in the higher excitation-energy bins, causing an artificial drop in the γSF. This effect has previously been discussed [32]. At low energies we observe a large enhancement in the γSF, similar to what has been observed in several other nuclei [38–44]. Although the *upbend* has been independently confirmed [45], little is known of the origin of this feature, except that it is dominated by dipole radiation [46–48] and that it can have large effects on neutron capture cross sections [49].

5 Shell-model calculations

Calculations within the shell-model framework predicts the upbend due to M1 transitions [50]. In this work, large-scale shell-model calculations of the M1 component of the γSF were performed in the model space outside the ^{78}Ni core, containing $f_{5/2}p_{3/2}p_{1/2}g_{9/2}$-proton and $d_{5/2}s_{1/2}$ $d_{3/2}g_{7/2}h_{11/2}$-neutron orbitals. The effective interaction employed here is described e.g. in Refs. [51,52]. The diagonalization of the Hamiltonian matrix in the full configuration space was achieved using the Strasbourg shell-model code NATHAN [53]. The spin part of the magnetic operator was quenched by a common factor of 0.75 [53]. We computed this way up to 60 states of each spin between 1/2 and 15/2 for both parities. This leads to a total of around $8 \cdot 10^4$ M1 matrix elements, among which 14,822 connect states located in the energy range $E_x = 3.4 - 5.4$ MeV, as considered in the experiment. To obtain the average strength per energy interval, $\langle B(M1)\rangle$, the total transition strength was accumulated in 200 keV bins and divided by the number of transitions within these bins. The γSF was obtained from the relation $f_{M1}(E_\gamma, E_i, J_i, \pi) = 16\pi/9(\hbar c)^{-3}\langle B(M1)(E_\gamma, E_i, J_i, \pi)\rangle\rho(E_i, J_i, \pi)$, where $\rho_i(E_i, J_i, \pi)$ is the partial level density at the energy of the initial state (E_i). The γSF, shown in Fig. 2, is an average of the f_{M1}s evaluated for each spin/parity separately. The shape of the shell-model γSF is consistent with experimental data up to $\sim$ 3 MeV. Since the model space does not contain all spin-orbit partners (i.e., $\nu g_{9/2}$ and $\pi f_{7/2}$ orbits) the strength above 4 MeV, due to the spin-flip transitions, cannot be accounted for. However, the theoretical γSF exhibits significant strength at $E_\gamma = 0$, as in the previous shell-model calculations in this mass region [50]. The largest $B(M1)$ contributions at low γ-ray energies in ^{87}Kr

are related to transitions between close-lying negative-parity states with $\nu d_{5/2} \otimes \pi f_{5/2}^{-1} g_{9/2}^{1}$ and $\nu d_{5/2} \otimes \pi p_{3/2}^{-1} g_{9/2}^{1}$ components. The magnitude of the theoretical M1 strength is in good agreement with the data as measured in the experiment; however, we cannot exclude an additional contribution from E1 strength. Recent experimental results in ^{56}Fe [48] could suggest a mixture of M1 and E1 radiation in the enhancement region and the addition of a non-zero E1 component without an upbend towards $E_\gamma \rightarrow 0$ MeV is predicted from shell-model calculations [54]. Including the E1 strength calculations from the Hartree–Fock–Bogolyubov + QRPA (HFB+QRPA) model by [37] we observe an overall good agreement between theoretical predictions and experimental results.

6 Neutron capture cross sections

In a statistical framework the ^{86}Kr(n, γ) cross section can be determined from the NLD, γSF and a suitable neutron optical model potential (nOMP) for ^{87}Kr. Phenomenological nOMPs e.g. from Ref. [55] are observed to give good agreement with the total cross section for nuclei close to the valley of stability. We performed Hauser–Feshbach (HF) [56] calculations with the TALYS[1] code [16], and the optical model potential of Ref. [55]. A semi-microscopic optical model [57] was also tested, and gave virtually the same results. Pre-equilibrium reactions were also taken into account. Tabulated experimental NLD are passed to TALYS, with NLD at energies above 3.7 MeV generated from the CT interpolation. Up to 2.3 MeV the known discrete levels are used. E1 and M1 strength are tabulated from the experimental γSF ($1.6 \leq E_\gamma \leq 5.2$ MeV, 2.1 MeV data point excluded) with the strength outside the experimental region tabulated from the microscopic HFB + QRPA calculations of [37] for the E1 strength and the strength found in the SM calculations plus a standard Lorentzian for the M1 spin flip with the default TALYS parameterization. Decomposition of the experimental γSF are done by subtracting the SM + spin-flip strength and assuming the residual being E1.

The capture cross section for astrophysical relevant neutron energies are proportional to the integrated product of the NLD and γSF at all energies from the ground state to the neutron separation energy and are the region experimentally determined. The resulting neutron capture cross section are shown in Fig. 3. The input parameters have been varied in accordance with the statistical and systematic uncertainties to produce the red-hashed error-band. We observe an overall good agreement with direct measurements by Bhike et al. [58] and a decent agreement at higher energies with measurements of Walter et al. [59], while somewhat high compared

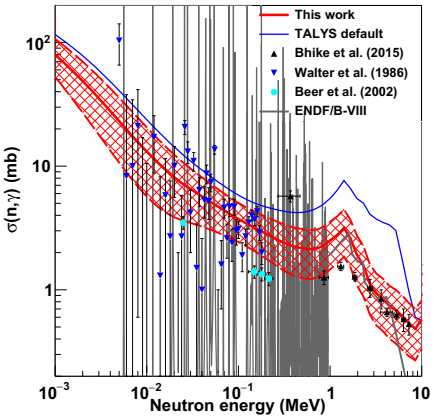

Fig. 3 ^{86}Kr(n, γ) cross sections. The red-hashed area represents the total uncertainty based on both systematical and statistic errors. The gray and blue lines are from the evaluation of ENDF/B-VII.1 [8] and the TALYS default input, respectively, and is provided for comparison. The black triangles shows the direct measurements of Bhike et al. [58], the blue upside-down triangles are results from time-of-flight measurements of Walter et al. [59] and the turquoise circles are the results from the activation measurements of Beer et al. [60]

with the activation results of Beer et al. [60]. The Maxwellian average (MACS) at the typical s-process temperature of 30 keV is found to be 7.2(36) mb, which is higher than the evaluated value of 3.4(3) mb found in KaDoNis [61]. This discrepancy can be explained by the fact that HF calculations will give results that overestimate the MACS for low temperatures when the level density is low [62]. A possible resolution could be to use Monte Carlo simulations to generate statistical resonances from average nuclear properties as proposed in [63,64].

7 Conclusion

We have presented a novel method for obtaining γSF and NLD using inverse kinematic reactions, which opens opportunities to study a wide range of stable and radioactive nuclei. The $d(^{86}\text{Kr}, p\gamma)$ reaction was used to measure the NLD and γSF in ^{87}Kr. The low-energy part of the γSF is found to exhibit an enhancement. Shell-model calculations were performed and suggest that the enhancement is predominantly due to low-energy M1 transitions in ^{87}Kr.

The γSF and NLD measurements in ^{87}Kr were used to calculate (n, γ) cross sections, which are in good agreement with those from direct measurements, and give confidence in the approach using inverse kinematic reactions. This is consistent with the findings of previous work with the Oslo method and is particularly interesting since direct measure-

[1] Version 1.9.

ment of neutron capture cross sections over a wide range of incident neutron energies is very challenging. It is clear that γSFs and NLDs provide a viable alternative to obtain reliable capture cross sections.

With inverse kinematics, new regions of the nuclear chart become accessible to experiments, which also brings about new challenges. For exotic nuclei, neutron resonance data are not known and the normalizing procedure needs to be revised. One possibility is that the slope of the γSF, and thereby also the slope of the NLD, could be constrained using a technique where the ratio of populated discrete states from the quasi-continuum is used to determine the shape of the γSF [45,65], leaving the absolute value of the NLD to be determined by the known discrete levels. Unfortunately, this still does not determine the absolute value of the γSF. However, reasonable estimates of the absolute value may be obtained from systematics of the $\langle\Gamma_{\gamma 0}\rangle$.

Measuring statistical properties of nuclei from inverse kinematic reactions provides a novel and complementary foundation for exploring the limitations of the current models of statistical behavior in the nucleus. It will allow for further constraining the uncertainties in models which are used in nuclear astrophysics and reactor physics.

Acknowledgements Open Access funding provided by the University of Oslo & Oslo University Hospital. The authors would like to thank iThemba LABS operations for stable running conditions and John Greene (Argonne National Lab.) for providing excellent targets. This work is based on research supported by the Research Council of Norway under project Grants no. 222287, 262952 (G. M. T.), 263030 (V. W. I, S. S., A. G., F. Z.) and 240104 (E.S), by the National Research Foundation of South Africa under grant no 118846, and the U.S. Department of Energy by Lawrence Livermore National Laboratory under Contract DE-AC52-07NA27344. A. C. L. gratefully acknowledges funding through ERC-STG-2014 Grant Agreement no. 637686, and support from the ChETEC Cost Action (CA16117) supported by COST. This work was performed within the IAEA CRP on "Updating the Photonuclear data Library and generating a Reference Database for Photon Strength Functions" (F410 32). M. W. and S. S. acknowledge the support from the IAEA under Research Contract 20454 and 20447, respectively.

Data Availability Statement This manuscript has associated data in a data repository. [Author's comment: The NLD and γSF are available online at http://mn.uio.no/fysikk/english/research/about/infrastructure/ocl/nuclear-physics-research/compilation/ and has been deposited to the IAEA PSF database [10] (http://www-nds.iaea.org/PSFdatabase/). Raw data will be made available upon request.]

References

1. H.A. Bethe, An attempt to calculate the number of energy levels of a heavy nucleus. Phys. Rev. **50**, 332–341 (1936). https://doi.org/10.1103/PhysRev.50.332. https://link.aps.org/doi/10.1103/PhysRev.50.332
2. G.A. Bartholomew, E.D. Earle, A.J. Ferguson, J.W. Knowles, M.A. Lone, Gamma-Ray Strength Functions, pages 229–324. Springer US, Boston, MA, (1973). ISBN 978-1-4615-9044-6. https://doi.org/10.1007/978-1-4615-9044-6_4
3. T. Rauscher, N. Dauphas, I. Dillmann, C. Fröhlich, Z. Fülöp, G. Gyürky, Constraining the astrophysical origin of the p-nuclei through nuclear physics and meteoritic data. Rep. Prog. Phys., **76**(6), 066201, (2013). http://stacks.iop.org/0034-4885/76/i=6/a=066201
4. M. Arnould, S. Goriely, The p-process of stellar nucleosynthesis: astrophysics and nuclear physics status. Phys. Rep., **384**(1), 1–84, (2003). ISSN 0370-1573. https://doi.org/10.1016/S0370-1573(03)00242-4. http://www.sciencedirect.com/science/article/pii/S0370157303002424
5. M. Arnould, S. Goriely, K. Takahashi, The r-process of stellar nucleosynthesis: astrophysics and nuclear physics achievements and mysteries. Phys. Rep., **450**(4), 97–213, (2007). ISSN 0370-1573. https://doi.org/10.1016/j.physrep.2007.06.002. http://www.sciencedirect.com/science/article/pii/S0370157307002438
6. S. Goriely, Radiative neutron captures by neutron-rich nuclei and the r-process nucleosynthesis. Phys. Lett. B, **436**(1), 10–18, (1998). ISSN 0370-2693. https://doi.org/10.1016/S0370-2693(98)00907-1. http://www.sciencedirect.com/science/article/pii/S0370269398009071
7. A.C. Larsen, A. Spyrou, S.N. Liddick, M. Guttormsen, Novel techniques for constraining neutron-capture rates relevant for r-process heavy-element nucleosynthesis, (2019). ISSN 01466410. https://www.sciencedirect.com/science/article/pii/S0146641019300298
8. M.B. Chadwick, M. Herman, P. Obložinský, M.E. Dunn, Y. Danon, A.C. Kahler, D.L. Smith, B. Pritychenko, G. Arbanas, R. Arcilla, R. Brewer, D.A. Brown, R. Capote, A.D. Carlson, Y.S. Cho, H. Derrien, K. Guber, G.M. Hale, S. Hoblit, S. Holloway, T.D. Johnson, T. Kawano, B.C. Kiedrowski, H. Kim, S. Kunieda, N.M. Larson, L. Leal, J.P. Lestone, R.C. Little, E.A. McCutchan, R.E. MacFarlane, M. MacInnes, C.M. Mattoon, R.D. McKnight, S.F. Mughabghab, G.P.A. Nobre, G. Palmiotti, A. Palumbo, M.T. Pigni, V.G. Pronyaev, R.O. Sayer, A.A. Sonzogni, N.C. Summers, P. Talou, I.J. Thompson, A. Trkov, R.L. Vogt, S.C. van der Marck, A. Wallner, M.C. White, D. Wiarda, P.G. Young, Endf/b-vii.1 nuclear data for science and technology: cross sections, covariances, fission product yields and decay data. Nucl. Data Sheets, **112**(12), 2887–2996, (2011). ISSN 0090-3752. https://doi.org/10.1016/j.nds.2011.11.002. http://www.sciencedirect.com/science/article/pii/S009037521100113X. Special Issue on ENDF/B-VII.1 Library
9. M.B. Chadwick, Report of the nuclear physics and related computational science R&D for advanced fuel cycles workshop, (August 2006)
10. S. Goriely, P. Dimitriou, M. Wiedeking, T. Belgya, R. Firestone, J. Kopecky, M. Krtička, V. Plujko, R. Schwengner, S. Siem, H. Utsunomiya, S. Hilaire, S. Péru, Y.S. Cho, D.M. Filipescu, N. Iwamoto, T. Kawano, V. Varlamov, R. Xu, Reference database for photon strength functions. Eur. Phys. J. A **55**(10), 172 (2019). https://doi.org/10.1140/epja/i2019-12840-1

11. A. Schiller, L. Bergholt, M. Guttormsen, E. Melby, J. Rekstad, S. Siem, Extraction of level density and γ strength function from primary γ spectra. Nucl. Instrum. Methods Phys. Res. Sect. A, **447**(3), 498–511 (2000). https://doi.org/10.1016/S0168-9002(99)01187-0
12. M. Guttormsen, S. Goriely, A.C. Larsen, A. Görgen, T.W. Hagen, T. Renstrøm, S. Siem, N.U.H. Syed, G. Tagliente, H.K. Toft, H. Utsunomiya, A.V. Voinov, K. Wikan, Quasi-continuum γ decay of ^{91,92}**Zr**: Benchmarking indirect (n, γ) cross section measurements for the s process. Phys. Rev. C **96**, 024313 (2017). https://doi.org/10.1103/PhysRevC.96.024313. https://link.aps.org/doi/10.1103/PhysRevC.96.024313
13. B.V. Kheswa, M. Wiedeking, J.A. Brown, A.C. Larsen, S. Goriely, M. Guttormsen, F.L. Bello Garrote, L.A. Bernstein, D.L. Bleuel, T.K. Eriksen, F. Giacoppo, A. Görgen, B.L. Goldblum, T.W. Hagen, P.E. Koehler, M. Klintefjord, K.L. Malatji, J.E. Midtbø, H.T. Nyhus, P. Papka, T. Renstrøm, S.J. Rose, E. Sahin, S. Siem, T.G. Tornyi, ^{137,138,139}**La**(n, γ). Phys. Rev. C, **95**, 045805, (2017). https://doi.org/10.1103/PhysRevC.95.045805. https://link.aps.org/doi/10.1103/PhysRevC.95.045805
14. A.C. Larsen, M. Guttormsen, R. Schwengner, D.L. Bleuel, S. Goriely, S. Harissopulos, F.L. Bello Garrote, Y. Byun, T.K. Eriksen, F. Giacoppo, A. Görgen, T.W. Hagen, M. Klintefjord, T. Renstrøm, S.J. Rose, E. Sahin, S. Siem, T.G. Tornyi, G.M. Tveten, A.V. Voinov, M. Wiedeking, Experimentally constrained $(p, \gamma)^{89}$Y and $(n, \gamma)^{89}$Y reaction rates relevant to p-process nucleosynthesis. Phys. Rev. C, **93**, 045810, (2016). https://doi.org/10.1103/PhysRevC.93.045810
15. A. Spyrou, S.N. Liddick, A.C. Larsen, M. Guttormsen, K. Cooper, A.C. Dombos, D.J. Morrissey, F. Naqvi, G. Perdikakis, S.J. Quinn, T. Renstrøm, J.A. Rodriguez, A. Simon, C.S. Sumithrarachchi, R.G.T. Zegers, Novel technique for constraining r-process (n, γ) reaction rates. Phys. Rev. Lett. **113**, 232502 (2014). https://doi.org/10.1103/PhysRevLett.113.232502
16. A.J. Koning, S. Hilaire, M.C. Duijvestijn, Talys-1.0, in *International Conference on Nuclear Data for Science and Technology 2007*, pages 2–5, Les Ulis, France, may 2008. EDP Sciences. https://doi.org/10.1051/ndata:07767
17. Micron Semiconductor Ltd. Product cataloque. Technical report, Micron Semiconductor Ltd., (2017). http://micronsemiconductor.co.uk/wp-content/uploads/2017/01/cat.pdf
18. M. Lipoglavšek, A. Likar, M. Vencelj, T. Vidmar, R.A. Bark, E. Gueorguieva, F. Komati, J.J. Lawrie, S.M. Maliage, S.M. Mullins, S.H.T. Murray, T.M. Ramashidzha, Measuring high-energy γ-rays with Ge clover detectors. Nucl. Instrum. Methods Phys. Res. Sect. A Acceler. Spectrom. Detect. Assoc. Equipment, **557**(2), 523–527, (2006). ISSN 0168-9002. https://doi.org/10.1016/j.nima.2005.11.067. http://www.sciencedirect.com/science/article/pii/S0168900205021935
19. O.B. Tarasov, D. Bazin, LISE++: Radioactive beam production with in-flight separators. Nucl. Instrum. Methods Phys. Res. Sect. B Beam Interact. Mater. Atoms, **266**(19–20), 4657–4664, (2008). ISSN 0168583X. https://doi.org/10.1016/j.nimb.2008.05.110. http://lise.nscl.msu.edu
20. M. Guttormsen, T.S. Tveter, L. Bergholt, F. Ingebretsen, J. Rekstad, The unfolding of continuum γ-ray spectra. Nucl. Instrum. Methods Phys. Res. Sect. A **374**(3), 371–376 (1996). https://doi.org/10.1016/0168-9002(96)00197-0. ISSN 01689002
21. S. Agostinelli, J. Allison, K. Amako, J. Apostolakis, H. Araujo, P. Arce, M. Asai, D. Axen, S. Banerjee, G. Barrand, F. Behner, L. Bellagamba, J. Boudreau, L. Broglia, A. Brunengo, H. Burkhardt, S. Chauvie, J. Chuma, R. Chytracek, G. Cooperman, G. Cosmo, P. Degtyarenko, A. Dell'Acqua, G. Depaola, D. Dietrich, R. Enami, A. Feliciello, C. Ferguson, H. Fesefeldt, G. Folger, F. Foppiano, A. Forti, S. Garelli, S. Giani, R. Giannitrapani, D. Gibin, J.J. Gómez Cadenas, I. González, G. Gracia Abril, G. Greeniaus, W. Greiner, V. Grichine, A. Grossheim, S. Guatelli, P. Gumplinger, R. Hamatsu, K. Hashimoto, H. Hasui, A. Heikkinen, A. Howard, V. Ivanchenko, A. Johnson, F.W. Jones, J. Kallenbach, N. Kanaya, M. Kawabata, Y. Kawabata, M. Kawaguti, S. Kelner, P. Kent, A. Kimura, T. Kodama, R. Kokoulin, M. Kossov, H. Kurashige, E. Lamanna, T. Lampén, V. Lara, V. Lefebure, F. Lei, M. Liendl, W. Lockman, F. Longo, S. Magni, M. Maire, E. Medernach, K. Minamimoto, P. Mora de Freitas, Y. Morita, K. Murakami, M. Nagamatu, R. Nartallo, P. Nieminen, T. Nishimura, K. Ohtsubo, M. Okamura, S. O'Neale, Y. Oohata, K. Paech, J. Perl, A. Pfeiffer, M.G. Pia, F. Ranjard, A. Rybin, S. Sadilov, E. Di Salvo, G. Santin, T. Sasaki, N. Savvas, Y. Sawada, S. Scherer, S. Sei, V. Sirotenko, D. Smith, N. Starkov, H. Stoecker, J. Sulkimo, M. Takahata, S. Tanaka, E. Tcherniaev, E. Safai Tehrani, M. Tropeano, P. Truscott, H. Uno, L. Urban, P. Urban, M. Verderi, A. Walkden, W. Wander, H. Weber, J.P. Wellisch, T. Wenaus, D.C. Williams, D. Wright, T. Yamada, H. Yoshida, D. Zschiesche, Geant4—a simulation toolkit. Nucl. Instrum. Methods Phys. Res. Sect. A Acceler. Spectrom. Detect. Assoc. Equipment, **506**(3), 250–303, (2003). ISSN 0168-9002. https://doi.org/10.1016/S0168-9002(03)01368-8. http://www.sciencedirect.com/science/article/pii/S0168900203013688
22. M. Guttormsen, T. Ramsøy, J. Rekstad, The first generation of γ-rays from hot nuclei. Nucl. Instum. Methods Phys. Res. Sect. A **255**(3), 518–523 (1987). https://doi.org/10.1016/0168-9002(87)91221-6. ISSN 01689002
23. T.D. Johnson, W.D. Kulp, Nuclear data sheets for a = 87. Nucl. Data Sheets, 129:1–190, (2015). ISSN 0090-3752. https://doi.org/10.1016/j.nds.2015.09.001. http://www.sciencedirect.com/science/article/pii/S0090375215000460
24. R.F. Carlton, R.R. Winters, C.H. Johnson, N.W. Hill, J.A. Harvey, Total cross section and resonance spectroscopy for n+^{86}kr. Phys. Rev. C **38**, 1605–1618 (1988). https://doi.org/10.1103/PhysRevC.38.1605
25. T. Ericson, V. Strutinski, On angular distributions in compound nucleus processes. Nucl. Phys. C, **8**, 284–293, (1958). ISSN 00295582. https://doi.org/10.1016/0029-5582(58)90156-1. https://www.sciencedirect.com/science/article/pii/0029558258901561
26. T. von Egidy, D. Bucurescu, Systematics of nuclear level density parameters. Phys. Rev. C **72**, 044311 (2005). https://doi.org/10.1103/PhysRevC.72.044311
27. A. Glibert, A.G.W. Cameron, A composite nuclear-level density formula with shell corrections. Can. J. Phys. **43**, 1446–1496 (1965). https://doi.org/10.1139/p65-139
28. T. von Egidy, D. Bucurescu, Experimental energy-dependent nuclear spin distributions. Phys. Rev. C **80**, 054310 (2009). https://doi.org/10.1103/PhysRevC.80.054310
29. S. Goriely, S. Hilaire, A.J. Koning, Improved microscopic nuclear level densities within the Hartree–Fock–Bogoliubov plus combinatorial method. Phys. Rev. C **78**, 064307 (2008). https://doi.org/10.1103/PhysRevC.78.064307
30. T. Ericson, The statistical model and nuclear level densities. Adv. Phys. **9**(36), 425–511 (1960). https://doi.org/10.1080/00018736000101239
31. E. Erba, U. Facchini, E.S. Menichella, Statistical emission in nuclear reactions and nuclear level density. Il Nuovo Cimento **22**(6), 1237–1260 (1961). https://doi.org/10.1007/BF02786895
32. A.C. Larsen, M. Guttormsen, M. Krtička, E. Běták, A. Bürger, A. Görgen, H.T. Nyhus, J. Rekstad, A. Schiller, S. Siem, H.K. Toft, G.M. Tveten, A.V. Voinov, K. Wikan, Analysis of possible systematic errors in the oslo method. Phys. Rev. C **83**, 034315 (2011). https://doi.org/10.1103/PhysRevC.83.034315
33. S. Raman, B. Fogelberg, J.A. Harvey, R.L. Macklin, P.H. Stelson, A. Schröder, K.L. Kratz, Overlapping β decay and resonance

neutron spectroscopy of levels in ^{87}Kr. Phys. Rev. C **28**, 602–622 (1983). https://doi.org/10.1103/PhysRevC.28.602
34. A. Voinov, M. Guttormsen, E. Melby, J. Rekstad, A. Schiller, S. Siem, γ. Phys. Rev. C **63**, 044313 (2001). https://doi.org/10.1103/PhysRevC.63.044313
35. R. Schwengner, R. Massarczyk, G. Rusev, N. Tsoneva, D. Bemmerer, R. Beyer, R. Hannaske, A.R. Junghans, J.H. Kelley, E. Kwan, H. Lenske, M. Marta, R. Raut, K.D. Schilling, A. Tonchev, W. Tornow, A. Wagner, Pygmy dipole strength in ^{86}kr and systematics of $n = 50$ isotones. Phys. Rev. C **87**, 024306 (2013a). https://doi.org/10.1103/PhysRevC.87.024306
36. R. Raut, A.P. Tonchev, G. Rusev, W. Tornow, C. Iliadis, M. Lugaro, J. Buntain, S. Goriely, J.H. Kelley, R. Schwengner, A. Banu, N. Tsoneva, Cross-section measurements of the ^{86}Kr(γ, n) reaction to probe the s-process branching at ^{85}Kr. Phys. Rev. Lett. **111**, 112501 (2013). https://doi.org/10.1103/PhysRevLett.111.112501
37. S. Goriely, E. Khan, M. Samyn, Microscopic HFB + GRPA predictions of dipole strength for astrophysics applications. Nucl. Phys. A, **739**(3), 331–352, (2004). ISSN 0375-9474. https://doi.org/10.1016/j.nuclphysa.2004.04.105. http://www.sciencedirect.com/science/article/pii/S0375947404006578
38. T. Renstrøm, H.-T. Nyhus, H. Utsunomiya, R. Schwengner, S. Goriely, A.C. Larsen, D.M. Filipescu, I. Gheorghe, L.A. Bernstein, D.L. Bleuel, T. Glodariu, A. Görgen, M. Guttormsen, T.W. Hagen, B.V. Kheswa, Y.-W. Lui, D. Negi, I.E. Ruud, T. Shima, S. Siem, K. Takahisa, O. Tesileanu, T.G. Tornyi, G.M. Tveten, M. Wiedeking, Low-energy enhancement in the γ-ray strength functions of ^{73,74}Ge. Phys. Rev. C **93**, 064302 (2016). https://doi.org/10.1103/PhysRevC.93.064302
39. M. Guttormsen, R. Chankova, U. Agvaanluvsan, E. Algin, L.A. Bernstein, F. Ingebretsen, T. Lönnroth, S. Messelt, G.E. Mitchell, J. Rekstad, A. Schiller, S. Siem, A.C. Sunde, A. Voinov, S. Ødegård, Radiative strength functions in $^{93-98}$Mo. Phys. Rev. C **71**, 044307 (2005). https://doi.org/10.1103/PhysRevC.71.044307
40. A.C. Larsen, R. Chankova, M. Guttormsen, F. Ingebretsen, S. Messelt, J. Rekstad, S. Siem, N.U.H. Syed, S.W. Ødegård, T. Lönnroth, A. Schiller, A. Voinov, Microcanonical entropies and radiative strength functions of ^{50,51}V. Phys. Rev. C **73**, 064301 (2006). https://doi.org/10.1103/PhysRevC.73.064301
41. N.U.H. Syed, A.C. Larsen, A. Bürger, M. Guttormsen, S. Harissopulos, M. Kmiecik, T. Konstantinopoulos, M. Krtička, A. Lagoyannis, T. Lönnroth, K. Mazurek, M. Norby, H.T. Nyhus, G. Perdikakis, S. Siem, A. Spyrou, Extraction of thermal and electromagnetic properties in ^{45}Ti. Phys. Rev. C **80**, 044309 (2009). https://doi.org/10.1103/PhysRevC.80.044309
42. A.C. Larsen, I.E. Ruud, A. Bürger, S. Goriely, M. Guttormsen, A. Görgen, T.W. Hagen, S. Harissopulos, H.T. Nyhus, T. Renstrøm, A. Schiller, S. Siem, G.M. Tveten, A. Voinov, M. Wiedeking, Transitional γ strength in cd isotopes. Phys. Rev. C **87**, 014319 (2013a). https://doi.org/10.1103/PhysRevC.87.014319
43. A. Simon, M. Guttormsen, A.C. Larsen, C.W. Beausang, P. Humby, J.T. Burke, R.J. Casperson, R.O. Hughes, T.J. Ross, J.M. Allmond, R. Chyzh, M. Dag, J. Koglin, E. McCleskey, M. McCleskey, S. Ota, A. Saastamoinen, First observation of low-energy γ-ray enhancement in the rare-earth region. Phys. Rev. C **93**, 034303 (2016). https://doi.org/10.1103/PhysRevC.93.034303
44. B.V. Kheswa, M. Wiedeking, F. Giacoppo, S. Goriely, M. Guttormsen, A.C. Larsen, F.L. Bello Garrote, T.K. Eriksen, A. Görgen, T.W. Hagen, P.E. Koehler, M. Klintefjord, H.T. Nyhus, P. Papka, T. Renstrøm, S. Rose, E. Sahin, S. Siem, T. Tornyi, Galactic production of ^{138}La: Impact of ^{138,139}La statistical properties. Phys. Lett. B, **744**, 268–272, (2015). ISSN 0370-2693. https://doi.org/10.1016/j.physletb.2015.03.065. http://www.sciencedirect.com/science/article/pii/S0370269315002403
45. M. Wiedeking, L.A. Bernstein, M. Krtička, D.L. Bleuel, J.M. Allmond, M.S. Basunia, J.T. Burke, P. Fallon, R.B. Firestone, B.L. Goldblum, R. Hatarik, P.T. Lake, I.-Y. Lee, S.R. Lesher, S. Paschalis, M. Petri, L. Phair, N.D. Scielzo, Low-energy enhancement in the photon strength of ^{95}Mo. Phys. Rev. Lett. **108**, 162503 (2012). https://doi.org/10.1103/PhysRevLett.108.162503
46. A.C. Larsen, N. Blasi, A. Bracco, F. Camera, T.K. Eriksen, A. Görgen, M. Guttormsen, T.W. Hagen, S. Leoni, B. Million, H.T. Nyhus, T. Renstrøm, S.J. Rose, I.E. Ruud, S. Siem, T. Tornyi, G.M. Tveten, A.V. Voinov, M. Wiedeking, Evidence for the dipole nature of the low-energy γ enhancement in ^{56}Fe. Phys. Rev. Lett. **111**, 242504 (2013b). https://doi.org/10.1103/PhysRevLett.111.242504
47. A.C. Larsen, M. Guttormsen, N. Blasi, A. Bracco, F. Camera, L. Crespo Campo, T.K. Eriksen, A. Görgen, T.W. Hagen, V.W. Ingeberg, B.V. Kheswa, S. Leoni, J.E. Midtbø, B. Million, H.T. Nyhus, T. Renstrøm, S.J. Rose, I.E. Ruud, S. Siem, T.G. Tornyi, G.M. Tveten, A.V. Voinov, M. Wiedeking, F. Zeiser, Low-energy enhancement and fluctuations of γ-ray strength functions in 56,57 fe: test of the brink–axel hypothesis. J. Phys. G Nucl. Part. Phys., **44**(6), 064005, (2017). http://stacks.iop.org/0954-3899/44/i=6/a=064005
48. M.D. Jones, A.O. Macchiavelli, M. Wiedeking, L.A. Bernstein, H.L. Crawford, C.M. Campbell, R.M. Clark, M. Cromaz, P. Fallon, I.Y. Lee, M. Salathe, A. Wiens, A.D. Ayangeakaa, D.L. Bleuel, S. Bottoni, M.P. Carpenter, H.M. Davids, J. Elson, A. Görgen, M. Guttormsen, R.V.F. Janssens, J.E. Kinnison, L. Kirsch, A.C. Larsen, T. Lauritsen, W. Reviol, D.G. Sarantites, S. Siem, A.V. Voinov, S. Zhu, Examination of the low-energy enhancement of the γ-ray strength function of ^{56}Fe. Phys. Rev. C **97**, 024327 (2018). https://doi.org/10.1103/PhysRevC.97.024327
49. A.C. Larsen, S. Goriely, Impact of a low-energy enhancement in the γ-ray strength function on the neutron-capture cross section. Phys. Rev. C **82**, 014318 (2010). https://doi.org/10.1103/PhysRevC.82.014318
50. R. Schwengner, S. Frauendorf, A.C. Larsen, Low-energy enhancement of magnetic dipole radiation. Phys. Rev. Lett. **111**, 232504 (2013b). https://doi.org/10.1103/PhysRevLett.111.232504
51. M. Czerwiński, T. Rząca-Urban, W. Urban, P. Bączyk, K. Sieja, B.M. Nyakó, J. Timár, I. Kuti, T.G. Tornyi, L. Atanasova, A. Blanc, M. Jentschel, P. Mutti, U. Köster, T. Soldner, G. de France, G.S. Simpson, C.A. Ur, Neutron–proton multiplets in the nucleus ^{88}Br. Phys. Rev. C **92**, 014328 (2015). https://doi.org/10.1103/PhysRevC.92.014328
52. J. Litzinger, A. Blazhev, A. Dewald, F. Didierjean, G. Duchêne, C. Fransen, R. Lozeva, K. Sieja, D. Verney, G. de Angelis, D. Bazzacco, B. Birkenbach, S. Bottoni, A. Bracco, T. Braunroth, B. Cederwall, L. Corradi, F .C .L. Crespi, P. Désesquelles, J. Eberth, E. Ellinger, E. Farnea, E. Fioretto, R. Gernhäuser, A. Goasduff, A. Görgen, A. Gottardo, J. Grebosz, M. Hackstein, H. Hess, F. Ibrahim, J. Jolie, A. Jungclaus, K. Kolos, W. Korten, S. Leoni, S. Lunardi, A. Maj, R. Menegazzo, D. Mengoni, C. Michelagnoli, T. Mijatovic, B. Million, O. Möller, V. Modamio, G. Montagnoli, D. Montanari, A .I. Morales, D .R. Napoli, M. Niikura, G. Pollarolo, A. Pullia, B. Quintana, F. Recchia, P. Reiter, D. Rosso, E. Sahin, M .D. Salsac, F. Scarlassara, P.-A. Söderström, A .M. Stefanini, O. Stezowski, S. Szilner, Ch. Theisen, J .J. Valiente Dobón, V. Vandone, A. Vogt, Transition probabilities in neutron-rich ^{84,86}Se. Phys. Rev. C **92**, 064322 (2015). https://doi.org/10.1103/PhysRevC.92.064322
53. E. Caurier, G. Martínez-Pinedo, F. Nowacki, A. Poves, A.P. Zuker, The shell model as a unified view of nuclear structure. Rev. Mod. Phys. **77**, 427–488 (2005). https://doi.org/10.1103/RevModPhys.77.427
54. K. Sieja, Electric and magnetic dipole strength at low energy. Phys. Rev. Lett. **119**, 052502 (2017). https://doi.org/10.1103/PhysRevLett.119.052502
55. A.J. Koning, J.P. Delaroche, Local and global nucleon optical models from 1 kev to 200 mev. Nucl. Phys. A, **713**(3),

231–310, (2003). ISSN 0375-9474. https://doi.org/10.1016/S0375-9474(02)01321-0. http://www.sciencedirect.com/science/article/pii/S0375947402013210
56. W. Hauser, H. Feshbach, The inelastic scattering of neutrons. Phys. Rev. **87**, 366–373 (1952). https://doi.org/10.1103/PhysRev.87.366
57. E. Bauge, J.P. Delaroche, M. Girod, Lane-consistent, semimicroscopic nucleon–nucleus optical model. Phys. Rev. C **63**, 024607 (2001). https://doi.org/10.1103/PhysRevC.63.024607
58. M. Bhike, E. Rubino, M.E. Gooden, Krishichayan, W. Tornow, Measurements of the ^{86}Kr$(n,\gamma)^{87}$Kr and ^{86}Kr$(n,2n)^{85}$Kr^{m} reaction cross sections below $E_n = 15$ mev. Phys. Rev. C **92**, 014624 (2015). https://doi.org/10.1103/PhysRevC.92.014624
59. G. Walter, B. Leugers, F. Käppeler, Z.Y. Bao, G. Reffo, F. Fabbri, Kilo-electron-volt neutron capture cross sections of the krypton isotopes. Nucl. Sci. Eng. **93**, 357–369 (1986). https://doi.org/10.13182/NSE86-A18471
60. H. Beer, P.V. Sedyshev, W. Rochow, P. Mohr, H. Oberhummer, Neutron capture measurements of the noble gas isotopes22Ne, 40Ar and 78,80,84,86Kr in the keV energy region. Nucl. Phys. A, **705**(1–2), 239–261, (2002). ISSN 03759474. https://doi.org/10.1016/S0375-9474(02)00645-0. https://www.sciencedirect.com/science/article/abs/pii/S0375947402006450
61. I. Dillmann, Kadonis—the karlsruhe astrophysical database of nucleosynthesis in stars. In: AIP conference proceedings (2006). https://doi.org/10.1063/1.2187846. http://www.kadonis.org
62. T. Rauscher, F.K. Thielemann, K.L. Kratz, Nuclear level density and the determination of thermonuclear rates for astrophysics. Phys. Rev. C Nucl. Phys. **56**(3), 1613–1625 (1997). https://doi.org/10.1103/PhysRevC.56.1613. ISSN 1089490X
63. D. Rochman, A.J. Koning, J. Kopecky, J.C. Sublet, P. Ribon, M. Moxon, From average parameters to statistical resolved resonances. Ann. Nucl. Energy, **51**, 60–68, (2013). ISSN 03064549. https://doi.org/10.1016/j.anucene.2012.08.015. https://www.sciencedirect.com/science/article/pii/S0306454912003350
64. D. Rochman, S. Goriely, A.J. Koning, H. Ferroukhi, Radiative neutron capture: Hauser Feshbach vs. statistical resonances. Phys. Lett. B **764**, 109–113 (2017). https://doi.org/10.1016/j.physletb.2016.11.018
65. M. Krtička, M. Wiedeking, F. Bečvář, S. Valenta, Consistency of photon strength function models with data from the ^{94}Mo(d, p$\gamma\gamma$) reaction. Phys. Rev. C **93**, 054311 (2016). https://doi.org/10.1103/PhysRevC.93.054311

Paper II

Nuclear Level density and Gamma-ray Strength Function of Ni-63

V. W. Ingeberg, P. Jones, L. Msebi, S. Siem, M. Wiedeking, A. A. Avaa, T. D. Bucher, C. P. Brits, M. V. Chisapi, E. A. Lawrie, K. L. Malatji, B. Maqabuka, L. Makhathini, S. P.Noncolela, J. Ndayishmye, A. Netshiya, O. Shinda, B. R. Zikhali

Manuscript in preparation

II

Nuclear Level Density and γ-ray Strength Function of ^{63}Ni

V. W. Ingeberg,[1] P. Jones,[2] L. Msebi,[2,3] S. Siem,[1] M. Wiedeking,[2,4] A. A. Avaa,[2,3] T. D. Bucher,[2] C. P. Brits,[2,5] M. V. Chisapi,[3,5] E. A. Lawrie,[2] K. L. Malatji,[2,5] B. Maqabuka,[2,3] L. Makhathini,[2] S. P. Noncolela,[2,3] J. Ndayishimye,[2] A. Netshiya,[2,4] O. Shirinda,[6] and B. R. Zikhali[2,3]

[1]*Department of Physics, University of Oslo, N-0316 Oslo, Norway*
[2]*Department of Subatomic Physics, iThemba LABS, P.O. Box 722, 7129 Somerset West, South Africa*
[3]*Physics Department, University of the Western Cape, P/B X17, Bellville, 7535, South Africa*
[4]*School of Physics, University of the Witwatersrand, 2050 Johannesburg, South Africa*
[5]*Physics Department, Stellenbosch University, P/B X1, Matieland, 7602, South Africa*
[6]*Department of Physical and Earth Sciences, Sol Plaatje University, Private Bag X5008, Kimberley 8301, South Africa*

(Dated: February 21, 2022)

The nuclear level density (NLD) and γ-ray strength function (γSF) of ^{63}Ni have been investigated using the Oslo method. The NLD was found to agree with previous measurements using particle evaporation [1], but is far lower than that measured in neutron resonance experiments [2–4]. The γSF was found to feature a strong low energy enhancement that could be explained as M1 based on large scale shell model calculations [5]. We compare with NLD and γSF of other Ni isotopes to look for systematic behaviours.

I. INTRODUCTION

The Oslo method is a powerful analytical method that allows for simultaneous extraction of nuclear level density (NLD) and γ-ray strength functions (γSF) from particle-γ coincidences following reactions with light ion beams (e.g. (p,p'), (d,p) etc.) [6]. The method has been extended to be used in conjunction with total absorption spectrometry following β-decay (β-Oslo method) [7] and particle-γ coincidences from inverse-kinematics experiments [8]. This allows for study of unstable and/or chemically challenging nuclei.

The Oslo method itself does not provide the absolute NLD and γSF values, but rather the functional shapes. In order to determine the correct common slope of the NLD and γSF, as well as their absolute values, a normalization to auxiliary experimental data is required. Typical data for normalization are the s-wave resonance spacing, discrete resolved levels and average radiative width. The reliance on external data means that the accuracy of the final NLD and γSF is mostly determined by the accuracy of those data. The resonance spacings and radiative widths can be highly uncertain, especially in nuclei with few resonances. For the majority of unstable nuclei these have not even been measured. This means that alternative approaches for normalization have to be used especially for cases where no experimental resonance data are available. For nuclei close to stability these values can typically be estimated from systematics in the vicinity of the nucleus using models [7]. The down side of such normalized NLDs and γSFs is the introduction of model dependencies which may result in large uncertainties. A model independent approach is the use of the shape method [9, 10] to determine the slope of the γSF, however the method requires sufficient particle energy resolution and a well known level structure with fairly large energy spacing at low excitation energy. In this paper we will look at a possible third option in which only NLD from known discrete states is used to normalize the NLD.

In this paper we have analyzed data from a (p, d) reaction on ^{64}Ni to measure the NLD and γSF of ^{63}Ni. The level density of ^{63}Ni has previously been measured using particle evaporation spectra and shows significantly lower NLD than that expected from resonance spacing data [1, 11]. This makes ^{63}Ni a very interesting case study as a normalization only considering known discrete levels could resolve the discrepancy. In addition, the γSFs have previously been measured in many Ni isotopes and consistently show a strong low energy enhancement [12–17]. With this measurement the NLD and γSF will have been measured in most stable [12–14, 18] and several unstable Ni isotopes [15–18], allowing for investigations into the systematics of the γSF.

II. EXPERIMENT AND ANALYSIS

The experiment measuring particle-γ coincidences from the ^{64}Ni(p, d)^{63}Ni reaction was performed with a 27.4 MeV proton beam accelerated by the Separated Sector Cyclotron (SSC) at iThemba LABS. The 4.56 mg/cm^2 thick ^{64}Ni target was bombarded with a beam current of $\approx$ 1 pnA for about 15 hours at the center of the AFRODITE array [19]. The array consisted of eight Compton suppressed high purity germanium (HPGe) CLOVER detectors, six small (2"x2") and two large volume (3.5"x8") $LaBr_3$:Ce detectors. Particles from the reaction were measured by two silicon detectors of the S2 type in a ΔE-E configuration and placed down stream of the target. The ΔE detector had a thickness of 309 μm and the E detector was 1041 μm thick. In front of the particle telescope a 10 μm thick aluminum absorber

was placed to shield from δ-electrons. Signals from the detectors were read out using Pixie-16 digital pulse processors from XIA. Each detector was self-triggering and the pulse height, timestamp and constant fraction corrections of each event were stored to disk for offline analysis.

Particle-γ coincidences were found in the list mode data by placing time gates on the prompt time peak in the particle-γ time spectra. Background events were found by placing an off-prompt time gate of similar length. The mass and charge of the ejected particle, and thus the reaction channel, was selected by applying a graphical cut in the ΔE vs. E matrix. For each event the excitation energy of the residual ^{63}Ni nucleus was found from kinematic reconstruction assuming a two-body reaction. The resulting excitation energy and coincident γ-rays spectrum were then used to construct the prompt excitation-γ-ray energy matrix shown in fig. 1(a). A similar background excitation-γ-ray energy matrix was constructed from the events in the background time gate. After applying time and particle gates a total of $3,675,254$, $4,820,587$ and $5,735,151$ prompt particle-γ coincidences and $731,410$, $1,038,589$ and $788,504$ background events were found in the CLOVER, large $LaBr_3$:Ce and small $LaBr_3$:Ce detectors, respectively. The considerably lower background to prompt ratio for the small $LaBr_3$:Ce detectors can be attributed to their exceptionally high time resolution [20]. In the following analysis only particle-γ coincidences in the large $LaBr_3$:Ce detectors were considered as these exhibit far superior efficiency at high γ-ray energies which is important in the Oslo method.

A. The Oslo method

The starting point for the Oslo method is the excitation-γ matrix. The first step is to correct for the response of the γ-detector using the *unfolding method* [21]. The response function of the setup was found from simulations of the AFRODITE array using a model implemented in `Geant4` [22, 23]. The resulting unfolded matrix are shown in fig. 1(b). The peak at $E_x = 3.6$ MeV to the ground state was fitted and subtracted from the unfolded spectra with the justification being that this state is only populated directly from the reaction and has no feeding from the quasi-continuum.

Next is to find the first generation matrix using the *first generation method* [24]. The resulting first generation matrix contains the distribution of the first γ-rays emitted in cascades depopulating each excitation bin and are shown in fig. 1(c).

The first generation matrix are proportional to the NLD and γ-ray transmission coefficient via [6]

$$\Gamma(E_\gamma, E_x) \propto \mathcal{T}(E_\gamma)\rho(E_x - E_\gamma), \tag{1}$$

where $\Gamma(E_\gamma, E_x)$ is the bin with γ-ray energy E_γ and excitation energy E_x. $\mathcal{T}(E_\gamma)$ is the transmission coefficient for γ-ray energy E_γ and $\rho(E_x - E_\gamma)$ is the level density at the final excitation energy $E_f = E_x - E_\gamma$. The NLD and γ-ray transmission coefficients are extracted from the first generation matrix by fitting a theoretical matrix

$$\Gamma_{\rm th}(E_\gamma, E_x) = \frac{\rho(E_x - E_\gamma)\mathcal{T}(E_\gamma)}{\sum_{E_\gamma = E_\gamma^{\rm min}}^{E_x} \rho(E_x - E_\gamma)\mathcal{T}(E_\gamma)}, \tag{2}$$

where $\rho(E_x - E_\gamma)$ and $\mathcal{T}(E_\gamma)$ are treated as free variables for each final energy $E_f = E_x - E_\gamma$ and γ-ray energy E_γ. The fit was done by minimizing

$$\chi^2 = \sum_{E_x, E_\gamma} \left(\frac{\Gamma(E_\gamma, E_x) - \Gamma_{\rm th}(E_\gamma, E_x)}{\Delta\Gamma(E_\gamma, E_x)} \right)^2. \tag{3}$$

The region of the first generation matrix fitted was limited to a minimum γ-ray energy of 1500 keV and excitation energies between 3100 keV and 6600 keV to ensure only statistical decay were included. The region is highlighted by the dashed line in fig. 1(c).

The resulting theoretical first generation matrix are shown for a few select excitation bins together with the experimental matrix in fig. 2.

The NLD and γ-ray transmission coefficients resulting from the χ^2 minimization are not the physical values, but rather the shape as eq. (3) is symmetric under transformation

$$\begin{aligned} \tilde{\rho}(E_x - E_\gamma) &= A\rho(E_x - E_\gamma)e^{\alpha(E_x - E_\gamma)} \\ \tilde{\mathcal{T}}(E_\gamma) &= B\mathcal{T}(E_\gamma)e^{\alpha E_\gamma}, \end{aligned} \tag{4}$$

where A, B and α are transformation parameters. To obtain the physical transformation for the extracted NLD and γ-transmission coefficients a normalization to external data has to be performed, see section III. The γSF is related to the transmission coefficient via $f(E_\gamma) = \mathcal{T}(E_\gamma)/(2\pi E_\gamma^3)$, under the assumption that dipole transitions dominate the transmission coefficients.

III. NORMALIZATION OF LEVEL DENSITY & γ-RAY STRENGTH FUNCTION

The main auxiliary data required to normalize the NLD is known level densities from tabulated levels and the NLD at the neutron separation energy. Tabulated levels are converted to level density simply by counting the number of levels within each excitation bin and dividing by the bin width. This results in a level density that will have large fluctuations compared to Oslo method data as the experimental resolution has not yet been accounted for. The level density from known levels is smoothed with a Gaussian with FWHM of about 325 keV to match the experimental resolution for final excitation energy. Tabulated discrete levels were taken from the RIPL-3 library [3].

The level density at the neutron separation energy are found from the resonance spacing of s-wave resonances

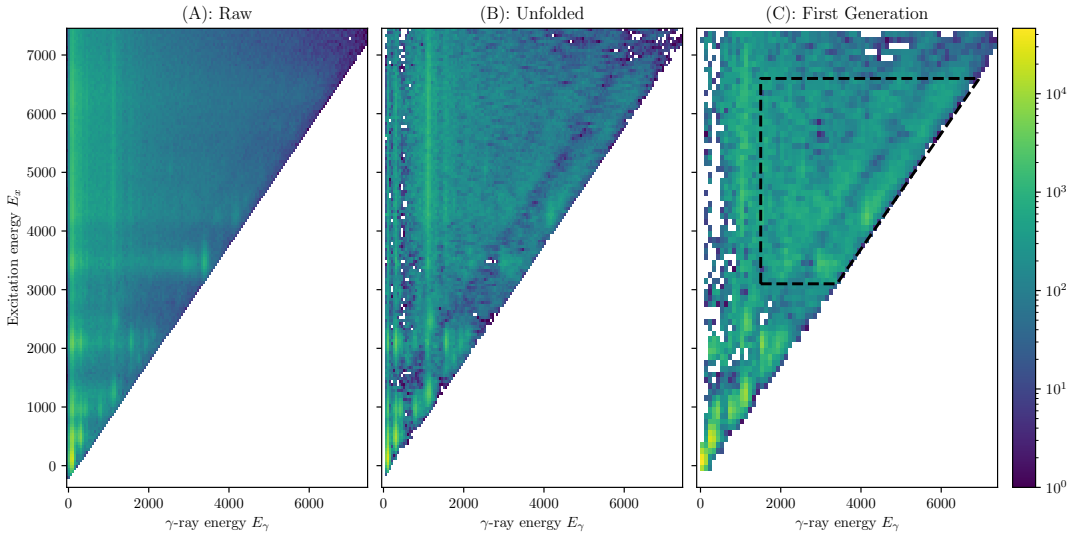

FIG. 1. The (a) raw, (b) unfolded and (c) first generation matrix.

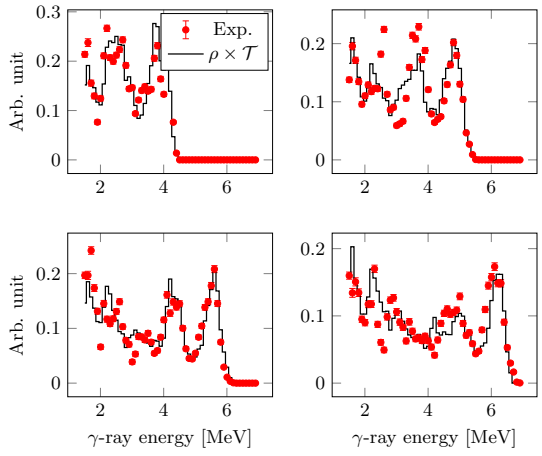

FIG. 2. ^{63}Ni primary γ-ray distribution at excitation energy 4 MeV (upper left), 5 MeV (upper right), 5.75 MeV (lower left) and 6.4 MeV (lower right). Red dots shows the experimental first generation spectra, while the solid black line is the product of the fitted NLD and γSF.

D_0 by [6]

$$\rho(S_n) = \frac{2}{g(S_n, J_t - 1/2) + g(S_n, J_t + 1/2)} \frac{1}{D_0} \quad (5)$$

where J_t is the ground state spin of the $A-1$ nucleus. The spin distribution $g(E_x, J)$ is given by the Ericson distribution [25]

$$g(E_x, J) = \exp\left(-\frac{J^2}{2\sigma^2(E_x)}\right) - \exp\left(-\frac{(J+1)^2}{2\sigma^2(E_x)}\right), \quad (6)$$

with the spin-cutoff parameter parameterized by [26]

$$\sigma^2(E_x) = \begin{cases} \sigma_d^2 & E < E_d \\ \sigma_d^2 + \frac{E - E_d}{S_n - E_d}(\sigma^2(S_n) - \sigma_d^2) & E \geq E_d. \end{cases} \quad (7)$$

The spin-cutoff parameter of the discrete levels ($E_d = 2.0$ MeV) is estimated to be $\sigma_d = 2.30(23)$ from tabulated discrete levels [3] and large scale shell model calculations [5], while the spin-cutoff parameter at the neutron separation energy was estimated to be $\sigma(S_n) = 3.68(21)$ estimated from the models of [27], [28] and [29]. The s-wave resonance spacing $D_0 = 16.0(30)$ keV was taken from the RIPL-3 database [3] resulting in a total level density at the neutron separation energy of 1730(363) MeV^{-1}.

The experimental NLD only extends up to 5.2 MeV and to properly compare with the level density at the neutron separation energy the NLD is extrapolated to S_n via a constant temperature (CT) formula [25]

$$\rho_{\mathrm{CT}}(E_x) = \frac{1}{T} \exp\left(\frac{E_x - E_{\mathrm{shift}}}{T}\right) \quad (8)$$

where the temperature T and shift parameter E_{shift} are treated as free parameters.

Data required to normalize the γSF is the average radiative width of s-wave resonances, as this value is related

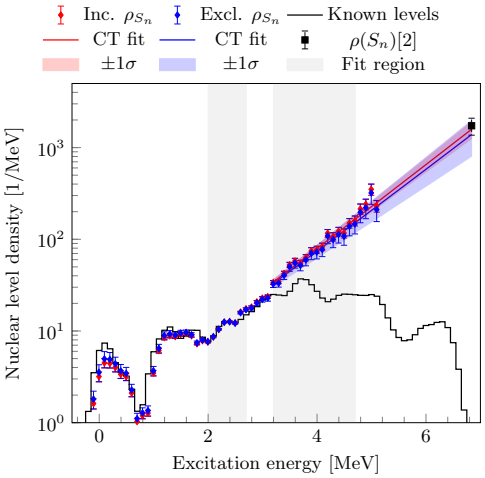

FIG. 3. The extracted and normalized NLD. The red circles are the experimental values, while the black solid line is the level density from the known resolved levels convoluted with the experimental resolution. The black dash-dotted line is the level density found from large scale shell model calculations using the ca48mh1 interaction [5]. The black solid square is the level density at the neutron separation energy found from s-wave resonance spacing reported by [2–4]. The red solid line shows the level density from the fitted CT model while the red shaded area is the $\pm1\sigma$ confidence interval.

to the γSF and NLD via [30]

$$\langle\Gamma_{\gamma 0}\rangle = \frac{D_0}{2}\int_0^{S_n} dE_\gamma E_\gamma^3 f(E_\gamma)\rho(S_n - E_\gamma) \times \left[g(S_n - E_\gamma, 1/2) + g(S_n - E_\gamma, 3/2)\right] E_\gamma. \quad (9)$$

Due to the limits selected (see sect. II A) for the extraction of the NLD and γSF the experimental data only extends up to $E_x = 5.2$ MeV and E_γ between 1.5 and 6.6 MeV, respectively. To evaluate the integral in eq. (9) the NLD was extrapolated with the constant temperature formula, eq. (8), between 5.2 MeV and the neturon separation energy. The γSF was extrapolated using $f(E_\gamma) = Ce^{\eta E_\gamma}$, and $f(E_\gamma) = Ce^{\eta E_\gamma}/E_\gamma^3$ for energies between 0 and 1.5 MeV, and 6.6 MeV and the neutron separation energy, respectively. The average radiative width of s-wave resonances in ^{63}Ni was found to be 534(214) meV by a weighted average of all the tabulated values found in [4]. Due to the large spread of the tabulated values a large uncertainty of 40% was assumed. All normalization parameters adopted in this analysis are listed in table I. The normalization parameters A, B and α was found by sampling the total likelihood function

$$\mathcal{L}(\boldsymbol{\theta}) = \prod_i \mathcal{L}_i(\boldsymbol{\theta}) \quad (10)$$

TABLE I. List of parameters used to normalize the NLD and γSF. The spin-cut at S_n $\sigma(S_n)$ is estimated from the model predictions of [27], [28] and [29] while the discrete levels spin-cut is estimated from the discrete states [3] and shell model calculations [5]. The s-wave resonance spacing D_0 are taken from [3], while the $\langle\Gamma_\gamma\rangle$ is a weighted average of tabulated radiative widths in [4].

S_n	6.838 MeV
D_0	16.0(30) keV
$\sigma(S_n)$	3.63(21)
E_d	2.0 MeV
$\sigma(E_d)$	2.3(23)
$\langle\Gamma_\gamma\rangle$	534(214) meV
$\rho(S_n)$	1730(363) 1/MeV

using the Bayesian sampling package `UltraNest` [31]. All experimental data are assumed to be normally distributed, giving the likelihoods

$$\ln\mathcal{L}_{\text{discrete}} = \sum_i \ln\frac{1}{\sqrt{2\pi\sigma_{j,\text{Oslo}}(\boldsymbol{\theta})}} - \frac{1}{2}\sum_i\left(\frac{\rho_{j,\text{discrete}} - \rho_{j,\text{Oslo}}(\boldsymbol{\theta})}{\sigma_{j,\text{Oslo}}(\boldsymbol{\theta})}\right)^2, \quad (11)$$

$$\ln\mathcal{L}_{\text{CT}} = \sum_i \ln\frac{1}{\sqrt{2\pi\sigma_{j,\text{Oslo}}(\boldsymbol{\theta})}} - \frac{1}{2}\sum_i\left(\frac{\rho_{j,\text{CT}} - \rho_{j,\text{Oslo}}(\boldsymbol{\theta})}{\sigma_{j,\text{Oslo}}(\boldsymbol{\theta})}\right)^2, \quad (12)$$

$$\ln\mathcal{L}_{\rho_{S_n}} = \left(\frac{\rho_{S_n} - \rho_{S_n,\text{CT}}(\boldsymbol{\theta})}{\sigma_{\rho_{S_n}}}\right)^2, \quad (13)$$

$$\ln\mathcal{L}_{\langle\Gamma_{\gamma 0}\rangle} = \left(\frac{\langle\Gamma_{\gamma 0}\rangle_{\text{exp}} - \langle\Gamma_{\gamma 0}\rangle_{\text{Oslo}}(\boldsymbol{\theta})}{\sigma_{\langle\Gamma_{\gamma 0}\rangle_{\text{exp}}}}\right)^2. \quad (14)$$

The parameters $\boldsymbol{\theta} = (A, B, \alpha, T, E_{\text{shift}}, \sigma_D, \sigma_{S_n})$ have a uniform prior between 0 and 5 for A and B and -1 MeV^{-1} and 1 MeV^{-1} for α. The temperature and shift parameters also used a uniform prior between 0.2 and 2 MeV and -10 and 10 MeV, respectively. The spin cut-off parameters were included as nuance parameters with normal distributed priors to ensure proper propagation of errors. The resulting normalized NLD and γSF are shown as red circles in fig. 3 and 4, respectively. The discrete likelihood, eq. (11) was limited to data points between 2 and 2.7 MeV, while the CT formula was fitted between 3.2 and 4.7 MeV. To investigate the sensitivity to the resonance spacing the analysis was repeated, but excluding eq. (13) in the total likelihood and resulted in the NLD and γSF shown as blue circles in fig. 3 and 4, respectively.

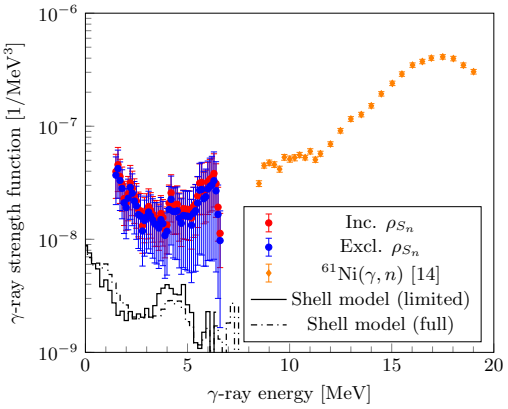

FIG. 4. Extracted γSF when including the NLD at S_n from resonance spacings in the normalization are shown by the red circles while the blue circles only considers the level density from known levels. The orange diamonds are the γSF of ^{61}Ni measured by [14]. The black line shows the calculated M1 strength from shell model calculations [5] considering only decay from levels within the fit region, while the dash-dotted line includes all levels found in the shell model calculation.

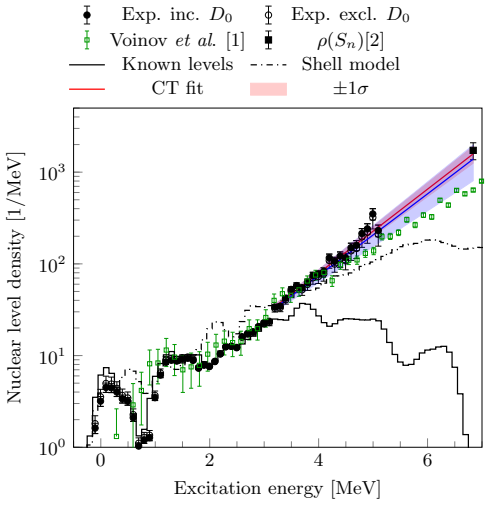

FIG. 5. Comparison between the presented NLD shown by the black circles (filled including the ρ_{S_n} point in the normalization, the open circles excludes this point) and the NLD found in large scale shell model calculations [5] shown by the dash-dotted line and the green open boxes are the NLD found in particle evaporation studies by A. Voinov *et al.* [1].

IV. DISCUSSION AND COMPARISON

Level density

We find that the experimental NLD fits exceptionally well with the tabulated discrete NLD up to about $E_x \approx 3.6$ MeV indicating that the level scheme might be complete up to even higher excitation energies, than the evaluated $E_x = 2.7$ MeV [3].

Comparing the two normalizations we see that the one including ρ_{S_n} results in a slightly steeper slope. overall the two normalizations are well within the error-bars of each other demonstrating that normalization without knowledge of the NLD at the neutron separation energy are viable.

Fig. 5 shows the NLD compared with the experimental NLD found from particle evaporation spectra of [1] and the NLD found in large scale shell model (SM) calculations of [5]. The SM results clearly overestimates the NLD between 1.8 and 3.7 MeV while underestimating above 4 MeV up to around 6 MeV where the model space seems to be exhausted. The NLD found from evaporation studies fits well within the error bars up to about 4.5 MeV where the presented NLD seems to tend to higher densities.

In fig. 6 the NLDs of ^{59,60,64,65,67,69,70}Ni [12, 13, 15–18] are shown together with the measured ^{63}Ni isotope. We observe a clear trend of the absolute NLD increases with the mass number while the temperature (i.e. the slope) decreases with mass number.

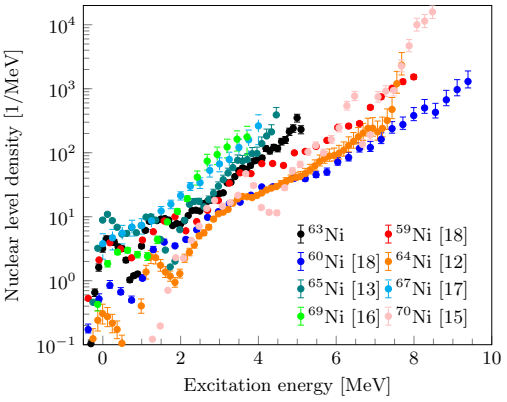

FIG. 6. NLDs measured with the Oslo method in Ni isotopes.

γ-ray strength function

The extracted γSF features a strong upbend at low energies similar to what has been seen in other Ni isotopes [12–16, 18], as well as other nuclei in the same mass region [32–34]. Comparing the measured strength function to the M1 strength predicted from the SM cal-

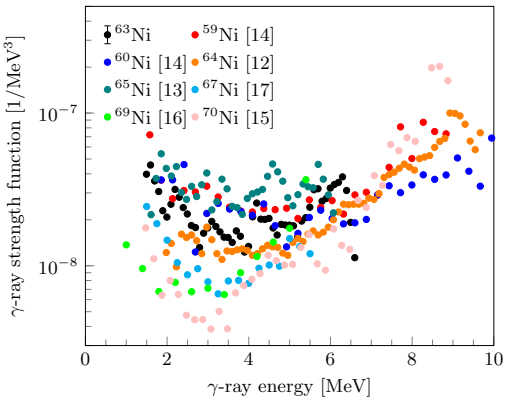

FIG. 7. γSFs measured in Ni isotopes.

culations of [5] we see that qualitatively these have a similar shape, although the absolute values of the SM calculations are considerably lower. Comparison with the photo-absorption cross section of ^{61}Ni [14] we find a reasonably good agreement as the giant dipole resonance evolves slowly with mass number. The normalized γSF has a considerably large uncertainty band with the dominating contributing factor being the uncertainty in the average radiative width. Excluding the $\rho(S_n)$ in the normalization does also have a large impact on the uncertainties of the normalization for the γSF, increasing the size of the error bars from $\approx$ 45% to $\approx$ 80%, especially at higher γ-ray energies.

In fig. 7 we show the γSF for ^{59,60,64,65,67,69,70}Ni [12–17] together with the presented γSF. From this comparison we can see a clear trend with the strength below $\approx$ 4.5 MeV significantly decreasing with higher mass numbers. This is especially apparent in the unstable neutron rich nuclei ($A = 67, 69$ and 70). The outlier are the γSF of ^{65}Ni which have the highest strength overall.

V. SUMMARY

We have measured the NLD and γSF of ^{63}Ni and found that the NLD agrees well with the density found from known levels, and are compatible with the NLD at the neutron separation energy found in neutron resonance studies. The NLD of [1] agrees with the presented NLD for excitation energies up to about 4.7 MeV where the presented NLD seems to be somewhat steeper. Based on this we conclude that our results tends to favour the NLD found in resonance studies, rather than those of [1].

The measured γSF features a strong low energy enhancement similar to that found in other Ni isotopes. Shell model calculations from [5] suggests that the enhancement may be due to M1 transitions within the quasi-continuum. Compared with (γ, n) [14] data for ^{61}Ni there may be a pygmy resonance around 7-8 MeV, but due to the large uncertainties in the absolute value of the measured γSF we cannot conclude.

In general the exclusion of s-wave spacing in the overall fit of the NLD and γSF resulted in very similar results, although with considerable larger uncertainties when extrapolating towards the neutron separation energy. Based on this we can conclude that if the level scheme is sufficiently well known a reasonably good normalization for the NLD can be obtained without resonance data.

ACKNOWLEDGMENTS

The authors would like to thank iThemba LABS operations for stable running conditions. This work is based on research supported by the Research Council of Norway under project Grants no. 263030 (V.W.I, S.S.), by the National Research Foundation of South Africa under grant no. 105207, 99037, 90741 and 118846.

[1] A. V. Voinov, S. M. Grimes, C. R. Brune, T. Massey, and A. Schiller, Recent experimental results on level densities for compound reaction calculations, EPJ Web of Conferences **21** (2012).

[2] S. F. Mughabghab, *Atlas of Neutron Resonances : Volume 1: Resonance Properties and Thermal Cross Sections Z= 1-60.*, sixth ed., Atlas of Neutron Resonances (Elsevier Science, 2018).

[3] R. Capote, M. Herman, P. Obložinský, P. G. Young, S. Goriely, T. Belgya, A. V. Ignatyuk, A. J. Koning, S. Hilaire, V. A. Plujko, M. Avrigeanu, O. Bersillon, M. B. Chadwick, T. Fukahori, Z. Ge, Y. Han, S. Kailas, J. Kopecky, V. M. Maslov, G. Reffo, M. Sin, E. S. Soukhovitskii, and P. Talou, RIPL - Reference Input Parameter Library for Calculation of Nuclear Reactions and Nuclear Data Evaluations, Nuclear Data Sheets **110**, 3107 (2009).

[4] C. Lederer, C. Massimi, E. Berthoumieux, N. Colonna, R. Dressler, C. Guerrero, F. Gunsing, F. Käppeler, N. Kivel, M. Pignatari, R. Reifarth, D. Schumann, A. Wallner, S. Altstadt, S. Andriamonje, J. Andrzejewski, L. Audouin, M. Barbagallo, V. Bécares, F. Bečvář, F. Belloni, B. Berthier, J. Billowes, V. Boccone, D. Bosnar, M. Brugger, M. Calviani, F. Calviño, D. Cano-Ott, C. Carrapiço, F. Cerutti, E. Chiaveri, M. Chin, G. Cortés, M. A. Cortés-Giraldo, I. Dillmann, C. Domingo-Pardo, I. Duran, N. Dzysiuk, C. Eleftheriadis, M. Fernández-Ordóñez, A. Ferrari, K. Fraval, S. Ganesan, A. R. García, G. Giubrone, M. B. Gómez-Hornillos, I. F. Gonçalves, E. González-Romero,

F. Gramegna, E. Griesmayer, P. Gurusamy, S. Harrisopulos, M. Heil, K. Ioannides, D. G. Jenkins, E. Jericha, Y. Kadi, D. Karadimos, G. Korschinek, M. Krtička, J. Kroll, C. Langer, E. Lebbos, H. Leeb, L. S. Leong, R. Losito, M. Lozano, A. Manousos, J. Marganiec, S. Marrone, T. Martinez, P. F. Mastinu, M. Mastromarco, M. Meaze, E. Mendoza, A. Mengoni, P. M. Milazzo, F. Mingrone, M. Mirea, W. Mondalaers, C. Paradela, A. Pavlik, J. Perkowski, R. Plag, A. Plompen, J. Praena, J. M. Quesada, T. Rauscher, A. Riego, F. Roman, C. Rubbia, R. Sarmento, P. Schillebeeckx, S. Schmidt, G. Tagliente, J. L. Tain, D. Tarrío, L. Tassan-Got, A. Tsinganis, L. Tlustos, S. Valenta, G. Vannini, V. Variale, P. Vaz, A. Ventura, M. J. Vermeulen, R. Versaci, V. Vlachoudis, R. Vlastou, T. Ware, M. Weigand, C. Weiß, T. J. Wright, and P. Žugec, Ni 62 (n, γ) and Ni 63 (n, γ) cross sections measured at the n-TOF facility at CERN, Physical Review C - Nuclear Physics **89**, 25810 (2014).

[5] J. E. Midtbø, A. C. Larsen, T. Renstrøm, F. L. Bello Garrote, and E. Lima, Consolidating the concept of low-energy magnetic dipole decay radiation, Physical Review C **98**, 064321 (2018).

[6] A. Schiller, L. Bergholt, M. Guttormsen, E. Melby, J. Rekstad, and S. Siem, Extraction of level density and γ strength function from primary γ spectra, Nuclear Instruments and Methods in Physics Research, Section A: Accelerators, Spectrometers, Detectors and Associated Equipment **447**, 498 (2000).

[7] A. Spyrou, S. N. Liddick, A. C. Larsen, M. Guttormsen, K. Cooper, A. C. Dombos, D. J. Morrissey, F. Naqvi, G. Perdikakis, S. J. Quinn, T. Renstrøm, J. A. Rodriguez, A. Simon, C. S. Sumithrarachchi, and R. G. Zegers, Novel technique for constraining r -process (n, γ) reaction rates, Physical Review Letters **113**, 232502 (2014).

[8] V. W. Ingeberg, S. Siem, M. Wiedeking, K. Sieja, D. L. Bleuel, C. P. Brits, T. D. Bucher, T. S. Dinoko, J. L. Easton, A. Görgen, M. Guttormsen, P. Jones, B. V. Kheswa, N. A. Khumalo, A. C. Larsen, E. A. Lawrie, J. J. Lawrie, S. N. Majola, K. L. Malatji, L. Makhathini, B. Maqabuka, D. Negi, S. P. Noncolela, P. Papka, E. Sahin, R. Schwengner, G. M. Tveten, F. Zeiser, and B. R. Zikhali, First application of the Oslo method in inverse kinematics, European Physical Journal A **56**, 68 (2020).

[9] M. Wiedeking, M. Guttormsen, A. C. Larsen, F. Zeiser, A. Görgen, S. N. Liddick, D. Mücher, S. Siem, and A. Spyrou, Independent normalization for γ -ray strength functions: The shape method, Physical Review C **104**, 014311 (2021).

[10] D. Mücher, A. Spyrou, M. Wiedeking, M. Guttormsen, A. C. Larsen, F. Zeiser, C. Harris, A. L. Richard, M. K. Smith, A. Görgen, S. N. Liddick, S. Siem, H. Berg, J. A. Clark, P. A. DeYoung, A. C. Dombos, B. Greaves, L. Hicks, R. Kelmar, S. Lyons, J. Owens-Fryar, A. Palmisano, D. Santiago-Gonzalez, G. Savard, and W. W. von Seeger, A novel approach for extracting model-independent nuclear level densities far from stability (2020).

[11] B. M. Oginni, S. M. Grimes, A. V. Voinov, A. S. Adekola, C. R. Brune, D. E. Carter, Z. Heinen, D. Jacobs, T. N. Massey, J. E. O'Donnell, and A. Schiller, Test of level density models from reactions of Li6 on Fe58 and Li7 on Fe57, Physical Review C **80**, 34305 (2009).

[12] L. Crespo Campo, F. L. Bello Garrote, T. K. Eriksen, A. Görgen, M. Guttormsen, K. Hadynska-Klek, M. Klintefjord, A. C. Larsen, T. Renstrøm, E. Sahin, S. Siem, A. Springer, T. G. Tornyi, and G. M. Tveten, Statistical γ -decay properties of Ni 64 and deduced (n,γ) cross section of the s -process branch-point nucleus Ni 63, Physical Review C **94**, 44321 (2016).

[13] L. C. Campo, A. C. Larsen, F. L. Garrote, T. K. Eriksen, F. Giacoppo, A. Görgen, M. Guttormsen, M. Klintefjord, T. Renstrøm, E. Sahin, S. Siem, T. G. Tornyi, and G. M. Tveten, Investigating the γ decay of Ni 65 from particle-γ coincidence data, Physical Review C **96**, 14312 (2017).

[14] H. Utsunomiya, T. Renstrøm, G. M. Tveten, S. Goriely, S. Katayama, T. Ari-Izumi, D. Takenaka, D. Symochko, B. V. Kheswa, V. W. Ingeberg, T. Glodariu, Y. W. Lui, S. Miyamoto, A. C. Larsen, J. E. Midtbø, A. Görgen, S. Siem, L. C. Campo, M. Guttormsen, S. Hilaire, S. Péru, and A. J. Koning, Photoneutron cross sections for Ni isotopes: Toward understanding (n,γ) cross sections relevant to weak s -process nucleosynthesis, Physical Review C **98**, 54619 (2018).

[15] A. C. Larsen, J. E. Midtbø, M. Guttormsen, T. Renstrøm, S. N. Liddick, A. Spyrou, S. Karampagia, B. A. Brown, O. Achakovskiy, S. Kamerdzhiev, D. L. Bleuel, A. Couture, L. C. Campo, B. P. Crider, A. C. Dombos, R. Lewis, S. Mosby, F. Naqvi, G. Perdikakis, C. J. Prokop, S. J. Quinn, and S. Siem, Enhanced low-energy γ-decay strength of Ni 70 and its robustness within the shell model, Physical Review C **97**, 54329 (2018).

[16] A. Spyrou, A. C. Larsen, S. N. Liddick, F. Naqvi, B. P. Crider, A. C. Dombos, M. Guttormsen, D. L. Bleuel, A. Couture, L. C. Campo, R. Lewis, S. Mosby, M. R. Mumpower, G. Perdikakis, C. J. Prokop, S. J. Quinn, T. Renstrom, S. Siem, and R. Surman, Neutron-capture rates for explosive nucleosynthesis: The case of 68Ni(n, γ)69Ni, Journal of Physics G: Nuclear and Particle Physics **44**, 044002 (2017).

[17] V. W. Ingeberg, S. Siem, M. Wiedeking, S. Goriely, K. Abrahams, K. Arnswald, F. Bello Garrote, T. Berry, D. L. Bleuel, J. Cederkäll, T. Christoffersen, D. Cox, L. Crespo Campo, H. De Witte, L. Gaffney, A. Görgen, C. Henrich, A. Illana Sison, P. Jones, B. Kheswa, T. Kröll, S. Majola, T. Nogwanya, J. Ojala, J. Pakarinen, G. Rainovski, P. Reiter, D. Rosiak, M. Von Schmid, M. Seidlitz, B. Siebeck, J. Snäll, K. Sowazi, G. M. Tveten, N. Warr, and F. Zeiser, Nuclear level density and γ-ray strength function of unstable Ni 67 (in preparation) (2022).

[18] T. Renstrøm, G. M. Tveten, J. E. Midtbø, H. Utsunomiya, O. Achakovskiy, S. Kamerdzhiev, B. A. Brown, A. Avdeenkov, T. Ari-izumi, A. Görgen, S. M. Grimes, M. Guttormsen, T. W. Hagen, V. W. Ingeberg, S. Katayama, B. V. Kheswa, A. C. Larsen, Y. W. Lui, H. T. Nyhus, S. Siem, D. Symochko, D. Takenaka, and A. V. Voinov, Experimental γ-decay strength in Ni 59, 60 compared with microscopic calculations, arXiv (2018).

[19] M. Lipoglavšek, A. Likar, M. Vencelj, T. Vidmar, R. A. Bark, E. Gueorguieva, F. Komati, J. J. Lawrie, S. M. Maliage, S. M. Mullins, S. H. Murray, and T. M. Ramashidzha, Measuring high-energy γ-rays with Ge clover detectors, Nuclear Instruments and Methods in Physics Research, Section A: Accelerators, Spectrometers, Detectors and Associated Equipment **557**, 523 (2006).

[20] L. Msebi, V. W. Ingeberg, P. Jones, J. F. Sharpey-

Schafer, A. A. Avaa, T. D. Bucher, C. P. Brits, M. V. Chisapi, D. J. C. Kenfack, E. A. Lawrie, K. L. Malatji, B. Maqabuka, L. Makhathini, S. P. Noncolela, J. Ndayishimye, A. Netshiya, O. Shrinda, M. Wiedeking, and B. R. Zikhali, A fast-timing array of 2" x 2" LaBr3:Ce detectors for lifetime measurements of excited nuclear states, Nuclear Instruments and Methods in Physics Research Section A: Accelerators, Spectrometers, Detectors and Associated Equipment **1026**, 166195 (2022).

[21] M. Guttormsen, T. S. Tveter, L. Bergholt, F. Ingebretsen, and J. Rekstad, The unfolding of continuum γ-ray spectra, Nuclear Instruments and Methods in Physics Research, Section A: Accelerators, Spectrometers, Detectors and Associated Equipment **374**, 371 (1996).

[22] S. Agostinelli, J. Allison, K. Amako, J. Apostolakis, H. Araujo, P. Arce, M. Asai, D. Axen, S. Banerjee, G. Barrand, F. Behner, L. Bellagamba, J. Boudreau, L. Broglia, A. Brunengo, H. Burkhardt, S. Chauvie, J. Chuma, R. Chytracek, G. Cooperman, G. Cosmo, P. Degtyarenko, A. Dell'Acqua, G. Depaola, D. Dietrich, R. Enami, A. Feliciello, C. Ferguson, H. Fesefeldt, G. Folger, F. Foppiano, A. Forti, S. Garelli, S. Giani, R. Giannitrapani, D. Gibin, J. J. G. Cadenas, I. González, G. G. Abril, G. Greeniaus, W. Greiner, V. Grichine, A. Grossheim, S. Guatelli, P. Gumplinger, R. Hamatsu, K. Hashimoto, H. Hasui, A. Heikkinen, A. Howard, V. Ivanchenko, A. Johnson, F. W. Jones, J. Kallenbach, N. Kanaya, M. Kawabata, Y. Kawabata, M. Kawaguti, S. Kelner, P. Kent, A. Kimura, T. Kodama, R. Kokoulin, M. Kossov, H. Kurashige, E. Lamanna, T. Lampén, V. Lara, V. Lefebure, F. Lei, M. Liendl, W. Lockman, F. Longo, S. Magni, M. Maire, E. Medernach, K. Minamimoto, P. M. de Freitas, Y. Morita, K. Murakami, M. Nagamatu, R. Nartallo, P. Nieminen, T. Nishimura, K. Ohtsubo, M. Okamura, S. O'Neale, Y. Oohata, K. Paech, J. Perl, A. Pfeiffer, M. G. Pia, F. Ranjard, A. Rybin, S. Sadilov, E. D. Salvo, G. Santin, T. Sasaki, N. Savvas, Y. Sawada, S. Scherer, S. Sei, V. Sirotenko, D. Smith, N. Starkov, H. Stoecker, J. Sulkimo, M. Takahata, S. Tanaka, E. Tcherniaev, E. S. Tehrani, M. Tropeano, P. Truscott, H. Uno, L. Urban, P. Urban, M. Verderi, A. Walkden, W. Wander, H. Weber, J. P. Wellisch, T. Wenaus, D. C. Williams, D. Wright, T. Yamada, H. Yoshida, and D. Zschiesche, Geant4—a simulation toolkit, Nuclear Instruments and Methods in Physics Research Section A: Accelerators, Spectrometers, Detectors and Associated Equipment **506**, 250 (2003).

[23] V. W. Ingeberg, AFRODITE (2022).

[24] M. Guttormsen, T. Ramsøy, and J. Rekstad, The first generation of γ-rays from hot nuclei, Nuclear Inst. and Methods in Physics Research, A **255**, 518 (1987).

[25] T. Ericson, A statistical analysis of excited nuclear states, Nuclear Physics **11**, 481 (1959).

[26] M. Guttormsen, S. Goriely, A. C. Larsen, A. Görgen, T. W. Hagen, T. Renstrøm, S. Siem, N. U. Syed, G. Tagliente, H. K. Toft, H. Utsunomiya, A. V. Voinov, and K. Wikan, Quasicontinuum γ decay of Zr 91,92: Benchmarking indirect (n,γ) cross section measurements for the s process, Physical Review C **96**, 24313 (2017).

[27] T. v. Egidy and D. Bucurescu, Systematics of nuclear level density parameters, Physical Review C **72**, 044311 (2005).

[28] A. Gilbert and A. G. W. Cameron, a Composite Nuclear-Level Density Formula With Shell Corrections, Canadian Journal of Physics **43**, 1446 (1965).

[29] T. von Egidy and D. Bucurescu, Experimental energy-dependent nuclear spin distributions, Phys. Rev. C **80**, 54310 (2009).

[30] J. Kopecky and M. Uhl, Test of gamma-ray strength functions in nuclear reaction model calculations, Physical Review C **41**, 1941 (1990).

[31] J. Buchner, UltraNest - a robust, general purpose Bayesian inference engine, Journal of Open Source Software **6**, 3001 (2021).

[32] A. C. Larsen, N. Blasi, A. Bracco, F. Camera, T. K. Eriksen, A. Görgen, M. Guttormsen, T. W. Hagen, S. Leoni, B. Million, H. T. Nyhus, T. Renstrøm, S. J. Rose, I. E. Ruud, S. Siem, T. Tornyi, G. M. Tveten, A. V. Voinov, and M. Wiedeking, Evidence for the dipole nature of the low-energy γ enhancement in Fe56, Physical Review Letters **111**, 242504 (2013).

[33] A. C. Larsen, M. Guttormsen, N. Blasi, A. Bracco, F. Camera, L. C. Campo, T. K. Eriksen, A. Görgen, T. W. Hagen, V. W. Ingeberg, B. V. Kheswa, S. Leoni, J. E. Midtbø, B. Million, H. T. Nyhus, T. Renstrøm, S. J. Rose, I. E. Ruud, S. Siem, T. G. Tornyi, G. M. Tveten, A. V. Voinov, M. Wiedeking, and F. Zeiser, Low-energy enhancement and fluctuations of γ-ray strength functions in 56,57 Fe: Test of the Brink-Axel hypothesis, Jour. Phys. G Nucl. and Part. Phys. **44**, 64005 (2017).

[34] T. Renstrøm, H. T. Nyhus, H. Utsunomiya, R. Schwengner, S. Goriely, A. C. Larsen, D. M. Filipescu, I. Gheorghe, L. A. Bernstein, D. L. Bleuel, T. Glodariu, A. Görgen, M. Guttormsen, T. W. Hagen, B. V. Kheswa, Y. W. Lui, D. Negi, I. E. Ruud, T. Shima, S. Siem, K. Takahisa, O. Tesileanu, T. G. Tornyi, G. M. Tveten, and M. Wiedeking, Low-energy enhancement in the γ -ray strength functions of Ge 73,74, Physical Review C **93**, 64302 (2016).

Paper IV

A fast timing array 2" x 2" LaBr3:Ce for lifetime measurements of excited nuclear states

L. Msebi, V. W. Ingeberg, P. Jones, J. F. Sharpey-Schafer, A. A. Avaa, T. D. Bucher, C. P. Brits, M. V. Chisapi, D. J. C. Kenfack, E. A. Lawrie, K. L. Malatji, B. Maqabuka, L. Makhathini, S. P. Noncolela, J. Ndayishimye, A. Netshiya, O. Shrinda, M. Wiedeking, B. R. Zikhali

Published in *Nuclear Inst. and Methods in Physics Research, A*, **1026**:166195 (2022), DOI: 10.1016/j.nima.2021.166195

IV

Nuclear Inst. and Methods in Physics Research, A 1026 (2022) 166195

Contents lists available at ScienceDirect

Nuclear Inst. and Methods in Physics Research, A

journal homepage: www.elsevier.com/locate/nima

A fast-timing array of 2" x 2" $LaBr_3$:Ce detectors for lifetime measurements of excited nuclear states

L. Msebi [a,b,*], V.W. Ingeberg [c], P. Jones [b], J.F. Sharpey-Schafer [f], A.A. Avaa [b,e], T.D. Bucher [a], C.P. Brits [b,d], M.V. Chisapi [b,d], D.J.C. Kenfack [b,d], E.A. Lawrie [b], K.L. Malatji [b,d], B. Maqabuka [a,b], L. Makhathini [b], S.P. Noncolela [a,b], J. Ndayishimye [b], A. Netshiya [b], O. Shrinda [g], M. Wiedeking [b,e], B.R. Zikhali [a,b]

[a] University of Western Cape, Physics Department, P/B X17, Bellville, ZA7535, South Africa
[b] Department of Subatomic Physics, iThemba Laboratory for Accelerator Based Sciences, P.O Box 722, Somerset West, ZA-7129, South Africa
[c] Department of Physics, University of Oslo, N-0316, Oslo, Norway
[d] Physics Department, Stellenbosch University, P/B X1, Matieland, 7602, South Africa
[e] School of Physics, University of the Witwatersrand, 1 Jan Smuts Avenue, Braamfontein, Johannesburg, 2000, South Africa
[f] Department of Physics, University of Zululand, Private Bag X1001, KwaDlangezwa, 3886, South Africa
[g] Sol Plaatje University, Department of Physical and Earth Sciences, Private Bag X5008, Kimberley 8301, South Africa

ARTICLE INFO

Keywords:
Lanthinum Bromide
Lifetime measurements
Digital pulse processing
Slope method
Centroid shift method

ABSTRACT

With its unique combination of excellent timing properties and good energy resolution, $LaBr_3$:Ce detectors have proven to be effective tool in gamma spectroscopy and in particular fast-timing studies. Eight 2" x 2" $LaBr_3$:Ce detectors used in conjunction with the 16 channel all-digital waveform 500 MHz acquisition module, PIXIE-16 were commissioned at iThemba Laboratory for Accelerator Based Sciences, South Africa. The results presented here give insight of the performance of the 2" x 2" $LaBr_3$ detectors when used in conjunction with a digital pulse processing (DPP) module and electronic read-out module. Initial commissioning experiments were done using radioactive sources, including ^{60}Co, ^{152}Eu and ^{67}Ga. The detectors were then exposed to an in-beam environment using the AFRODITE array with targets ^{45}Sc and ^{64}Ni, with a proton beam energy of 27 MeV.

1. Introduction

In the study of nuclear spectroscopy, it is desirable to detect gamma rays with high efficiency, good energy resolution, as well as to study decay properties of excited states with very short lifetimes. Previously there were limitations obtaining full energy peak events while benefiting from excellent timing resolution. This was as a consequence that scintillator detectors are traditionally known to have poor energy resolution. The advent of $LaBr_3$:Ce detectors has made it possible to achieve excellent timing resolution and good energy resolution with easy maintenance. Often, these detectors are used with the conventional analogue acquisition system. The present work makes use of these detectors together with high speed digital readout electronics. Digital pulse processing (DPP) modules boast of on-board processing as well as the ability to detect pulse pileup, energy filtering, record time stamps, coincidence triggering, and perform pulse shape analysis.

Excited states in a crystal scintillator decay by emission of scintillation light which directly influences the timing resolution. The short decay time of these detectors also means that they are not susceptible to deadtime when exposed to high count rates. $LaBr_3$:Ce detectors have a very high light output of around 61×10^3 photons per MeV [1], which is significantly larger when compared to that of the NaI scintillator (38×10^3 ph/MeV [2]). Because the light output is proportional to the energy absorbed and provides better statistics and signal-to-noise ratio, it makes the high light output beneficial for energy resolution. The $LaBr_3$:Ce is an inorganic crystal with an hexagonal (UCL3 type) structure with a P63/m space group [3]. The crystals are cerium Ce^{3+} doped thus producing luminescence in the blue/UV part of the electromagnetic spectrum (λ max = 380 nm) [4]. The crystal shape optimizes the solid angle thus improving light collection and time resolution. $LaBr_3$:Ce detectors vary in dimensions with the commonly used ranging from 1" x 1" to 3.5" x 8". Choosing the optimal crystal size is often challenging since a delicate balance has to be reached between the intrinsic time resolution and the detector efficiency. The intrinsic time resolution weakens with the increasing crystal size whereas the converse is true for detector efficiency.

The measurement of lifetimes of excited nuclear states gives one of the most important information in determining the structure of an

* Corresponding author at: University of Western Cape, Physics Department, P/B X17, Bellville, ZA7535, South Africa.
E-mail address: msebi@tlabs.ac.za (L. Msebi).

https://doi.org/10.1016/j.nima.2021.166195
Received 25 July 2021; Received in revised form 19 November 2021; Accepted 29 November 2021
Available online 17 December 2021

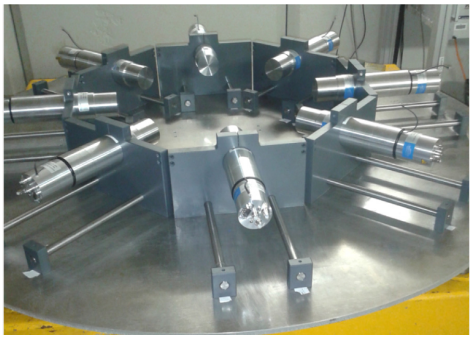

Fig. 1. The new array commissioned recently at iThemba LABS consisting of eight 2" x 2" $LaBr_3$:Ce detectors.

isotope and testing nuclear models. The lifetime of a state, together with its decay branching ratios, gives a direct measurement of the nuclear matrix elements joining an initial state to the final state. The advantage of direct electronic measurements of lifetimes is that they can be very accurate and free of many systematic errors that affect other measurements. When coupled to a gamma-ray spectrometer array such as the AFRODITE array [5], a hybrid array with capabilities of excellent energy and time resolution is obtained. These arrays are effective in measuring sub-nanosecond lifetimes, using γ-γ coincidences, over a wide range of energies [6–12]. We present here results obtained from measuring radioactive sources with 2" x 2" $LaBr_3$:Ce detectors and those obtained from in-beam measurements obtained by incorporating these detectors to the AFRODITE array.

2. Radioactive sources measurements

To test the performance of the recently commissioned eight 2" x 2" $LaBr_3$:Ce detectors, several measurements were performed with various sources. The 2" x 2" $LaBr_3$:Ce detectors with Brilliance:Ce-380 crystals were manufactured by Saint-Gobain Crystals coupled to a R2083 photomultiplier tube (PMT). The number 380 indicate the mean value of the wavelength of the emitted scintillation light [4,13]. There are two output signals from the PMT of the 2" x 2" $LaBr_3$:Ce detectors. The first is the timing signal also referred to as the fast channel stemming from the anode pulse. The second is the energy signal or the channel from the dynode pulse. The source to detector geometry was such that the point source is placed 240 mm equidistant from each detector as shown in Fig. 1. These measurements give an insight into the performance of detectors and what are the possible limitations.

The electronics of the detectors are such that they are digital and not analogue. The DPP module is connected to the 500 MHz card.

2.1. Detector electronics set up

The incoming signals are digitized and three digital filters are applied, namely; a digital constant fraction (CFD) filter, a fast and a slow trapezoidal filter. The Constant Fraction Discriminator (CFD) provides a timing signal which is related to the time of occurrence of the gamma-ray detection. The CFD algorithm, implemented in the signal processing field programmable gate array (FPGA), is unique for 500 MHz. This is because the ADC data arriving into the FPGA is initially delayed and the FPGA then locates the CFD trigger point between two adjacent 2 ns ADC samples via the weighing method. The following equation describes how the CFD algorithm is implemented [14]:

$$CFD(k) = w.\left(\sum_{i=k}^{k+L} a(i) - \sum_{i=k-B}^{k-B+L} a(i)\right) - \left(\sum_{i=k-D}^{k-D+L} a(i) - \sum_{i=k-D-B}^{k-D-B+L} a(i)\right) \quad (1)$$

Table 1
Typical parameters used for the slow and fast signal that were adjusted to achieve the best energy resolution. These values may vary slightly from detector to detector.

Parameter	Slow signal (μs)	Fast signal (μs)
Fast Risetime	0.10	0.02
Fast Flat Top	0.10	0.01
Energy Risetime	0.50	0.20
Energy Flat Top	0.50	0.10
Peak sample	0.98	0.24
Peak separation	1.00	0.50
Decay constant	34.93	0.03
CFD Delay	0.01	0.01

where $a(i)$ is the ADC trace data, k is the index representing the ADC tick (2 ns). The parameters w, B, D and L are set as $w = 1$, $B = 5$, $D = 5$ and $L = 1$.

The CFD delay and fraction are thus fixed to optimize its response. The zero crossing point is found by first building sums of ADC samples and then calculating the difference between delayed and non-delayed sums. The FPGA implements pulse detection, triggering, discrimination, pileup inspection and a trapezoidal energy filter digitally. Waveforms of each event may be customized by user defined functions such as trigger threshold, filter rise and flat top time, etc. The Digital Signal Processor (DSP) processes validated events and those events that are not validated are eliminated with zero dead time. The DSP reads out the energy filter from the FPGA and computes the pulse height and performs other tasks such as constant fraction timing and rise time calculation. It communicates with the host computer via an interface through the direct memory access (DMA) channel. A more thorough and detailed procedure is available in Ref. [15]. The DSP,s on board memory allows it to increment and store spectra. The data is collected using the iThemba LABS Digital Data Acquisition System [16].

Since the DPP module used has sixteen channels, the first eight were allocated the slow signal while the last eight were allocated the fast signal. To explore and optimize the performance of the $LaBr_3$:Ce detectors incorporated to the DPP module several radioactive sources were used.

2.2. Energy resolution and efficiency

The resolution at energy E is a ratio of the full width at half-maximum (FWHM) and the full energy peak (FEP).

The user defined functions mentioned in Section 2.1 were optimized so as to achieve the best possible energy resolution, with the typical values shown in Table 1. Parameters such as the energy risetime have a direct bearing on the energy resolution and need to be adjusted so as to produce the optimum energy resolution. Fig. 2 shows the singles spectrum of ^{60}Co radioactive source generated from one of the $LaBr_3$:Ce detectors.

The well known 1173 keV and 1332 keV peaks, from the ^{60}Co decay, can been identified together with the 1436 keV peak, from ^{138}La, that is the result of the internal radioactivity of the $LaBr_3$:Ce detector and the 1460 keV peak from presence of ^{40}K is visible. The energy resolution value obtained for the detectors is between 4.2% and 5.3% at 662 keV. It is not known exactly why the energy resolution is poorer than what is expected, as several factors may be responsible including noise induced by electronics. Test measurements are ongoing to improve the energy resolution, which include optimizing the operational voltage, since the less than expected energy resolution may also be due to a lowly optimized operational voltage. Furthermore, $LaBr_3$:Ce detectors are known to have a 2.1% energy resolution at 1332 keV [17].

The total peak efficiency of the array of eight 2" x 2" $LaBr_3$:Ce detectors was found to be 0.28% ± 0.0013 at 1332 keV with the same geometry as described above.

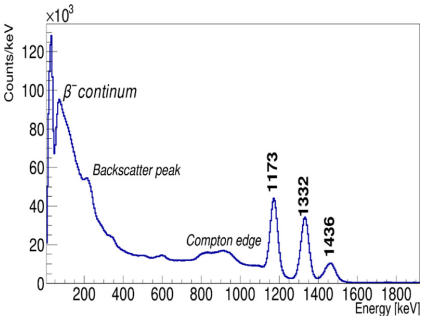

Fig. 2. The ^{60}Co singles spectrum obtained from one of the 2" x 2" $LaBr_3$:Ce detectors. The peak at 1436 keV, from ^{138}La, is due to the internal radioactivity of the $LaBr_3$:Ce detector.

Table 2
Table of the measured coincidence resolving time (CRT) obtained by varying the detector pairs in order to determine the contribution from each detector.

Detector	CRT [ps]
A11019	383.3(2.7)
A11020	318.3(3.4)
A11021	328.9(3.1)
A11022	364.1(2.8)
A11023	378.5(3.0)
A11024	379.7(3.0)
A11025	412.4(2.6)
A11026	407.9(2.6)

2.3. Time resolution

The limit of lifetimes that can be measured directly by $LaBr_3$:Ce detectors is determined by the time resolution of the detectors. To obtain the time resolution of a single detector, coincidence timing measurements of detector pairs were used for the prompt 1172–1332 keV cascade from the ^{60}Co decay. The timing resolution for the individual detectors ranged between 320 ps FWHM and 409 ps FWHM. The time resolution of the array was also measured by measuring positron annihilation γ-rays from a ^{22}Na source and gating on the 511 keV peak in the pair of detectors along the same axis. The coincidence resolving time (CRT), reported in Table 2, is extracted from the width peak for each pair.

Statistical amplitude variations affect the CFD time jitter rather than noise induced by electronics [18]. The threshold voltage, delayed time and zero crossing are CFD parameters that can be easily adjusted to produce a reliable and trustworthy results. The threshold prevents triggering from the noise by ignoring signals below the said threshold. Other factors that affect time resolution include detector size and operational voltage. A more detailed discussion may be found in [19].

3. Lifetimes of radioactive sources

Using the fast-timing technique, the transition that populates an excited state may be designated as the *start* and the one that depopulates it, may be designated *stop*. It is paramount that the energies are well resolved to clearly distinguish the transitions populating or depopulating an excited state. The quality of the measurement depends on this important ability.

The ^{67}Ga source was produced at iThemba LABS, it has a half-life of 3.26 days, decays through 100% electron capture to ^{67}Zn.

In this decay process, the 184.6 keV level decays to the ground state via the $(3/2^-) \rightarrow (5/2^-)$ transition. In this work, the lifetime of the $(3/2^-)$ state at 184.6 keV level was measured. This was obtained by measuring the time difference between two signals of the $LaBr_3$:Ce detectors. The first signal which defines the *start*, is given by the 209 keV gamma ray populating the level and the second signal, which is the *stop*, by the 184.6 keV gamma ray depopulating it.

Table 3
Table of values for the half-life of the first excited state 2^+ of ^{152}Sm from previous publications.

Author and reference	Half-life (ns)
M. Birk *et al.* [23].	1.45(6)
D. Ashery *et al.* [24]	1.41(6)
P. J. Wolfe and R. P. Scharenberg [25]	1.46(5)
F. W. Richter *et al.* [26] .	1.44(3)
A. Hubner [27]	1.43(4)
W. Karle *et al* [28]	1.398(6)
C. C. Dey *et al* [29]	11.40(2)
M. R. El-Asser *et al* [30].	1.35(5)
H. W. Kugel *et al.*[31]	1.41(4)
R. E. McAdams and E. N. Hatch [32]	1.36(6)
D. B. Fossan and B. Herskind [33]	1.37(4)
A. W. Sunyar [34]	1.40(10)
M. Hellstrom *et al* [35].	1.471(35)
Present work	**1.394 (9)**
M. J. Martin [36]	1.403(11)

The time spectrum obtained is shown in Fig. 3(a) through which the lifetime of the $(3/2^-) \rightarrow (5/2^-)$ transition was calculated. The slope method was employed to obtain the lifetime of this transition and other transitions that have much longer lifetimes than the system's time resolution. In this method no background subtraction was applied, since the time contribution of the background usually affects the prompt distribution. By taking a fit far from the prompt region, the background time component can be avoided. The lifetime of this transition was calculated to be $T_{1/2}$ = 1.090(7) ns. Lieder et al. [21] states this half-life to be $T_{1/2}$ = 1.01(5) ns. While Engel et al. [22] asserts it to be $T_{1/2}$ = 1.026(14) ns.

The current analysis studied the ^{152}Eu radioactive source, decays by 72.08% to ^{152}Sm via electron capture. The half-life of the first excited state (2^+) of ^{152}Sm has a reported value of 1.403(11) ns [20]. Setting the *start* and *stop* gates on transitions that populate and depopulate the 2^+ state we found the half-life to be $T_{1/2}$ = 1.394(9) ns. Various measurements, see Table 3, were performed to determine the half-life of the first excited state 2^+ of ^{152}Sm. The adopted value in the ENSDF evaluated data sheet is $T_{1/2}$ = 1.403(11) ns.

Another radioactive source studied in this work is ^{133}Ba, it decays to ^{133}Cs through 100% electron capture and has a half-life of 10.551 years. The $(5/2^+)$ state of ^{133}Cs is adopted as $T_{1/2}$ = 6.283(14) ns according to the ENSDF evaluated data sheet. To obtain the lifetime of this state, two detectors were used with a gate set on the 356 keV transition that populates the state and the 81 keV that depopulates it. The present work reports the half-life of this state to be $T_{1/2}$ = 6.217(12) ns (Table 4).

3.1. Time walk characteristics

Essential to obtaining accurate lifetimes of excited nuclear states is the ability to employ a walk-free signal. The inherent variation in the delay of the discriminator results in time walk and may affect the quality of the signal. For scintillator detectors, it is not good practice to ignore the time walk as it may lead to adverse effects on the time resolution of a fast-timing array. Various methods may be used to correct for the time walk of a detector [6,54–56], to optimize the input signal. In a real γ-γ fast-timing set-up, the detector dependent time-walk difference is visible although it may be compensated in the CFD. Applying a higher PMT operation voltage can reduce the time-walk non-linearity yet this can drive the energy response of the PMT into non-linearity [57].

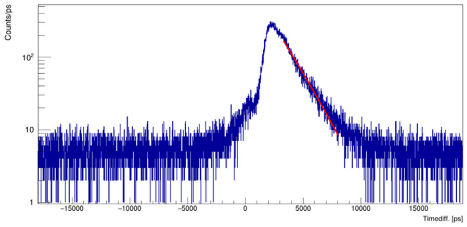

(a)

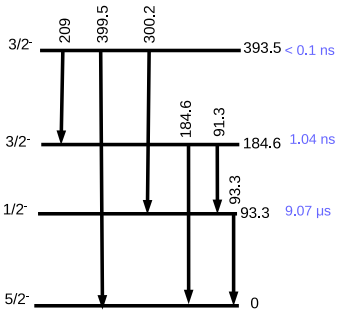

(b)

Fig. 3. (a) The time difference spectrum between two detectors fitted with exponential fit to determine the half-life of the 184.6.6 keV level of ^{67}Zn populated through the decay of the ^{67}Ga radioactive source. INSERT: The time spectrum on logarithmic scale. (b) The partial level scheme of ^{67}Zn showing the 209 keV transition populating the 184.6.6 keV level [20].

Table 4
List of published values of the half-life for the first excited state in ^{133}Cs.

Author and reference	Half-life (ns)
H. Mach *et al.* [37].	6.321(35)
E. Bodenstedt *et al.* [38]	6.31(5)
W. Flauger and H. Schneider [39]	6.30(15)
D. Bloess *et al* [40] .	6.25(5)
B. Olsen and L. Bostrom [41]	6.16(7)
F. W. Richter and J. Schutt [42]	6.25(5)
F. A. Akilov *et al* [43]	6.30(7)
A. Sakata *et al* [44] .	6.26(17)
K. G. Valivaara *et al.* [45]	6.27(4)
P.D. Bond *et al* [46]	6.28(14)
D.K. Gupta and G.N. Rao [47]	6.36(3)
D. Mouchel and H.H. Hansen [48]	6.23(3)
R. L. Graham and R. E. Bell [49]	6.0(4)
P. Thieberger [50]	6.25(10)
J.S. Geiger *et al* [51]	6.3(3)
I.M. Govil *et al* [52]	6.08(4)
D. Bloess and F. Munnich [40]	6.25(5)
Present work	**6.217(12)**
Yu. Khazov *et al* [53]	6.283(14)

For sub-nanosecond fast-timing measurements, it is necessary to establish the dependence of the time response as a function of energy. Moreover, when measuring lifetimes in the sub-nanosecond range, the centroid shift method may be employed. Characteristics of the energy as a function of the centroid position's prompt time distribution describes the time walk characteristics. The interplay of the shape of the detector output pulse and the timing principle result in the prompt response function [57].

A ^{60}Co radioactive source was used in this work to investigate the effects of the time walk. Fig. 4(a) illustrates that time walk characteristics when the *start* detector is gated on the 1173 keV and 334 keV. In order to obtain the centroid position over a wide range, 10 keV wide gates, in increments of 20 keV, were gated on the *stop* detector. The 1173 keV transition populates the 1332 keV level in ^{60}Ni following the β-decay ^{60}Co radioactive source. For comparison, a gate is set on the 344 keV Compton background as well and is an essential reference energy describing the prompt response function as elaborated by Régis et al. [58]. Similarly, gating the *stop* detector 1173 keV and 334 keV the fits as represented in Fig. 4(b) were obtained.

Below 300 keV a delayed structure, which may be a result of Compton scattered events, is observed. The 1173 keV gated centroids show an invariable continuity up to about 1200 keV and from then a structure is visible, possibly emanating from Compton scattered events.

N. Marginean et al. [6] used a second order polynomial to correct for the time walk, resulting in an optimum time resolution. The fitted

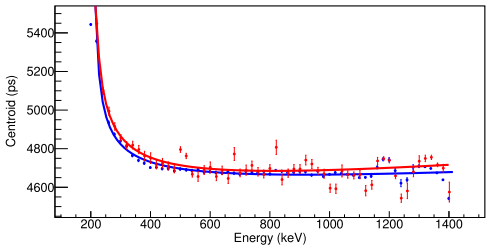

(a)

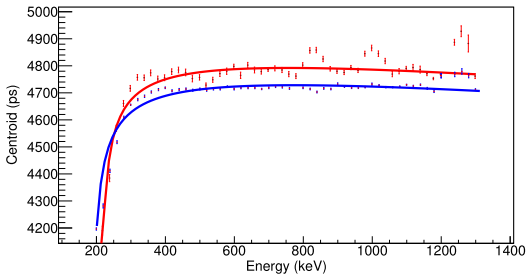

(b)

Fig. 4. (a) The energy dependency of the centroid position of the prompt time distribution obtained from gating the *start* detector on the 334 keV Compton background (in red) and 1173 keV full energy peak (in blue) transitions of the ^{60}Co source. (b) The gate is now set on the *stop* detector on the same transitions. The fitted data points in red are for gates set on the 344 keV and those in blue are for the 1173 keV.

centroids shown in Fig. 4, were fitted using:

$$C(E_\gamma) = \frac{a}{\sqrt{b + E_\gamma}} + cE_\gamma + d \tag{2}$$

4. In - beam experiment

To evaluate the performance of the 2" x 2" $LaBr_3$:Ce detectors when exposed to in-beam experimental environment, an experiment was conducted in which six 2" x 2" $LaBr_3$:Ce detectors were coupled to the AFRODITE array with eight Compton-suppressed clover detectors. Two additional large volume 3" x 8" $LaBr_3$:Ce detectors were also used.

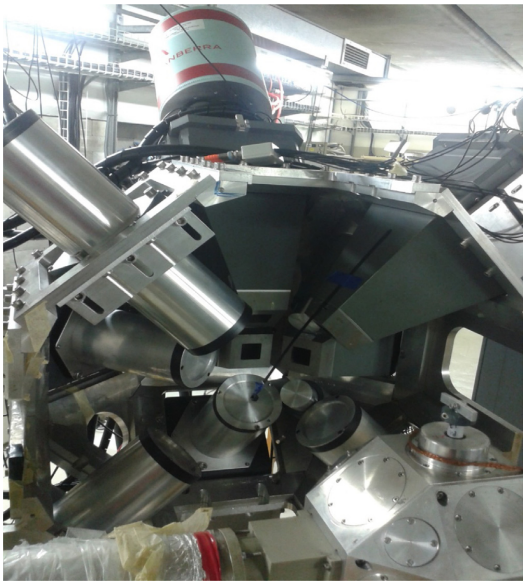

Fig. 5. The AFRODITE array consisting of HPGe clover detectors with BGO shields, large volume 3" by 8" $LaBr_3$:Ce detectors and medium sized 2" by 2" $LaBr_3$:Ce detectors.

The experimental set-up is shown in Fig. 5. High detector efficiency and excellent timing properties are obtained from large and small $LaBr_3$:Ce detectors respectively, whereas the clovers detectors offers superior energy resolution. Two of the 2" x 2" $LaBr_3$:Ce detectors were placed at an angle of 45° with respect to the beam line axis and the other four were placed at an angle 90°.

A micron semiconductor S2 type, with 48 rings and 16 sectors, was used in this work to build a particle identification telescope that consists of a thin energy loss stage in transmission geometry followed by a much thicker residual energy detector in which the particles are *stopped*. This particle dE-E telescope, used to select a desired reaction channel, was inserted inside the target chamber. The thickness of the dE detector used was 309 μm and the thickness of the E was 1041 μm. The mass and the charge of the particle both influence the energy loss per unit length.

The signals from HPGe detectors and particle telescope processed by the 100 MHz XIA digital acquisition card. In this work, results for the ^{45}Sc(p,d)^{44}Sc and ^{45}Sc(p, α)^{42}Ca reaction channels, with beam energy was 27 MeV, are reported. Two crates accommodate nuclear electronics in standard modules were used in this experiment. The first crate was fully occupied by the particle telescope and the HPGe detectors which were all incorporated into the 100 MHz XIA digital acquisition card. The second crate was used to accommodate the $LaBr_3$ detectors which were incorporated 500 MHz XIA digital acquisition card.

An arbitrary shift, between the $LaBr_3$ detector channels, in the recorded timestamp (in multiples of 2 ns in the 500 MHz card) was observed to occur whenever the DPP was restarted resulting in signals to become arbitrarily shifted in time, therefore a correction in the software was implemented. This shift is due to unsynchronized signals and in instances where DPP was left uninterrupted no shift was observed. To correct for this effect, the centroids of the time distributions were determined in order to observe how the signals were shifted during the *start* and *stop* process.

Table 5
Energy resolution $LaBr_3$:Ce detectors at 1.3 MeV obtained from the radioactive source ^{60}Co. The detector numbers recorded here are as per the label on the detectors.

Detector Number	Energy resolution at 1.3 MeV
2" x 2" $LaBr_3$:Ce 2	3.19%
2" x 2" $LaBr_3$:Ce 4	3.22%
2" x 2" $LaBr_3$:Ce 5	3.26%
2" x 2" $LaBr_3$:Ce 6	3.73%
2" x 2" $LaBr_3$:Ce 7	2.48%
2" x 2" $LaBr_3$:Ce 8	3.26%
3" x 8" $LaBr_3$:Ce 3.1	2.74%

4.1. Characterization of $LaBr_3$:Ce detectors for the in-beam set-up

The $LaBr_3$:Ce detectors were calibrated using a third order polynomial of the form:

$$E = ax^3 + bx^2 + cx + d \tag{3}$$

where a, b, c, d are the gain matching coefficients. E is the energy and x is the channel number of the original spectrum. These peaks were fitted and the relevant peak centroids and their uncertainties were taken into account so that each point has an associated weight. A correction as a result of a shift between detector channels was done [19]. The energy-independent centroids give a constant shift_{ij} values that were arranged in a matrix form, $i \times j$, for each time the data acquisition system was stopped between runs. The matrix elements $i \times j$ were arranged as 6×6 elements such that $\text{shift}_{i=j} = 0$ and $\text{shift}_{ij} = -\text{shift}_{ji}$.

The energy resolution obtained from the ^{60}Co calibration source is shown in Table 5.

Several factors influence the efficiency of detectors including the solid angle and the properties of a detector crystal. The high density and high atomic number of $LaBr_3$:Ce detectors result in higher detection efficiency. The total photopeak efficiency for the 2" x 2" $LaBr_3$:Ce detectors for the in-beam set up was obtained as $0.84\% \pm 0.0010$. The large volume 3" x 8" $LaBr_3$:Ce detectors were not the focus of this study. They are, however, part of the African $LaBr_3$:Ce Array (ALBA), at iThemba LABS, a detailed characterization of these detectors is found in Ref. [59].

4.2. The Prompt Response Difference (PRD) curve

To extract sub-nanosecond lifetimes, it is important to calibrate the zero-time response of the fast timing set-up. This involves a detailed and thorough process of determining the energy dependent centroid position of simultaneously occurring events (prompt events) of the prompt response function. Through this process, the timing characteristics describing the set-up is possible, which known as the "prompt response difference" (PRD) curve [60]. The PRD curve was determined using the ^{152}Eu radioactive source which decays to ^{152}Gd through β^- decay mode. The nucleus ^{152}Gd emits several gamma-ray transitions that are in coincidence with each other and have known picosecond lifetimes. This enables a reference energy gate to be selected and keep it constant while varying other gates that are in coincidence with the chosen reference energy gate. In this work, the 344 keV state was chosen as reference energy gate since there are seven gamma-ray transitions that are in coincidence with it. A measured centroid difference (which is the difference of the centroid position between the *start* and *stop* time distributions) is obtained which is then corrected by twice the known lifetime of the state, 2τ, to obtain each data point, which is then plotted as function of energy, yielding the PRD curve. The ^{152}Eu source also decays to ^{152}Sm through electron capture. The 244 keV transition of ^{152}Sm is populated by several transitions, and therefore is useful as a reference energy. The PRD for energy reference at 244 keV was obtained. The two PRD curves can be shifted in parallel

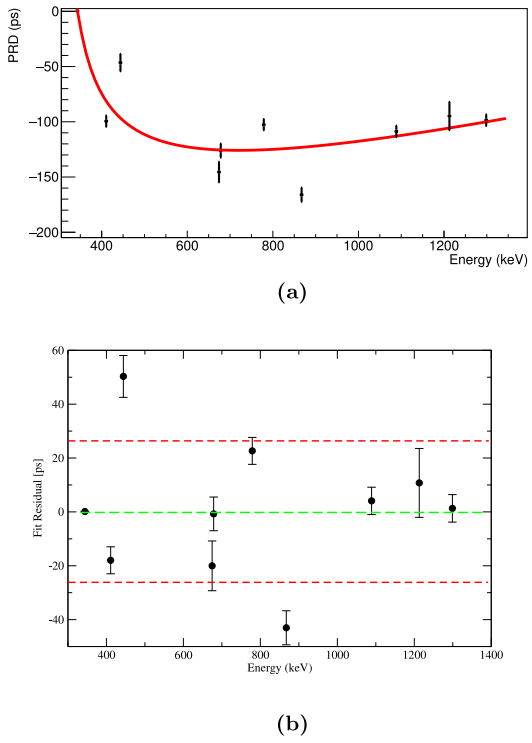

Fig. 6. (a) The PRD curve obtained after the overlapping of the two curves obtained with reference energies 344 keV and 244 keV is done. (b) The fit residual showing the data point deviation to the fit. The red dashed lines correspond to 26 ps, which is equivalent to 1σ.

so that one overlaps onto another thus making a single PRD curve see Fig. 6(a). The data points of the PRD curve are then fitted using, [60]

$$PRD(E_\gamma) = \frac{a}{\sqrt{b + E_\gamma}} + cE_\gamma + d \tag{4}$$

where a, b, c and d are free fit parameters.

No active shielding was placed around the $LaBr_3$:Ce detectors. Deviations from the smooth monotonic curve are possibly induced by Compton scattered events. Though both gates were set on full energy events to obtain the PRD curve, exposure to Compton events do contaminate the timing information of a $\gamma - \gamma$ fast-timing set-up. Compton events may result in an artificial delay in the timing information. The presence of an artificial delay in the time distributions is related to the time-of-flight of the scattered γ-ray [61].

4.3. The ^{44}Sc nucleus

The ^{44}Sc nucleus is an odd–odd nucleus with one valence proton and three valence neutrons outside the doubly magic ^{40}Ca nucleus. The ^{44}Sc nucleus has a dynamic range of excited nuclear states which makes it possible to put to test the performance of the 2" x 2" $LaBr_3$:Ce detectors.

4.3.1. The 2^- state

Instead of a $LaBr_3$:Ce detector, a reference timing signal can be synchronized with the radio-frequency (RF) of the pulsed beam to form a *start* signal and the *stop* can be provided by one of the 2" x 2" $LaBr_3$:Ce detectors. Using the RF as a reference signal has an added

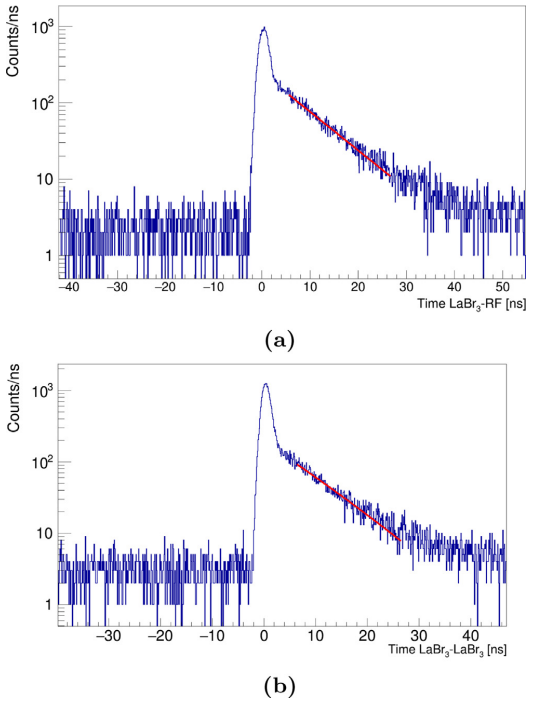

Fig. 7. (a)Time spectrum obtained by the gating the radio-frequency and a $LaBr_3$:Ce detector used to measure the half-life the 234.7 keV level. The fitted region represents events of the full energy peak. (b) Time spectrum obtained when two $LaBr_3$:Ce detectors are used, for the 234.7 keV level, in which one is a *start* and the other is *stop*.

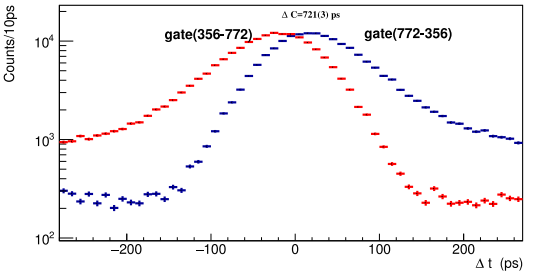

Fig. 8. Time distribution spectra for the 772 → 356 $keV\gamma$-γ cascade from which the ΔC value for the 429 keV level was obtained.

advantage of yielding more statistics and better results. In this work, the RF signal was used as a reference signal and also a $LaBr_3$:Ce detector as a reference signal allowing the results to be compared between RF-$LaBr_3$ and $LaBr_3$-$LaBr_3$ measurements.

The half-life of the 234.7 keV level was measured and compared to the value reported in literature. The *start* gate was set on the feeding 396 keV, $4^- \rightarrow 2^-$, transition and a *stop* gate set on the $2^- \rightarrow 0$ transition. When the RF was used as a reference signal the lifetime obtained for the excited 2^- state, at 234.7 keV level is $T_{1/2}$ = 6.160(76) ns. The time distribution spectrum from which this half-life was measured is shown in Fig. 7(a). The half-life for the same state when using $LaBr_3$-$LaBr_3$ measurements is $T_{1/2}$ = 5.93(41) ns, with the time distribution shown in Fig. 7(b). In both time spectra two

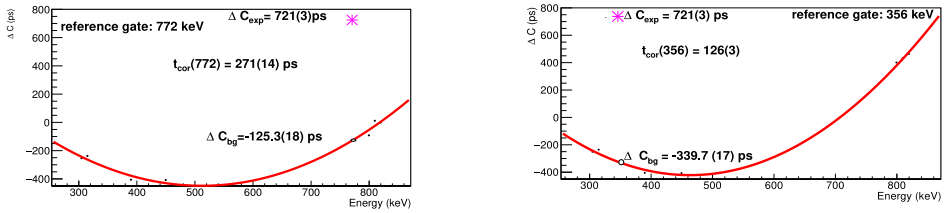

Fig. 9. (a) The centroid difference as a function of energy depicting background timing-analysis with the reference gate set at 772 keV with the background gates set around the regions of FEPE at 356 keV and 772 keV. The data points are fitted using a second order polynomial. (b) The centroid difference as a function of energy depicting background timing-analysis with the reference gate set at 356 keV with the background gates set around the regions of FEPE at 356 keV and 772 keV. The data points are fitted using a second order polynomial.

components are visible; The large fast component is due to the Compton background and the slow component due to full energy peak detection. It is this slow component that the half-life of the excited 2^- state was calculated using the slope method. The value obtained in this work is $T_{1/2} = 6.160(76)$ ns while the value reported ENSDF evaluated data sheet is $T_{1/2} = 6.12(23)$ ns [20]. The results of the 2^- state at 234.7 keV level and other states of ^{44}Sc are presented in Table 6

Contributions from the large fast component may falsify lifetime measurements, however, these contributions may be avoided by fitting the slope outside the region of the Compton background. Since the background is distributed uniformly it may be determined and catered for prior the fit, which was done for the fits obtained for Figs. 7(a) and 7(b).

4.3.2. The 3^- state

By virtue of this state being a much more short lived state, in the sub-nanosecond region, the Generalized Centroid Shift Method was employed to measure the lifetime of this state and all other sub-nanosecond states. The γ-γ cascade used to measure the lifetime of this state is $5^- \rightarrow 3^-$ and $3^- \rightarrow 1^-$. The populating and depopulating gamma energies are 772.5 keV and 356.92 keV respectively.

The centroid difference value of ΔC = 721(3) ps was obtained as shown in Fig. 8 and the PRD correction factor for the combination 772.5 → 356.92 keV is given by PRD(772–356 keV) = −99(26) ps.

In this analysis to correct for the background, the Compton background correction method was employed [58]. Another background correction through analytical means has been developed by Gamba et al. [62]. In order to compute the energy-dependent centroid difference, ΔC_{bg}, gates were set around well defined background regions for both the (full energy peak events) FEPE in the (772 → 356 keV) cascade. The reference energies are the FEPE whereas the background regions are varied. Fig. 9 shows both background-timing analyses for the two experimental peak-background components fitted with a second order polynomial. The background gates were set at the same width. The $LaBr_3$:Ce and HPGe gated coincidence spectra are shown in Fig. 10. The HPGe coincidence spectrum was used to select the background gate because of its excellent energy resolution. The lifetime of the excited 3^- state is then calculated as follows, [63]:

$$\tau = \frac{\Delta C + t_{av} - PRD}{2\times} \tag{5}$$

where t_{av} is the total time correction obtained from the weighted average of two separately measured time correction terms from the feeder and the decay transitions of the $\gamma - \gamma$ cascade. The half-life of this state obtained after background correction is recorded in Table 6.

4.3.3. The 6^- state

The 6^- state at 2210.5 keV level has no known lifetime recorded in literature. In this work, the lifetime of the 6^- state at 2210.5 keV level was measured. The transition that populates this state is the $7^- \rightarrow 6^-$ and it is associated with 396.2 keV γ ray. The 2210.5 keV level is depopulated by the $6^- \rightarrow 5^-$ which is associated with the 1013 keV γ ray. The centroid difference ΔC = 316(2) ps, as illustrated by Fig. 11. The PRD correction factor for the (396 → 1013 keV) cascade is PRD(396–1013 keV) = -45(26) ps. The half-life of this state obtained after background correction, using the similar approach employed for the 3^- state, is given in Table 6.

4.3.4. The 7^- state

The 7^- state at 2606.7 keV level has no known lifetime recorded in literature. This work reports the lifetime of this state. The 2606.7 keV is populated by the 382 keV γ ray level through the $8^- \rightarrow 7^-$ transition. The depopulating γ ray is 1409 keV through the $7^- \rightarrow 5^-$ transition. The centroid difference is ΔC =344(5) ps, as illustrated by Fig. 12.

The PRD correction factor for the (382 → 1409 keV) cascade is PRD(382–1409 keV) = -33(26) ps. The half-life of this state obtained after background correction, using the similar approach employed for the 3^- state, is given in Table 6.

4.3.5. The 8^- state

The lifetime of the 8^- state at 3364.1 keV level was measured in this work and it has no known literature value. The 465 keV γ ray populates this level and it is the $9^- \rightarrow 8^-$ transition. It is also depopulated by a $8^- \rightarrow 7^-$ transition associated with the 757 keV γ ray. The centroid difference is ΔC = 292(3) ps, as illustrated by Fig. 13. The PRD correction factor for the (465 → 757 keV) cascade is PRD(465–757 keV) = -22(26) ps. The half-life of this state obtained after background correction, using the similar approach employed for the 3^- state, is given in Table 6.

4.4. The ^{42}Ca nucleus

The ^{42}Ca nucleus has only two valence neutrons outside the doubly magic ^{40}Ca nucleus. The nucleus ^{42}Ca was populated through the ^{45}Sc(p, α)^{42}Ca direct reaction.

4.4.1. The second 0^+ state

The first excited 0^+_2 state of ^{42}Ca is found at 1837.3 keV energy level and has a known half-life of $T_{1/2}$ = 387(6) ps. This state is populated by a $2^+ \rightarrow 0^+$ associated with the 587 keV gamma ray. It is depopulated by an $0^+ \rightarrow 2^+$ transition associated with the 312 keV gamma ray. Fig. 14 shows the delayed and anti-delayed time distributions from which the centroid difference was determined. The Compton background correction method was employed to correct for the background and the background-timing analyses spectra are shown in Fig. 15. The PRD correction factor for the (587 → 312) cascade is PRD(587–312 keV) = -323(26) ps. The half-life obtained for this state and other states of ^{42}Ca are compared with previous measurements in Table 7.

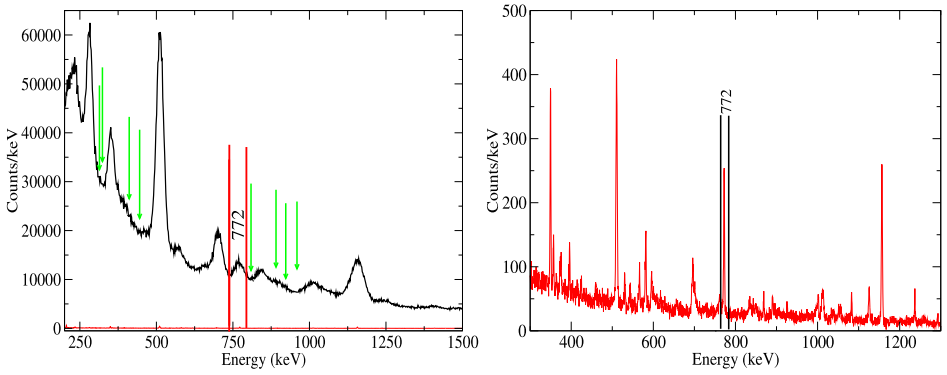

Fig. 10. (a) The γ-γ coincidence spectrum gated on the 356 keV. The full energy peak in coincidence with the 356 keV peak, used to obtain the lifetime of the excited 3^- state, is the 772 keV energy. The arrows mark the regions where the background gates around the full energy peaks were set. The black energy spectrum is the $LaBr_3$:Ce coincidence spectrum and the red energy spectrum is HPGe coincidence spectrum. (b) The HPGe gated spectrum clearly showing the 772 keV γ ray energy that is in coincidence 356 keV γ ray energy.

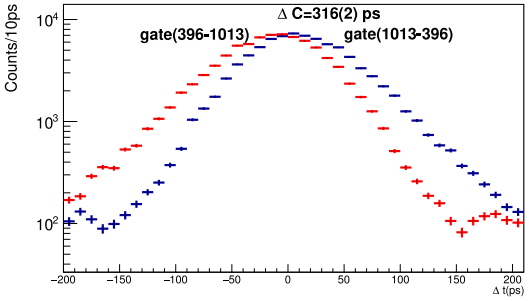

Fig. 11. Time distribution spectra for the 396 → 1013 $\gamma - \gamma$ cascade from which the ΔC value for the 2210.5 keV level was obtained.

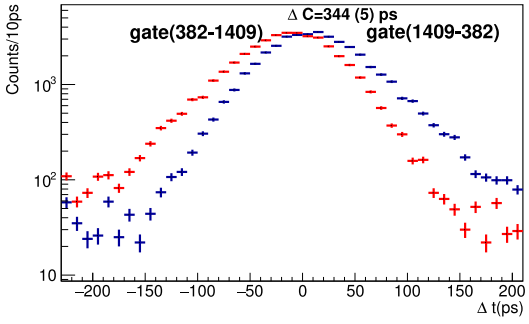

Fig. 12. Time distribution spectra for the 382 → 1409 $\gamma - \gamma$ cascade from which the ΔC value for the 2606.7 keV level was obtained.

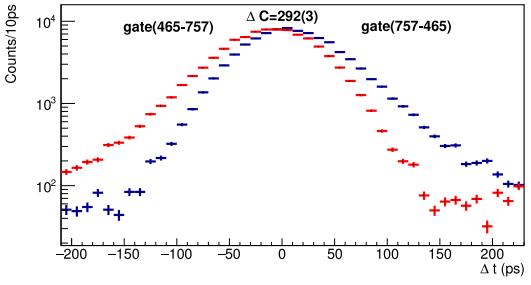

Fig. 13. Time distribution spectra for the 465 → 757 $\gamma - \gamma$ cascade from which the ΔC value for the 3364.1 keV level was obtained.

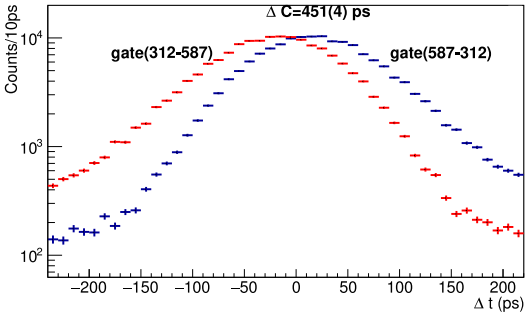

Fig. 14. Time distribution spectra for the 587 → 312 $keV\gamma$-γ cascade from which the ΔC value for the first excited 0_2^+ state of ^{42}Ca was obtained.

5. Conclusion

Eight 2" x 2" $LaBr_3$:Ce detectors used in conjunction with the 16 channel all-digital waveform 500 MHz acquisition card, PIXIE-16 were commissioned at iThemba Laboratory for Accelerator Based Sciences. Known lifetimes for ^{44}Sc and ^{42}Ca were extracted with new lifetimes for ^{44}Sc obtained. The results presented here prove that 2" x 2" $LaBr_3$:Ce detectors are a formidable tool for nuclear spectroscopy and in particular they are much useful for lifetime measurements. In this work we were able to obtain lifetimes without active shielding. Improved quality of results may be obtained in future experiments through active shielding, since this minimizes Compton background.

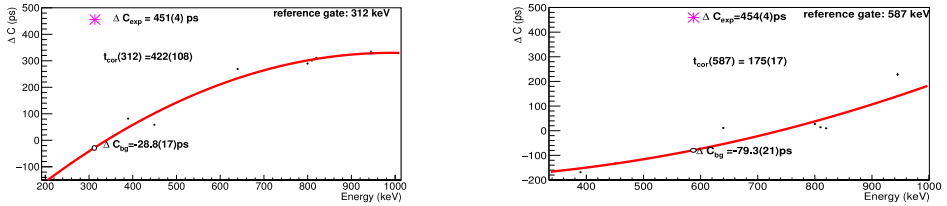

Fig. 15. (a) The centroid difference as a function of energy depicting background timing-analysis with the reference gate set at 312 keV with the background gates set around the regions of FEPE at 312 keV and 587 keV. The data points are fitted using a second order polynomial. (b) The centroid difference as a function of energy depicting background timing-analysis with the reference gate set at 587 keV with the background gates set around the regions of FEPE at 312 keV and 587 keV. The data points are fitted using a second order polynomial.

Table 6
Experimentally obtained half-lives that have been published for different states of ^{44}Sc. The values obtained in the current work are highlighted in bold. The sub-nanosecond lifetimes are background corrected, via the Compton background correction are indicated by the subscript CB.

Energy level (keV)	J^π	Method	Reference	Half-life
234.7	2^-	Recoil Distance	[64]	12.7 (22)ns
234.7	2^-	Delayed coincidence	[65]	6.12 (23)ns
234.7	2^-	ENSDF Evaluation	Adopted ENSDFvalue [20]	6.12 (23)ns
234.7	2^-	Fast-Timing (RF-$LaBr_3$)	Present work	**6.160 (76)ns**
349.9	4^+	Recoil Distance	[64]	3.12 (28)ns
349.9	4^+	Recoil Distance	[66]	3.1 (3)ns
349.9	4^+	ENSDF Evaluation	Adopted ENSDFvalue [20]	3.12 (19)ns
349.9	4^+	Fast-Timing (RF-$LaBr_3$)	Present work	**3.067 (14)ns**
349.9	4^+	Fast-Timing ($LaBr_3$-$LaBr_3$)	Present work	**2.499 (15)ns**
631	4^-	Recoil Distance	[67]	381 (55)ps
631	4^-	Recoil Distance	[64]	411 (30)ps
631	4^-	ENSDF Evaluation	Adopted ENSDFvalue [20]	404 (30)ps
631	4^-	Fast-Timing (GCD_{CB})	Present work	**336 (15)ps**
428.8	3^-	Recoil Distance	[66]	380 (40)ps
428.8	3^-	Recoil Distance	[64]	378 (42)ps
428.8	3^-	ENSDF Evaluation	Adopted ENSDFvalue [20]	378 (42)ps
428.8	3^-	Fast-Timing (GCD_{CB})	Present work	**364 (10)ps**
2210.5	6^-	Fast-Timing (GCD_{CB})	Present work	**162 (9)ps**
2606.7	7^-	Fast-Timing (GCD_{CB})	Present work	**180 (10)ps**
3364.1	8^-	Fast-Timing (GCD_{CB})	Present work	**164 (12)ps**

Table 7
Experimentally obtained half-lives that have been published for different states of ^{42}Ca. The values obtained in the current work are highlighted in bold. The sub-nanosecond lifetimes are background corrected, those that are corrected via the Compton background correction are indicated by the subscript CB.

Energy level (keV)	J^π	Method	Reference	Half-life
3189.3	6^+	Doppler Shift Attenuation	[68]	5.30 (16)ns
3189.3	6^+	Delayed Coincidence Techniques	[69]	3.7 (5)ns
3189.3	6^+	Doppler Shift Attenuation	[70]	5.3 (3)ns
3189.3	6^+	Delayed Coincidence Techniques	[71]	5.52 (15)ns
3189.3	6^+	ENSDF Evaluation	Adopted ENSDFvalue [20]	5.30 (16)ns
3189.3	6^+	ENSDF Evaluation	Adopted ENSDFvalue [20]	5.30 (16)ns
3189.3	6^+	Fast-Timing (RF-$LaBr_3$)	Present work	**4.91 (4)ns**
3189.3	6^+	Fast-Timing ($LaBr_3$-$LaBr_3$)	Present work	**4.29 (5)ns**
1837.3	0^+	Direct electronic timing	[72]	387(6)ps
1837.3	0^+	Delayed Coincidence Techniques	[73]	330 (20)ps
1837.3	0^+		[74]	420 (11)ps
1837.3	0^+	ENSDF Evaluation	Adopted ENSDFvalue [20]	387(6)ps
1837.3	0+	Fast-Timing (GCD_{CB})	Present work	**391 (17)ps**

CRediT authorship contribution statement

L. Msebi: Methodology, Formal analysis, Investigation, Writing – original draft, Review and editing. **V.W. Ingeberg:** Writing – original draft, Data curation. **P. Jones:** Conceptualization, Software, Supervision, Fund acquisition. **J.F. Sharpey-Schafer:** Supervision, Visualization, Conceptualization. **E.A. Lawrie:** Writing – original draft. **M. Wiedeking:** Project administration.

Declaration of competing interest

The authors declare that they have no known competing financial interests or personal relationships that could have appeared to influence the work reported in this paper.

Acknowledgment

We would like to acknowledge financial assistance and support from the National Research Foundation (NRF), South Africa under the following grants: (99037,90741,105207)

References

[1] P. Dorenbos, et al., IEEE Trans. Nucl. Sci. NS-51 3 (2004) 1289.
[2] I. Holl, E. Lorenz, G. Magera, IEEE Trans. Nucl. Sci. 35 no. 1 (1988) 105–109.
[3] B. Morosin, et al., J. Chem. Phys. 49 (1968) 2007.
[4] C.M. Rozsa, et al., Brilliance 380 Scintillator Perforamnce Summary, 2009.
[5] J.F. Sharpey-Schafer, Nucl. Phys. News. Int. 14 (2004) 5.
[6] N. Marginean, et al., Eur. Phys. J. A 46 (2010) 329.
[7] J.M. Régis, et al., Nucl. Instrum. Methods A 726 (2013) 191.
[8] T. Alharbi, et al., Phys. Rev. C 87 (2013) 014323.
[9] T. Alharbi, et al., Appl. Radiat. Isot. 70 (2012) 1337.
[10] P.J.R. Mason, et al., Phys. Rev. C 88 (2013) 044301.
[11] S. Kisyov, et al., J. Phys. Conf. Ser. 366 (2012) 012027.
[12] S. Kisyov, et al., Phys. Rev. C 84 (2011) 014324.
[13] Scintilation Products Technical Note available at, www.detectors.saint-gobain.com.
[14] XIA LLC. CFD Algorithm for 500 MHz Pixie-16, Tech. rep., XIA LLC., Sept. 2016..
[15] XIA LLC. PIXIE-16 User's Manual. Version 3.03, 2018, URL http://www.xia.com.
[16] iThemba LABS Annual Report 2013, URL https://tlabs.ac.za/wp-content/uploads/pdf/annual_reports/Annual_Report_2013_small.pdf.
[17] D. Weisshaar, et al., Nucl. Instrum. Methods A 594 (2008) 56.
[18] H. Spieler, IEEE Trans. Nucl. Sci. NS-29/3 (1982) 1142.
[19] L. Msebi, Lifetime Measurements of Excited Nuclei Through Modern Nuclear Spectroscopy (Ph.D. thesis), University of the Western Cape, 2021, in press.
[20] National Nuclear Data Center, URL http://www.nndc.bnl.gov/nudat2/chartNuc.jsp.
[21] R.M. Lieder, et al., Nuclear Phys. A 106 (2) (1967) 389.
[22] H. Engel, et al., Naturfosch 27a (19) 1368.
[23] M. Birk, et al., Phys. Rev. 116 (1959) 730–733.
[24] D. Ashery, et al., Nucl. Phys. 77.3 (1966) 650–656.
[25] P.J. Wolfe, R.P. Scharenberg, Phys. Rev. 160 (1967) 866–873.
[26] F.W. Richter, et al., Z. Phys. 213 (1938) 202.
[27] A. Hubner, Z. Phys. 183 (1965) 25.
[28] W. Karle, et al., Nucl. Instr. Methods A 271.3 (1998) 507–511.
[29] C.C. Dey, et al., Can. J. Phys. 70 (1992) 268.
[30] M.R. El-Asser, et al., Z. Naturfosch. 27a (1972) 1229.
[31] H.W. Kugel, et al., Phys. Rev. 165 (1968) 1352–1360.
[32] R.E. McAdams, E.N. Hatch, Nucl. Phys. 82.2 (1966) 372–384.
[33] D.B. Fossan, B. Herskind, Nucl. Phys. 40 (1963) 24–33.
[34] A.W. Sunyar, Phys. Rev. 98 (1955) 653–657.
[35] M. Hellstrom, et al., Phys. Rev. C43 (1991) 1462–1465.
[36] M.J. Martin, Nucl. Data Sheets 114.11 (2013) 1497–1847.
[37] H. Mach, et al., Nucl. Instrum. Meth. A (1989) 49–72.
[38] E. Bodenstedt, et al., Nucl. Phys. 11 (1959) 584–598.
[39] W. Flauger, H. Schneider, Atomkernenergie 8 (1963) 453.
[40] D. Bloess, et al., Z. Phys. 192 (1966) 358.
[41] B. Olsen, L. Bostrom, Nucl. Instrum. Methods 44 (1966) 65.
[42] F.W. Richter, J. Schutt, Z. Phys. 199 (1967) 422.
[43] F.A. Akilov, et al., Izv. Akad. Nauk SSSR Ser.Fiz. 32 (1968) 808.
[44] A. Sakata, et al., Himeji Kogyo Daigaku Kenkyu Hokoku No.22A (1969) 1.
[45] K.G. Valivaara, et al., Phys. Scr. 2 (1970) 19.
[46] P.D. Bond, et al., Nuclear Phys. A 163.2 (1971) 571–576.
[47] D.K. Gupta, G. Rao, Nuclear Phys. A 182.3 (1972) 1669–1672.
[48] D. Mouchel, H.H. Hansen, Int. J. Appl. Radiat. Isot. 34.8 (1991) 1201–1210.
[49] R.L. Graham, R.E. Bell, Can. J. Phys. 31.3 (1953) 377–392.
[50] P. Thieberger, Arkiv Fysik 22 (1962) 127.
[51] J.S. Geiger, et al., Nucl. Phys. 68.2 (1965) 3352–3368.
[52] I.M. Govil, et al., Nucl. Phys. 45 (1963) 60–64.
[53] Y. Khazov, Nucl. Data Sheets 112.4 (2011) 855–1113.
[54] G.J. Wozniak, et al., Nucl. Instrum. Methods 180 (1981) 509–510.
[55] E. Lamprou, et al., Characterization of TOF-petdetectors based on monolithic blocks and ASIC-readout, 2018, arxiv preprint arXiv:1806.08715.
[56] J. Du, IEEE Trans. Radiat. Plasma Med. Sci. 1 (5) (2017) 385–390, http://dx.doi.org/10.1109/TRPMS.2017.2726534.
[57] J.M. Régis, et al., Nucl. Instrum. Methods A 684 (2012) 36.
[58] J.M. Régis, et al., Nucl. Instrum. Methods A 622 (2010) 83–92.
[59] F. Azaiez, R. Nchodu, R. Nemutudi, M. Wiedeking, Nucl. Phys. News 30 (4) (2020) 5–11, http://dx.doi.org/10.1080/10619127.2020.1832807.
[60] J.M. Régis, Fast Timing with $LaBr_3$(Ce) Scintillators and the Mirror Symmetric Centroid Difference Method (Ph.D. thesis), Köln, 2011.
[61] H. Mach, et al., Nuclear Phys. A523 (1991) 197.
[62] E.R. Gamba, A.M. Bruce, M. Rudigier, Nucl. Instrum. Meth. A928 (2019) 93–103.
[63] J. Régis, et al., Nucl. Instrum. Methods A 955 (2020) 163258, http://dx.doi.org/10.1016/j.nima.2019.163258, URL http://www.sciencedirect.com/science/article/pii/S016890021931527X.
[64] G.D. Dracoulis, J.L. Durell, W. Gelletly, J. Phys. A: Math. Nucl. Gen. 6 (11) (1973) 1772–1799, http://dx.doi.org/10.1088/0305-4470/6/11/014.
[65] G.D. Dracoulis, G.S. Foote, M.G. Slocombe, The g-factor of the 235 keV state in44sc, J. Phys. A: Math. Nucl. Gen. 7 (18) (1974) 2289–2294, http://dx.doi.org/10.1088/0305-4470/7/18/009.
[66] J.J. Kolata, et al., Phys. Rev. C 10 (1974) 1663.
[67] A.R. Poletti, et al., Phys. Rev. C 13 (1976) 1180–1193, http://dx.doi.org/10.1103/PhysRevC.13.1180, URL https://link.aps.org/doi/10.1103/PhysRevC.13.1180.
[68] M. Marmor, S. Cochavi, D.B. Fossan, Phys. Rev. Lett. 25 (1970) 1033–1035, http://dx.doi.org/10.1103/PhysRevLett.25.1033, URL https://link.aps.org/doi/10.1103/PhysRevLett.25.1033.
[69] R. Hartmann, K.P. Lieb, H. Röpke, Nuclear Phys. A 123 (2) (1969) 437–448, http://dx.doi.org/10.1016/0375-9474(69)90512-0, URL http://www.sciencedirect.com/science/article/pii/0375947469905120.
[70] R. Hartmann, H. Grawe, Nuclear Phys. A 164 (1) (1971) 209–218, http://dx.doi.org/10.1016/0375-9474(71)90851-7, URL http://www.sciencedirect.com/science/article/pii/0375947471908517.
[71] T. Nomura, C. Gil, H. Saito, T. Yamazaki, M. Ishihara, E2 Effective charges of the $f_{\frac{7}{2}}$ proton and neutron deduced from the lifetimes of the 6^+ states in ^{50}Ti, ^{54}Fe, and ^{42}Ca, Phys. Rev. Lett. 25 (1970) 1342–1345, http://dx.doi.org/10.1103/PhysRevLett.25.1342, URL https://link.aps.org/doi/10.1103/PhysRevLett.25.1342.
[72] P.M. Lewis, A.R. Poletti, M.J. Savage, C.L. Woods, The mean life of the second 0+ state in ^{42}Ca, Nuclear Phys. A 443 (2) (1985) 210–216, http://dx.doi.org/10.1016/0375-9474(85)90260-X, URL http://www.sciencedirect.com/science/article/pii/037594748590260X.
[73] P.C. Simms, N. Benczer-Koller, C.S. Wu, New application of delayed coincidence techniques for measuring lifetimes of excited nuclear states—^{42}Ca and ^{47}Sc, Phys. Rev. 121 (1961) 1169–1174, http://dx.doi.org/10.1103/PhysRev.121.1169, URL https://link.aps.org/doi/10.1103/PhysRev.121.1169.
[74] D. Bloess, F. Munnich, Untersuchung der Lebensdauer Angeregter Kernniveaus von ^{42}Ca, Z. Naturforsch. 18 (1963) 671.

Bibliography

[1] W. Hauser and H. Feshbach, Phys. Rev. **87**, 366 (1952) 10.1103/PhysRev.87.366.

[2] P. Merrill, Science **115**, 479 (1952).

[3] E. M. Burbidge, G. R. Burbidge, W. A. Fowler, and F. Hoyle, Reviews of Modern Physics **29**, 547 (1957) 10.1103/RevModPhys.29.547.

[4] M. Arnould, S. Goriely, and K. Takahashi, Physics Reports **450**, 97 (2007) 10.1016/j.physrep.2007.06.002.

[5] M. Mumpower, R. Surman, G. McLaughlin, and A. Aprahamian, Progress in Particle and Nuclear Physics **86**, 86 (2016) 10.1016/j.ppnp.2015.09.001.

[6] J. E. McKay, P. A. Denissenkov, F. Herwig, G. Perdikakis, and H. Schatz, Monthly Notices of the Royal Astronomical Society **491**, 5179 (2020) 10.1093/mnras/stz3322.

[7] A. Schiller, L. Bergholt, M. Guttormsen, E. Melby, J. Rekstad, and S. Siem, Nuclear Instruments and Methods in Physics Research, Section A: Accelerators, Spectrometers, Detectors and Associated Equipment **447**, 498 (2000) 10.1016/S0168-9002(99)01187-0.

[8] A. Voinov, E. Algin, U. Agvaanluvsan, T. Belgya, R. Chankova, M. Guttormsen, G. E. Mitchell, J. Rekstad, A. Schiller, and S. Siem, Physical Review Letters **93**, 142504 (2004) 10.1103/PhysRevLett.93.142504.

[9] A. Bürger et al., Physical Review C - Nuclear Physics **85**, 64328 (2012) 10.1103/PhysRevC.85.064328.

[10] A. Simon et al., Physical Review C **93**, 34303 (2016) 10.1103/PhysRevC.93.034303.

[11] A. C. Larsen and S. Goriely, Physical Review C - Nuclear Physics **82**, 14318 (2010) 10.1103/PhysRevC.82.014318.

[12] A. Spyrou et al., Physical Review Letters **113**, 232502 (2014) 10.1103/PhysRevLett.113.232502.

[13] R. Capote et al., Nuclear Data Sheets **110**, 3107 (2009) 10.1016/j.nds.2009.10.004.

[14] T. Ericson and V. Strutinski, Nuclear Physics **8**, 284 (1958) 10.1016/0029-5582(58)90156-1.

[15] H. A. Bethe, Phys. Rev. **50**, 332 (1936) 10.1103/PhysRev.50.332.

[16] A. Gilbert and A. G. W. Cameron, Canadian Journal of Physics **43**, 1446 (1965) 10.1139/p65-139.

[17] T. Ericson, Nuclear Physics **11**, 481 (1959) 10.1016/0029-5582(59)90291-3.

[18] T. v. Egidy and D. Bucurescu, Physical Review C **72**, 044311 (2005) 10.1103/PhysRevC.72.044311.

[19] T. von Egidy and D. Bucurescu, Phys. Rev. C **80**, 54310 (2009) 10.1103/PhysRevC.80.054310.

[20] M. Guttormsen et al., Physical Review C **96**, 24313 (2017) 10.1103/PhysRevC.96.024313.

[21] S. M. Grimes, J. D. Anderson, J. W. McClure, B. A. Pohl, and C. Wong, Physical Review C **10**, 2373 (1974) 10.1103/PhysRevC.10.2373.

[22] G. A. Bartholomew, E. D. Earle, A. J. Ferguson, J. W. Knowles, and M. A. Lone, in *Advances in nuclear physics: volume 7*, edited by M. Baranger and E. Vogt (Springer US, Boston, MA, 1973), pages 229–324, 10.1007/978-1-4615-9044-6{_}4.

[23] D. Brink, "Doctorial thesis", PhD thesis (Oxford University, 1955).

[24] P. Axel, Physical Review **126**, 671 (1962) 10.1103/PhysRev.126.671.

[25] M. Guttormsen, A. C. Larsen, A. Görgen, T. Renstrøm, S. Siem, T. G. Tornyi, and G. M. Tveten, Physical Review Letters **116**, 12502 (2016) 10.1103/PhysRevLett.116.012502.

[26] L. Crespo Campo et al., Physical Review C **98**, 54303 (2018) 10.1103/PhysRevC.98.054303.

[27] A. C. Larsen et al., Jour. Phys. G Nucl. and Part. Phys. **44**, 64005 (2017) 10.1088/1361-6471/aa644a.

[28] J. Isaak et al., Physics Letters B **788**, 225 (2019) https://doi.org/10.1016/j.physletb.2018.11.038.

[29] H. Utsunomiya et al., Physical Review C - Nuclear Physics **88**, 15805 (2013) 10.1103/PhysRevC.88.015805.

[30] H. Beil, R. Bergère, P. Carlos, A. Leprêtre, A. De Miniac, and A. Veyssière, Nuclear Physics, Section A **227**, 427 (1974) 10.1016/0375-9474(74)90769-6.

[31] V. A. PLUJKO, I. M. KADENKO, O. M. GORBACHENKO, and E. V. KULICH, International Journal of Modern Physics E **17**, 240 (2008) 10.1142/S0218301308009744.

[32] S. Goriely and V. Plujko, Physical Review C **99**, 14303 (2019) 10.1103/PhysRevC.99.014303.

[33] S. Goriely et al., European Physical Journal A **55**, 172 (2019) 10.1140/epja/i2019-12840-1.

[34] D. Savran, T. Aumann, and A. Zilges, Progress in Particle and Nuclear Physics **70**, 210 (2013) https://doi.org/10.1016/j.ppnp.2013.02.003.

[35] K. Heyde, P. von Neumann-Cosel, and A. Richter, Rev. Mod. Phys. **82**, 2365 (2010) 10.1103/RevModPhys.82.2365.

[36] N. L. Iudice and F. Palumbo, Physical Review Letters **41**, 1532 (1978) 10.1103/PhysRevLett.41.1532.

[37] H. T. Nyhus, S. Siem, M. Guttormsen, A. C. Larsen, A. Bürger, N. U. Syed, G. M. Tveten, and A. Voinov, Physical Review C - Nuclear Physics **81**, 24325 (2010) 10.1103/PhysRevC.81.024325.

[38] C. P. Brits et al., Physical Review C **99**, 10.1103/PhysRevC.99.054330 (2019) 10.1103/PhysRevC.99.054330.

[39] K. L. Malatji et al., Physical Review C **103**, 14309 (2021) 10.1103/PhysRevC.103.014309.

[40] M. Guttormsen et al., Physical Review C - Nuclear Physics **89**, 14302 (2014) 10.1103/PhysRevC.89.014302.

[41] M. Guttormsen et al., Physical Review C - Nuclear Physics **71**, 044307 (2005) 10.1103/PhysRevC.71.044307.

[42] M. Wiedeking et al., Physical Review Letters **108**, 162503 (2012) 10.1103/PhysRevLett.108.162503.

[43] A. C. Larsen et al., Physical Review Letters **111**, 242504 (2013) 10.1103/PhysRevLett.111.242504.

[44] M. D. Jones et al., Physical Review C **97**, 24327 (2018) 10.1103/PhysRevC.97.024327.

[45] E. Litvinova and N. Belov, Physical Review C - Nuclear Physics **88**, 31302 (2013) 10.1103/PhysRevC.88.031302.

[46] R. Schwengner, S. Frauendorf, and A. C. Larsen, Phys. Rev. Lett. **111**, 232504 (2013) 10.1103/PhysRevLett.111.232504.

[47] Jouni Suhonen, *From Nucleon to Nucleus* (Springer, 2007).

[48] M. Czerwiński et al., Physical Review C - Nuclear Physics **92**, 14328 (2015) 10.1103/PhysRevC.92.014328.

[49] E. Caurier, G. Martínez-Pinedo, F. Nowacki, A. Poves, and P. A. Zuker, Reviews of Modern Physics **77**, 427 (2005) 10.1103/RevModPhys.77.427.

[50] J. E. Midtbø, A. C. Larsen, T. Renstrøm, F. L. Bello Garrote, and E. Lima, Physical Review C **98**, 064321 (2018) 10.1103/PhysRevC.98.064321.

[51] S. Goriely, S. Hilaire, and A. J. Koning, Physical Review C - Nuclear Physics **78**, 64307 (2008) 10.1103/PhysRevC.78.064307.

[52] D. Bohm and D. Pines, Phys. Rev. **82**, 625 (1951) 10.1103/PhysRev.82.625.

[53] S. Goriely, S. Hilaire, S. Péru, and K. Sieja, Physical Review C **98**, 014327 (2018) 10.1103/PhysRevC.98.014327.

[54] A. J. Koning, S. Hilaire, and M. C. Duijvestijn, in Nd2007 (2007), pages 211–214, 10.1051/ndata:07767.

[55] E. V. Van Loef, P. Dorenbos, C. W. Van Eijk, K. Krämer, and H. U. Güdel, Applied Physics Letters **79**, 1573 (2001) 10.1063/1.1385342.

[56] S. Riboldi et al., in 2011 ieee nuclear science symposium conference record (2011), pages 776–778, 10.1109/NSSMIC.2011.6154296.

[57] A. Giaz et al., Nuclear Instruments and Methods in Physics Research Section A: Accelerators, Spectrometers, Detectors and Associated Equipment **729**, 910 (2013) https://doi.org/10.1016/j.nima.2013.07.084.

[58] M. Guttormsen, A. Bürger, T. E. Hansen, and N. Lietaer, Nuclear Instruments and Methods in Physics Research Section A: Accelerators, Spectrometers, Detectors and Associated Equipment **648**, 168 (2011) https://doi.org/10.1016/j.nima.2011.05.055.

[59] V. W. Ingeberg, *OCLDAQ*, 2022, 10.5281/ZENODO.6052828.

[60] V. W. Ingeberg, fzeiser, and E. Lima, *oslocyclotronlab/Qkinz: Update*, 2018, 10.5281/zenodo.1206099.

[61] M. Lipoglavšek et al., Nuclear Instruments and Methods in Physics Research, Section A: Accelerators, Spectrometers, Detectors and Associated Equipment **557**, 523 (2006) 10.1016/j.nima.2005.11.067.

[62] L. Msebi, "Lifetime measurements of excited nuclei through modern nuclear spectroscopy", PhD thesis (Unversity of Western Cape, 2021).

[63] M. Guttormsen, T. S. Tveter, L. Bergholt, F. Ingebretsen, and J. Rekstad, Nuclear Instruments and Methods in Physics Research, Section A: Accelerators, Spectrometers, Detectors and Associated Equipment **374**, 371 (1996) 10.1016/0168-9002(96)00197-0.

[64] M. Guttormsen, T. Ramsøy, and J. Rekstad, Nuclear Inst. and Methods in Physics Research, A **255**, 518 (1987) 10.1016/0168-9002(87)91221-6.

[65] S. Agostinelli et al., Nuclear Instruments and Methods in Physics Research Section A: Accelerators, Spectrometers, Detectors and Associated Equipment **506**, 250 (2003) 10.1016/S0168-9002(03)01368-8.

[66] V. W. Ingeberg, *AFRODITE*, 2022, 10.5281/zenodo.5902767.

[67] V. W. Ingeberg, *vetlewi/MiniballREX: Ni67*, 2022, 10.5281/ZENODO.6075853.

[68] A. Voinov, M. Guttormsen, E. Melby, J. Rekstad, A. Schiller, and S. Siem, Physical Review C - Nuclear Physics **63**, 443131 (2001) 10.1103/PhysRevC.63.044313.

[69] M. Wiedeking, M. Guttormsen, A. C. Larsen, F. Zeiser, A. Görgen, S. N. Liddick, D. Mücher, S. Siem, and A. Spyrou, Physical Review C **104**, 014311 (2021) 10.1103/PhysRevC.104.014311.

[70] D. Mücher et al., *A novel approach for extracting model-independent nuclear level densities far from stability*, 2020.

[71] K. S. Krane, *Introductory Nuclear Physics* (Wiley & Sons Inc., 1988).

[72] M. Markova et al., Physical Review Letters **127**, 182501 (2021) 10.1103/PhysRevLett.127.182501.

[73] D. Muecher and A. Spyrou, *Constraining neutron capture rates for r-process nuclei in the A=140 region*, 2018.

[74] Y. Togano et al., *Determination of neutron capture reaction cross sections of Cd isotopes at N <= 82*, 2021.